University of California

Los Angeles

Strange Hadron(K_S^0, Λ and Ξ) Production in d+Au Collisions at $\sqrt{s_{NN}} = 200$ GeV at RHIC

A dissertation submitted in partial satisfaction

of the requirements for the degree

Doctor of Philosophy in Physics

by

Hai Jiang

2005

The dissertation of Hai Jiang is approved.

Nu Xu

Gang Li

Graciela Gelmini

Charles A. Whitten Jr., Committee Co-chair

Huan Z. Huang, Committee Co-chair

University of California, Los Angeles

2005

Table of Contents

List of Figures

List of Tables

Acknowledgments

I would sincerely thank Professor Huan Z. Huang and Professor Charles A. Whitten Jr. for the best advising they have given to me when I was working on this thesis. Without their guidance and push my thesis would never be finished. Also I would like to thank other members of the UCLA Relativistic Heavy Ion Group: G. Igo, S. Trentalange, V. Ghazikhanian, A. Tai, H. Long, P. Sorensen, J. Wood, D. Thein, S. Guertin, J. G. Ma, J. Gonzalez, W. J. Dong. The weekly discussions with them enlarged my vision of knowledge in physics and help correct mistakes I made in data analyses. Special thanks to H. Long and P. Sorensen for their close direction on analysis details, to An Tai for many helps on physics discussions. I also appreciate the financial support from the Nuclear Collisions group at Lawrence Berkeley National Laboratory, especially thank to Nu Xu for physics discussions. The completion of this fabulous work would not be possible without the contribution from all the members of the STAR Collaboration and the RHIC Operations Group, specially from my physics working group - strangeness group. Thanks to the convenors for their tireless work.

Here I would like to thank my parents in China who were always encouraging and supporting me to complete my PhD degree.

VITA

11 Feb. 1971	Born, Hangzhou, Zhejiang, P.R.China
1994	B.S. Physics Zhejiang University Hangzhou ,P.R.China
1997	M.S. Physics Beijiang University Beijing, P.R.China
1998-2000	Teaching Assistant Department of Physics University of California - Los Angeles
2002	M.S. Computer Science University of California - Los Angeles Los Angeles, CA
2003 – 2005	Graduate Research Assistant Heavy Ion and Intermediate Energy Physics Group University of California - Los Angeles

PUBLICATIONS AND PRESENTATIONS

H. Jiang *et al.*
Strange Hadron Production in d+Au collisions at RHIC
Proceedings of 21st Winter Workshop on Nuclear Dynamics 2005.

J. Adams *et al.*
Open charm yields in d+Au collisions at $\sqrt{s_{NN}} = 200$ GeV
Phys. Rev. Lett., **94**:062301, 2005.

J. Adams *et al.*
Particle-type dependence of azimuthal anisotropy and nuclear modification of particle production in Au+Au collisions at $\sqrt{s_{NN}} = 200$ GeV
Phys. Rev. Lett., **92**:052302, 2004.

J. Adams *et al.*
Cross Sections and Transverse Single-Spin Asymmetries in Forward Neutral Pion Production from Proton Collisions at $\sqrt{s_{NN}} = 200$ GeV
Phys. Rev. Lett., **92**:171801, 2004.

J. Adams *et al.*
Azimuthal anisotropy at the Relativistic Heavy Ion Collider: the first and fourth harmonics
Phys. Rev. Lett., **92**:062301, 2004.

J. Adams *et al.*
Azimuthal anisotropy and correlations at large transverse momenta in p+p and Au+Au collisions at $\sqrt{s_{NN}} = 200$ GeV
Phys. Rev. Lett., **93**:252301, 2004.

J. Adams *et al.*
Azimuthally sensitive HBT in Au+Au collisions at $\sqrt{s_{_{NN}}} = 200$ GeV
Phys. Rev. Lett. **93**:012301, 2004.

J. Adams *et al.*
Measurements of transverse energy distributions in Au+Au collisions at $\sqrt{s_{NN}} = 200$ GeV
Phys. Rev. C **70**:054907, 2004.

J. Adams *et al.*
Pseudorapidity Asymmetry and Centrality Dependence of Charged Hadron Spectra in d+Au Collisions at $\sqrt{s_{NN}} = 200$ GeV
Phys. Rev. C **70**:064907, 2004.

J. Adams *et al.*
Transverse-momentum dependent modification of dynamic texture in central Au+Au collisions at $\sqrt{s_{NN}} = 200$ GeV
Phys. Rev. C **71**:031901(R), 2005.

H. Jiang
Production of Λ and K_S^0 in d+Au collisions at $\sqrt{s_{NN}} = 200$ GeV
Contribution to the American Physical Society Meeting, Tucson, Arizona, 2003.

H. Jiang
K_S^0, Λ and Ξ production in d+Au collisions at RHIC
Contribution to the American Physical Society Meeting, Chicago, Illinois, 2004.

Abstract of the Dissertation

Strange Hadron(K_S^0, Λ and Ξ) Production in d+Au Collisions at $\sqrt{s_{NN}} = 200$ GeV at RHIC

by

Hai Jiang

Doctor of Philosophy in Physics

University of California, Los Angeles, 2005

Professor Huan Z. Huang, Co-chair

Professor Charles A. Whitten Jr., Co-chair

The study of identified particles from deuteron(d)+gold(Au) collisions provide a crucial reference to investigate nuclear effects observed in Au+Au collisions where a thermalized partonic state - Quark Gluon Plasma (QGP) - is thought to have been created.

The measurements of transverse mass(m_T) and momentum(p_T) spectra at mid-rapidity ($|y| < 1$) for the identified strange hardons: K_S^0, $\Lambda + \overline{\Lambda}$ and $\Xi^- + \overline{\Xi}^+$ from d+Au collisions are presented. The measured p_T covers $0.4 < p_T < 6.0$ GeV/c for K_S^0 and $\Lambda + \overline{\Lambda}$ and $0.6 < p_T < 5.0$ GeV/c for $\Xi^- + \overline{\Xi}^+$. These particles were reconstructed from the topological characteristics of their weak decays in the STAR Time Projection Chamber(TPC).

The m_T spectra of these particles are well described by a double exponential function which can be understood by two component models: soft(thermal) hadron production at low m_T and hard hadron production at high m_T. The integrated yields (dN/dy) and mean p_T ($< p_T >$) of these particles are calculated from the fit functions for different centralities. The dN/dy normalized to

the number of participants(N_{part}) increase with N_{part}. The $\Lambda(\overline{\Lambda})$ dN/dy values at the mid-rapidity and forward rapidity regions agree with the EPOS model calculations.

The measured Λ/K^0_S ratios show the greatest baryon enhancement at $p_T \sim$ 2 GeV/c in d+Au collisions. The strangeness enhancement going from d+Au to Au+Au collisions grows with the number of strange quark in a hadron. The magnitude of the enhancement is in the same order as the SPS measurement.

The nuclear modification factors R_{CP} normalized to binary collisions indicate that the Cronin effect in d+Au collisions has a distinct particle type dependence. The R_{CP} ratios show a distinct baryon versus meson dependence: the R_{CP} for $\Xi^- + \overline{\Xi}^+$ follows that for $\Lambda + \overline{\Lambda}$ while the R_{CP} for the ϕ is close to that for the K^0_S. The mechanism based on initial hadron or parton multiple scattering is not sufficient to explain this particle type dependence. Hadronization processes through multi-parton dynamics such as coalescence and recombination models are likely to be important for explaining baryon enhancement and the Cronin effect in high-energy d+Au collisions.

CHAPTER 1

Introduction

Relativistic heavy ion collisions provide a valuable tool to study the properties of nuclear matter at high temperature and energy density [Qua04]. In these collisions, atomic nuclei (heavy-ions) moving at nearly the speed of light collide and deposit a large amount of energy in a small region of space where the temperature and density is comparable with that existed in the early universe approximately one microsecond after the Big Bang (the starting point of Universe). At such extreme conditions, it is believed that chiral symmetry described in Quantum ChormoDynamics (QCD) will be restored and a new phase of nuclear matter, called Quark-Gluon Plasma (QGP) may exist. In this chapter, we will discuss the physical phenomena of relativistic heavy ion physics and introduce the topics relevant to the thesis research.

1.1 Quarks-Gluons, Hadrons and QCD

In the QCD framework, all matter is made of quarks, leptons, like electrons and positrons, and particles mediating interactions, like photons, gluons and gravitons. Quarks are the basic building block for hadrons. Hadrons are subdivided into two classes, baryons carrying three quarks or antiquarks and mesons carrying one quark and one antiquark. Baryons include nucleons and a large number of other particles, like Λ and Ξ which we will discuss in more detail later. Mesons include pions, kaons, ϕ and so on. There are six different types, or $flavors$, of quarks: u(up), d(down), s(strange), c(charm), t(top), b(beauty or bottom). Nucleons only carry the lightest quarks u and d. The hadrons carrying strange quarks are called strange hadrons. Quarks have another important degree of freedom, known as *color*, just as electric charge to electrons. A color is assigned to each quark,for example, R(red), G(green) and B(blue). All hadrons are *colorless* objects. The forces between colored quarks are called strong interactions which is well described by Quantum ChromoDynamics (QCD). According to QCD, gluons are the carriers of strong interactions between quarks, just as photons are the carriers of electromagnetic force in Quantum ElectroDynamics(QED).

For electromagnetic forces the coupling constant $\alpha = \frac{1}{137}$ is less than unity and an elegant mathematical method using perturbation calculations have been well established. The strong interaction, however, with a coupling constant α_s larger than one at low energy, can not be calculated as a series expansion. Fortunately, thanks to the discovery of the theory known as $asymptotic freedom$ whose discoverers were awarded the Nobel Prize in Physics in 2004, the strong force between quarks becomes smaller as the distance gets shorter [Pol73, GW73]. Hence perturbative QCD (pQCD) is applicable to short distance ($\sim fm^3$) or high momentum transfer process. At larger distances, the force between quarks becomes stronger [Won94] and a quark cannot be removed from a hadron: quarks are confined. In a scattering involving a high momentum transfer(hard process), the quarks move within nucleons (neutron and proton), essentially as free, non-interacting particles, and it allows physicists to calculate cross sections of the collision based on pQCD. Over the past decades, many experiments have been done on hard processes to test the validity of pQCD calculation based on $asymptotic freedom$. Fig. 1.1 shows differential cross-sections as a function of

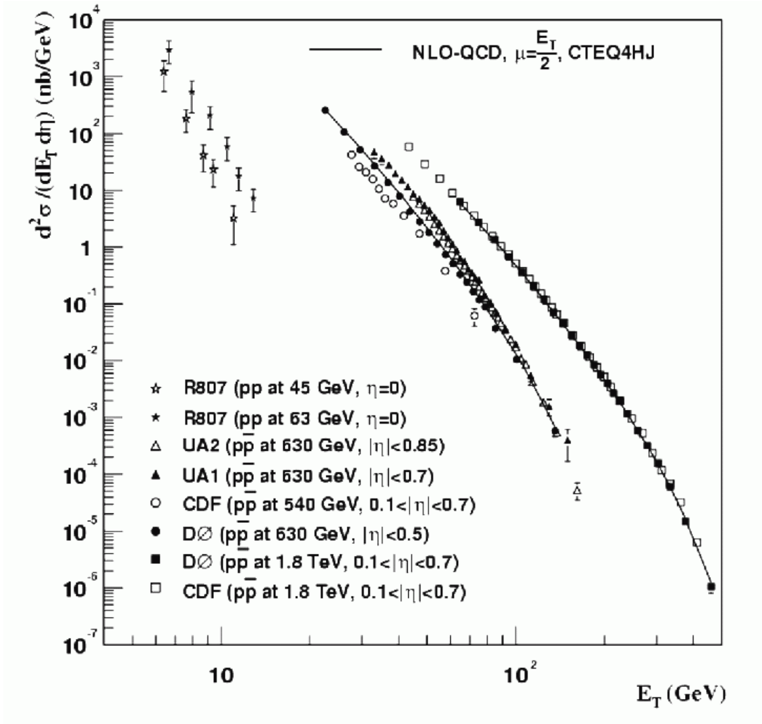

Figure 1.1: Inclusive differential cross-sections for single jet production as a function of the jet transverse energy(E_T) in proton (anti)proton collisions. Curves are next leading order (NLO) pQCD predictions for $p\bar{p}$ at center-of-mass energy $\sqrt{s}$=630 GeV and 1.8 TeV.

transverse energy(E_T) from pp and $p\bar{p}$ collisions [Hag02]. For the high E_T domain, pQCD calculations are in good agreement with experimental observations.

1.2 Bag Model, Lattice QCD and QGP

Although the pQCD has been well developed and verified by experiments as shown in Fig. 1.1, it fails to explain the large-distance or small-momentum tranfer behaviors of quark-gluon systems, like the equilibrium phases and phase transition, since the coupling constant α_s goes above one under these conditions.

A useful phenomenological approach, called **Bag Model**, sheds light on some nonperturbative properties of the system [CJJ74, DD83]. It assumes that the total kinetic energy of quarks in a hadron is counterbalanced by an inward bag pressure B. As the temperature increase, the total kinetic energy of quarks may exceed the bag pressure B, and the bag breaks up and quarks do not belong to any individual hadron. Quarks are **deconfined** and can move in a larger volume. That nuclear matter can turn into a new phase of a quark gluon soup at high temperature or net baryon density.

Whereas the **Bag Model** only provides a qualitative understanding of the new phases of quark matter, lattice QCD, a nonperturbative approach, gives a quantitative description on quark-gluon systems by applying QCD on discrete lattices of space-time coordinates. Lattice QCD is a large-scale numerical simulation of quantum chromodynamics and relies on computers to calculate the path integrals. In principle, lattice QCD can be used for many physics regimes where pQCD is not valid. However, its performance is limited by computer memory and speed. The main result from the lattice calculation is presented in Fig. 1.2 [Kar02]. The energy density ϵ (scaled by T^4), reflecting the number of degrees of freedom in the system, rapidly increases at the critical temperature T_C. This rise corresponds to a phase transition from the hadronic matter at low temperature to a new state at high temperature where quarks and gluons do not belong to individual nucleons. This new state is called the Quark-Gluon Plasma (QGP). The magnitude of the critical temperature T_C depends on the number of quarks in a hadron used in the computation. The typical T_C is in the order of 150 - 200 MeV. Lattice QCD calculations also indicate that the order of the phase transition depends on the strange quark masses [Got87].

This deconfined quark matter, QGP, is believed by most scientists to exist in the early universe about one microsecond after the Big Bang when the universe,

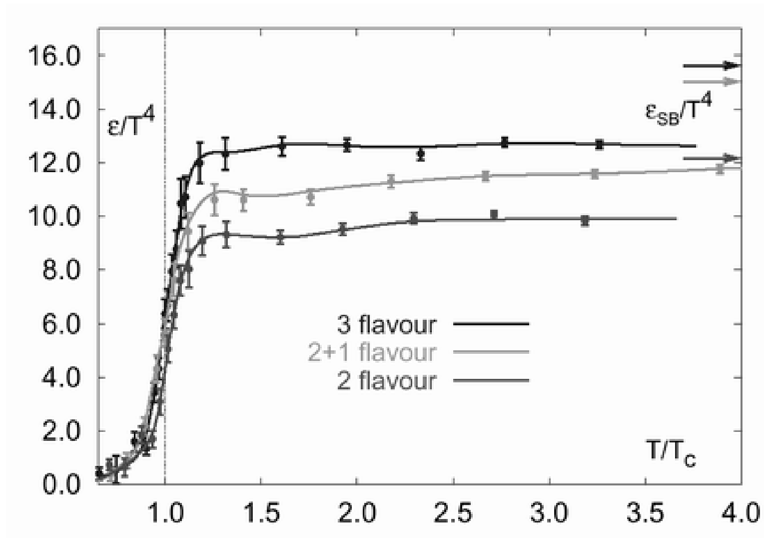

Figure 1.2: The energy density as a function of the system temperature (T) from lattice QCD calculations. A phase transition occurs when T reaches the critical temperature (T_C). The system transfers from hadronic matter to Quark-Gluon Plasma (QGP) where quarks and gluons are deconfined.

much smaller in space than the one at present, was at a extremely high temperature and hadrons were not yet formed. In laboratories such conditions for the QPG can be created through relativistic heavy-ion collisions. In fact, not only the high temperature but also the high baryon density can lead to a condition for the QGP formation. In current universe, we expect to observe this new state of matter at the center of neutron stars where the mass density can be as much as $10^{16} - 10^{17}$ gm/cm^3 [CP75]. The QCD phase diagram [BGS98] (Figure 1.3) shows that QGP exists in nature with high baryon density or in high energy heavy ion collision experiments where the temperature is extremely high. We will only discuss heavy ion collisions in this thesis.

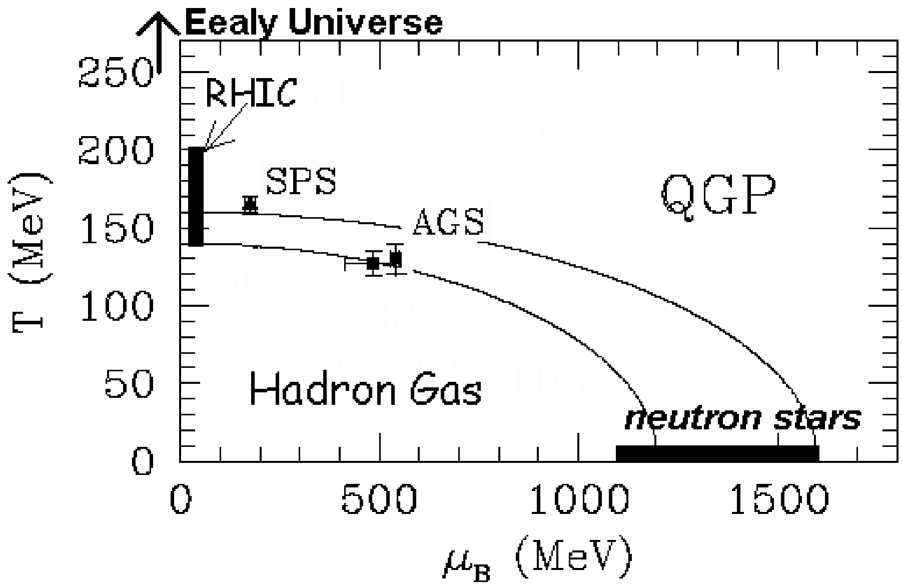

Figure 1.3: The phase diagram of nuclear matter. The possible new phase QGP can be observed through enhancing the temperature(in heavy ion collisions) or the baryon density(in neutron stars). The chemical density μ_B is a variable reflecting the baryon density. The two lines mark the location of the expected phase boundary at its level of uncertainty.

1.3 Heavy ion collisions

Motivated by the lattice QCD prediction for the existence of the QGP, scientists have studied heavy ion collisions since the 1980's to search for experimental evidences of a quark hadron phase transition by building high energy accelerators, such as the Alternating Gradient Synchrotron (AGS) at Brookhaven, USA and the SPS at CERN, the largest nuclear research center in Europe.

The QGP is thought to be a thermodynamically equilibrated deconfined quarks and gluons and its behaviors reflect the bulk properties of a hot dense many-body system. Ideally, the QGP should be studied in a static system with infinite number of quarks and gluons. In practice gold (the number of nucleons = 197) and lead (the number of nucleons = 207) are two good candidates for heavy ion collisions due to their easiness to find and operate. Gold(Au) has been used at the AGS with a center-of-mass(CM) collision energy of $\sqrt{s_{NN}} = 4.7$ GeV, and Lead(Pb) at the SPS with a CM energy of $\sqrt{s_{NN}} = 17.4$ GeV. Both CM energies were limited since the beams collided with fixed targets. The results from these two experiments proved that a direct observation of the predicted phase transition was difficult.

The Relativistic Heavy-Ion Collider (RHIC), built at at Brookhaven National Laboratory, Long Island, USA, was designed to search for the new phase of nuclear matter, thought to be prevalent in the early universe, by colliding two beams of atomic nuclei(Au) at 99.95 percent the speed of light. The full collision energy at RHIC is up to $\sqrt{s_{NN}} = 200$ GeV, 10 times greater than the AGS and SPS. As shown in Fig. 1.3 higher temperature and less net baryon(the difference of baryon numbers and anti-baryon numbers) density can be reached in the collisions at RHIC than those at the AGS and SPS, and thus new physics may be revealed at RHIC. The colliding nuclei are called heavy ions because electrons are stripped away and the nuclei carry positive charges during the collisions. Unlike AGS and SPS, RHIC is the first machine in the world that is capable of colliding two high energy heavy ion beams moving in opposite directions. The RHIC complex will be discussed in more detail in Chapter 2.

Experimental data were taken at RHIC from Au+Au collisions at $\sqrt{s_{NN}} =$ 130 GeV in 2000. In 2001, RHIC was running with full energy of $\sqrt{s_{NN}} =$ 200 GeV in Au+Au collisions. Many physics results have been obtained from the first two year runs. Some of the observations at RHIC were fitted well by the theoretical predictions for the formation of a quark-gluon plasma (QGP) state [Ada05a, Adc05]. However, to distinguish the origin of phenomena from various theoretical models all of which seem to fit the experimental data, more crosscheck needs to be done not only in Au+Au but also d+Au and p+p collisions.

1.4 Nucleus-Nucleus Collision Dynamics

A high energy head-on nucleus-nucleus collision can be viewed in the laboratory frame as two thin disks approaching each other at nearly the speed of light because of the Lorentz contraction effect in the moving direction. While a precise theoretical description of the collision dynamics is difficult to find, it is generally believed the ultra-relativistic heavy-ion collision has four stages of the evolution as shown in Fig. 1.4: pre-equilibrium parton cascade, an equilibrated QGP, hadronization and freeze-out of hadrons. After the collision of two nuclei(Au at RHIC) at (z, t)=(0,0), the energy density may be sufficiently high for the formation of deconfined quarks and gluons, a cascade of colliding partons. This partonic state initially may not be in thermal equilibrium, but the interaction between partons eventually bring the system into a local equilibrium at the proper time τ_0 when the QGP is formed. Then the QGP expands and its temperature drops down with increasing time. The hadronization process takes place at a time in the order of $\sim 10\tau_0$. This stage involves the formation of hadrons and hadrons continue to interact with each other. As the system expanding further, the interactions between the hadrons stop and the hadrons stream out of the collision region and the temperature falls below the freeze-out point.

Experimentally, since the direct probe of the QGP and hadronization process is not possible, the measurement of the particles in the final stage is the only way for us to study the formation and evolution of the QGP at the early stages. The initial energy density ϵ right after the collision can be determined according to the produced particles [Bjo83].

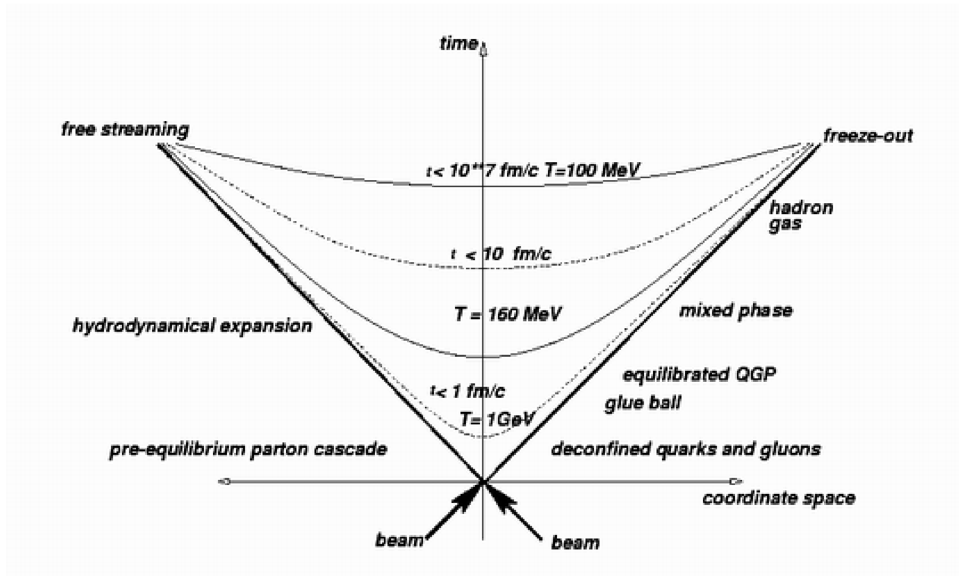

Figure 1.4: The space-time picture of a nucleus-nucleus collision

$$\epsilon = \frac{m_T}{\tau_0 A} \frac{dN}{dy}|_{y=0}. \tag{1.1}$$

where $m_T = \sqrt{m^2 + p_T^2}$ is the transverse mass of the particles produced, m and p_T are the mass and the transverse momentum of the particles, respectively. A is the overlapping area of two colliding nuclei and $\frac{dN}{dy}|_{y=0}$ is the number of hadrons per unit rapidity(see Appendix A). The τ_0, the proper time of thermalizing initial partons, may depend on the colliding beam energy and is believed to be on the order of 1 fm/c [Bjo83]. For Au+Au collisions at RHIC, most produced particles are pions. The energy density ϵ is about 4.6 GeV/fm^3 [Zaj02] for Au+Au collision at $\sqrt{s_{NN}}$ = 130 GeV and 5.0 GeV/fm^3 [DE03] for $\sqrt{s_{NN}}$ = 200 GeV at RHIC. These estimates of the energy density exceed the critical density for the QGP formation, ~1.0 GeV/fm^3, calculated from lattice QCD.

It is a big challenge for scientists to determine the thermally equilibrated QGP by studying the properties of the particles produced after the hadronization. We need to carefully distinguish the observations dominated by the QGP from those dominated by other nuclear effects.

1.5 Collision Geometry

Different from proton-proton collisions, nuclear collisions can be reliably classified according to their *centrality* - a variable measuring the degree of overlapping between two colliding nuclei. Centrality is closely related to the impact parameter b that is defined as the transverse distance between the centers of two colliding nuclei in a nucleus-nucleus collision as illustrated in Figure 1.5 where deuteron-nucleus collision geometry is also included(the deuteron contains a proton and a neutron). Although b cannot be directly measured in experiments, it has been widely used in theoretical models. N_{part} is another critical parameter in nuclear reactions and is a function of b. Roughly speaking, a head-on collision with a small b involves more colliding nucleons, thus a large N_{part}. For the most central collisions, the impact parameter $b = 0$ and $N_{part} \approx A + A$. The probability of this kind of collisions is very samll, therefore corresponding to a top percentage (a few %) of centrality. Another similar collision parameter, N_{binary}, represents the number of equivalent nucleon-nucleon collisions in a nucleus-nucleus collision. N_{part} and N_{binary} can be obtained from model calculations. At STAR, the centrality is determined by measuring the charged particle multiplicity, N_{ch}, for Au+Au and d+Au collisions. Larger N_{ch} corresponds to more central collisions. For example, in Au+Au 200 GeV collisions the centrality 0-5% at STAR means the top 5% events that have the averaged $N_{ch} > 686$ in middle rapidity region($|y| < 0.5$).

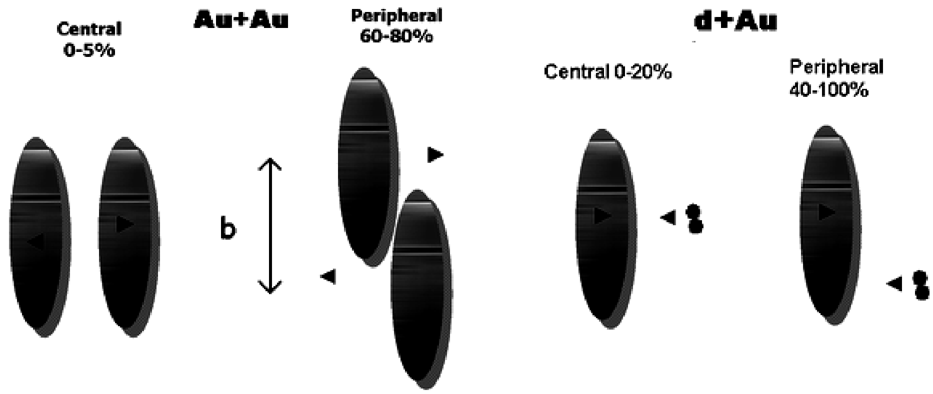

Figure 1.5: Illustration of nuclear collision geometry and centrality for Au+Au collisions at RHIC STAR. The percentage numbers of centrality are not accurate and are only for illustration purpose.

1.6 Transverse Mass(Momentum) Spectra

In nuclear collisions, the most important observable is the cross section or the particle yield as a function of the transverse mass, $m_T = \sqrt{m^2 + p_T^2}$, or the transverse momentum p_T. While in high energy pp or ee collisions the differential invariant cross section $Ed^3\sigma/dp_x dp_y dp_z$ is usually used, in heavy-ion collisions people are more interested in the invariant transverse mass(momentum) spectrum at a specific rapidity region,

$$\frac{d^2N}{2\pi p_T\, dp_T\, dy} \tag{1.2}$$

due to its convenience for measurements(see Appendix B for derivation). It is easy to prove that the magnitudes of transverse mass and momentum distribution are equal. The transverse mass(momentum) spectrum normalized to the number of events is equal to the differential invariant cross section over the total cross section.

The shape of particle $m_T(p_T)$ spectrum depends on the mechanism for collision dynamics and is used to test theoretical predications. Figure 1.6 shows the p_T spectra of $\Lambda(\overline{\Lambda})$, $\Xi(\overline{\Xi})$ and $\Omega^- + \overline{\Omega}^+$ at mid-rapidity as a function of centrality from Au+Au collisions at 200 GeV. The identical shape between strange and anti-strange hadrons suggests they have the same hadronization picture. The different shapes for different centralities indicate different space-time collision evolution as the impact parameter in collisions changes. By comparing the yield in central relative to peripheral collisions, we can determine some nuclear effects that exist in central collisions, but not in the peripheral.

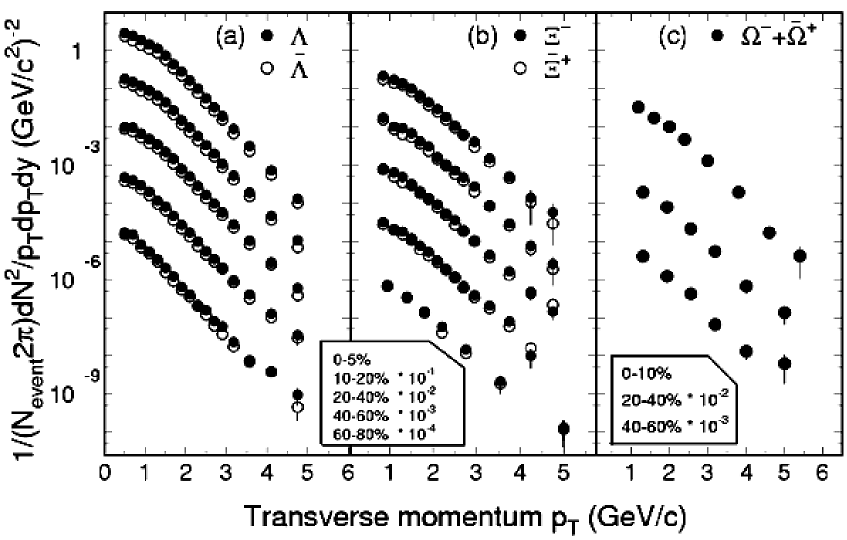

Figure 1.6: Mid-rapidity p_T spectra of Λ, Ξ and Ω from Au+Au collisions at $\sqrt{s_{NN}} = 200$ GeV at RHIC (STAR collaboration) [Lon05b].

At low $p_T (< 2$ GeV/c) in nucleus-nucleus or $p(d)$-nucleus collisions, the spectrum can be well fitted by an exponential function in m_T

$$\frac{d^2N}{2\pi m_T \, dm_T \, dy} \propto e^{-\frac{(m_T - m)}{T}} \tag{1.3}$$

according to thermal models [RD80, RH81] in which a large body of thermal hadronic or patonic matter is thought to act as a source of produced particles.

The fit parameter T, usually called temperature, is directly related to the freeze-out temperature. A larger T means a earlier freeze-out for a specific particle. The heavy multi-strange hadrons, like the Ω and charmed hadrons, are good particles for probing the QGP since they have large T and thus carry early evolution information, probably at the stage of the chemical freeze-out. The hydrodynamic models have been successfully used to describe the collective flow behavior at the low p_T region. The evolution of the flow is treated as an ideal fluid. The flow velocity can be obtained by fitting the spectrum with Blast wave function [Sch93].

However, at high $p_T(> 2$ GeV/c) both the thermal and hydrodynamic models fail and instead other pQCD based models implementing hard parton scattering, gluon shadowing and jet quenching(parton energy loss) are applied. These effects cause a harder(more flat) p_T spectrum which is fitted by a power law function

$$C(1+\frac{p_T}{p_0})^{-n} \tag{1.4}$$

In the heavy-ion collisions, any approach trying to reproduce the experimental data successfully has to deal with the dominant dynamical mechanism for the low p_T(soft) and high p_T(hard) region separately. This two component principle seems not only applicable to the Au+Au system but also to the d+Au system.

1.7 Nuclear Modification Factors, R_{CP} and R_{AA}

While low p_T hadron spectra reflect the behavior of hadronic matter at the hadronization stage, high p_T hadron production is thought to probe the early stage of heavy-ion collisions. It is presumed that these high p_T hadrons are created through large momentum transfer scatterings of partons which pass through dense matter and lose energy by induced gluon radiation at the early stage of the system evolution in central Au+Au collisions at RHIC. [GP90].

It is believed that the QGP would be more likely to be created in central nucleus-nucleus collisions. In peripheral collisions, where the number of effective colliding nucleons is small, the created matter is not sufficiently large to reach thermalization. Nuclear effects can be investigated by measuring a nuclear modification factor, the particle yield ratio from the central to peripheral collisions:

$$R_{CP}(p_T) = \frac{[(dN/dp_T)/N_{binary}]^{Central}}{[(dN/dp_T)/N_{binary}]^{Peripheral}} \tag{1.5}$$

where N_{binary} is the number of binary nucleon-nucleon collisions for each nuclear collision. In the absence of nuclear effects, R_{CP} is expected to be unity at high p_T.

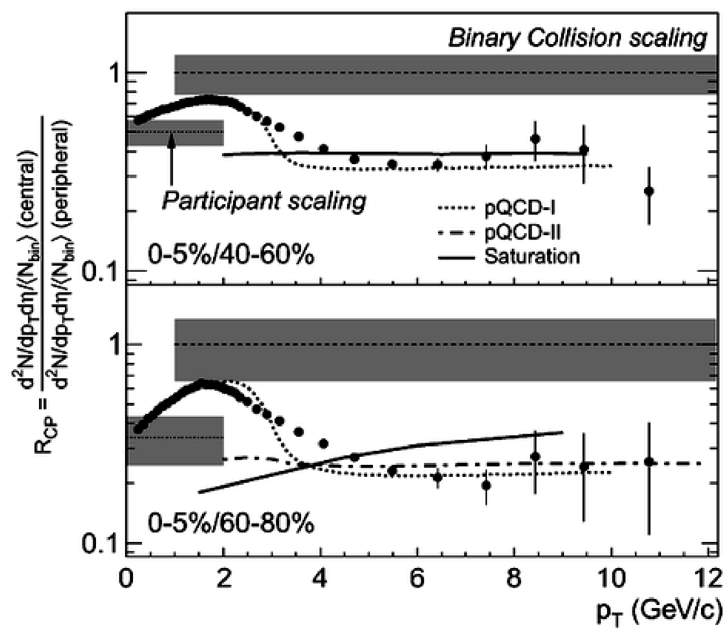

Figure 1.7: The nuclear modification parameter R_{CP} for charged hadrons in Au+Au collisions at $\sqrt{s_{NN}}$=200 GeV at RHIC [Ada03b].

Figure 1.7 shows the R_{CP} ratios of the central yield from the top $0-5\%$ collision centrality to the peripheral yield from $40-60\%$ and $60-80\%$ collision centrality for charged hadrons from Au+Au collisions at $\sqrt{s_{NN}}$=200 GeV [Ada03b]. The R_{CP} shows a strong suppression of particle yields at high p_T for central compared with peripheral collisions. This is consistent with the creation of a dense matter causing the energy loss for high p_T partons that may form jets when they experience multiple scattering in the medium. The final high p_T hadrons from jet fragmentation are then suppressed [VG02b, Wan04b]. This phenomenon is known as jet quenching. However, the suppression may also arise from a consequence of parton saturation in Color Glass Condensate [Kha02]. This initial state effect exists also in d+Au collisions in which the jet quenching is negligible. Therefore, d+Au data will provide a crucial test for these two models.

Like R_{CP}, there is another similar modification parameter defined by taking the ratio of the particle yields in nuclear collisions and the particle yields in proton-proton collisions:

$$R_{AA}(p_T) = \frac{d^2N/dp_T d\eta}{T_{AA} d^2\sigma^{pp}/dp_T d\eta} \tag{1.6}$$

where η is the pseudo-rapidity and $T_{AA} = \langle N_{binary} \rangle \sigma_{inel}^{NN}$. R_{AA} takes pp collisions as a reference instead of peripheral collisions in R_{CP}, providing a better reference since nuclear effects in pp collisions are completely negligible. However, the ratio R_{CP} has smaller systematic uncertainties than R_{AA} because the yields for different centralities in R_{CP} are measured in the same system and R_{AA} requires the extra measurement of pp spectrum as a reference.

The measurement of nuclear modification parameters, R_{CP} or R_{AA} provides a useful tool not only for the study of partonic energy loss in nucleus-nucleus collisions, but also for other nuclear effects, such as the Cornin effect in proton(deuteron)-nucleus collisions.

1.8 Enhancement of Strange Hadrons

Unlike the u and d quarks which are the valence quarks in the nucleon, a massive strangeness quark, s is sensitive to the possible QGP formation because its mass is of the same magnitude as the critical temperature T_c of the phase transition. This means that the measurements of strange hadrons will provide a good signal to detect the deconfined-matter phase [Raf82, RM86]. The properties of some strange hadrons mentioned in this thesis are listed in Table 1.1.

Hadron	Mass(GeV)	Constituent Quarks	τ(mean life)	Species
K_S^0	0.49767	$d\overline{s} + \overline{d}s$	$0.8934 \times 10^{-10}s$	Meson
ϕ	1.01941	$s\overline{s}$	$1.6 \times 10^{-24}s$	Meson
$\Lambda(\overline{\Lambda})$	1.11568	$uds(\overline{u}\overline{d}\overline{s})$	$2.632 \times 10^{-10}s$	Baryon
$\Xi^-(\overline{\Xi}^+)$	1.32132	$dss(\overline{d}\overline{s}\overline{s})$	$2.90 \times 10^{-10}s$	Baryon
$\Omega^-(\overline{\Omega}^+)$	1.67245	$sss(\overline{s}\overline{s}\overline{s})$	$0.822 \times 10^{-10}s$	Baryon

Table 1.1: Properties of strange hadrons.

The strangeness (s) and anti-strangeness ($\overline{s}$) quarks are only made from the vacuum since they are not contained in the colliding nuclei. In the deconfined quark-gluon matter, the $s\overline{s}$ pair can be generated through gluon fusion($g + g \rightarrow s\overline{s}$). The threshold energy for this mechanism is $\sim$ 300 MeV and much smaller than that for other hadronic generation mechanisms like $\pi + N \rightarrow \Lambda + K$ in which the threshold energy is $\sim$ 530 MeV. The gluon channel is dominant and thus strange hadron production is expected to be enhanced if the QGP exists. Fig 1.8 shows the ratio of the $< N_{part} >$ scaled strange particle yield in Pb+Pb collisions to that in p+Pb collisions at the same beam energy per nucleon 158 A GeV ($\sqrt{s_{NN}}$ = 17.2 GeV). The enhancement is more pronounced for multi-strange hyperons. Although the QGP formation would lead to the strangeness enhancement, the observed enhancement does not unequivocally indicate the formation of QGP. Other dynamic mechanisms could cause the same phenomenon [Red01, RT02].

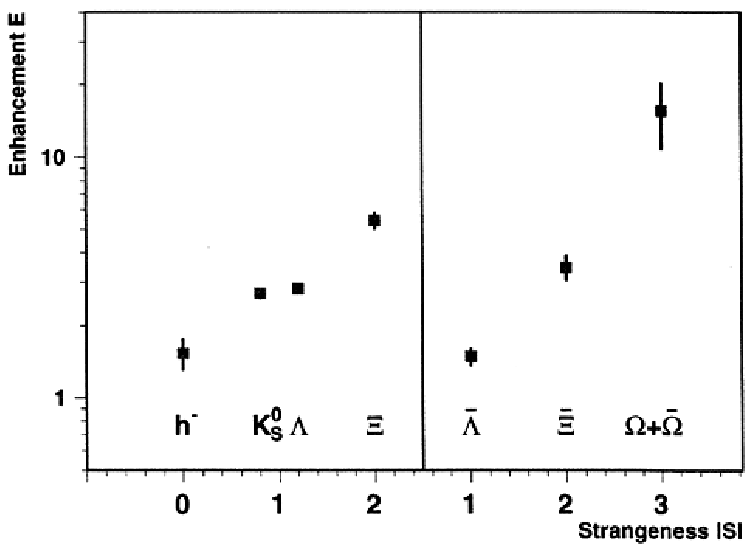

Figure 1.8: Strange particle enhancement versus strangeness content (WA97) [And99]. The fixed-target beam energy per nucleon is 158 A GeV, which is equivalent to $\sqrt{s_{NN}} = 17.2$ GeV.

1.9 Why d(deuteron)+Au collision at RHIC?

The new partonic phase, QGP cannot be directly detected through one or several measurements. The discovery of QGP, unlike the discovery of a new particle, requires a global cross check of consistency at each stage of the collision evolution. The main goal for d+Au collisions at RHIC is to take d+Au measurements as a reference for comparison to results obtained in Au+Au collisions. Some possible observations in favor of the QGP formation in Au+Au collisions need to be investigated in d+Au collisions to verify their uniqueness.

The difference in nuclear effects between d+Au and Au+Au collisions can help find a dominating mechanism among the possible models all of which seem to explain the Au+Au results. For example, a strong suppression of the hadron yield in central Au+Au collisions could arise from initial-state effects: the saturation of of gluon densities in the incoming nuclei, or from final-state effects: energy loss when partons are passing through dense matter created in central collisions. Since the produced matter in d+Au collisions is small in transverse direction, energy loss from the final state effect is not expected while the parton saturation in the initial-state effect may still exist. Thus through the measurement of R_{AA} or R_{CP} in d+Au, we can tell which effect is the origin of the yield suppression in central Au+Au collisions.

In addition, measurements of the d+Au system are interesting in their own right as tests of many theoretical models which predict the particle p_T and rapidity dependence. Of special interest is the measurement of the Cronin effect in high energy collisions at RHIC.

1.9.1 The Cronin Effect

The Cronin effect is an important nuclear effect that first observed in inclusive hadron spectra in proton-nucleus (pA) collisions [Cro75] 30 years ago. The observable is related to the nuclear modification factors, R_{AA} or R_{CP} as described in Equation 1.5 and 1.6. In absence of nuclear effects one would expect $R(p_T) = 1$, but for pA collisions a suppression exists at small p_T, and an enhancement at moderate p_T, and then when $p_T \to \infty$ the ratio approaches to unity. Experimentally, it was clearly observed in pA collisions at two beam energies $\sqrt{s} = 27.4$ GeV and $\sqrt{s} = 38.8$ GeV in Fermi Lab [Str92]. The experiment was conducted by collisions of 800 GeV protons with the fixed tungsten(W) and beryllium(Be) targets. The p_T dependent ratios for three identified particles were obtained by taking the ratio of the spectra from both collision systems. Figure 1.9 shows the pW-to-pBe ratio of per-nucleon cross sections for pions, kaons and protons. The ratios are less than one at $p_T < 1.5$ GeV/c and greater than one at $1.5 < p_T < 9$ GeV/c. The peak values are around 1.35, 1.5 and 2.2 for pions, kaons and protons respectively, as labelled in the plots and the corresponding p_T is the same for all of them and is about 4.6 GeV/c. The kaon ratio is slightly higher than the pion's, which is due to the high gluon fragmentation for kaons. However, the larger enhancement for protons($uud/\bar{u}\bar{u}\bar{d}$) compared to pions($u\bar{d}/d\bar{u}$) and kaons($u\bar{s}/s\bar{u}$) was explained as a larger rescattering cross section for diquarks($uu/\bar{u}\bar{u}$) to a $u/\bar{u}$ quark or the process of binding a diquark to a $u/\bar{u}$ quark is enhanced in nuclei. Many theoretical models have presented to quantitatively explain the Cronin enhancement in nucleus collisions at these energies based on initial-state nuclear effects: multiple soft/hard hadronic or patonic scattering [Kuh76, LP83].

The Cronin effect has received renewed interest in the recent heavy-ion experiments at RHIC. The strongly suppressed R_{AA} ratio due to a large jet quenching in central Au+Au collisions makes the Cronin effect not as pronounced as that in low energy pA collisions. However, the analysis of charged hadron spectra in d+Au collisions has revealed the Cronin effect does exists in high energy heavy-ion collisions, though with a smaller magnitude. Figure. 1.10 shows the p_T dependent R_{AA} ratio of charged hadrons in d+Au minimum bias and central events as well as that in Au+Au central collisions for comparison [Ada03a]. There is a clear Cronin enhancement at $1.5 < p_T < 7$ GeV/c for d+Au collisions.

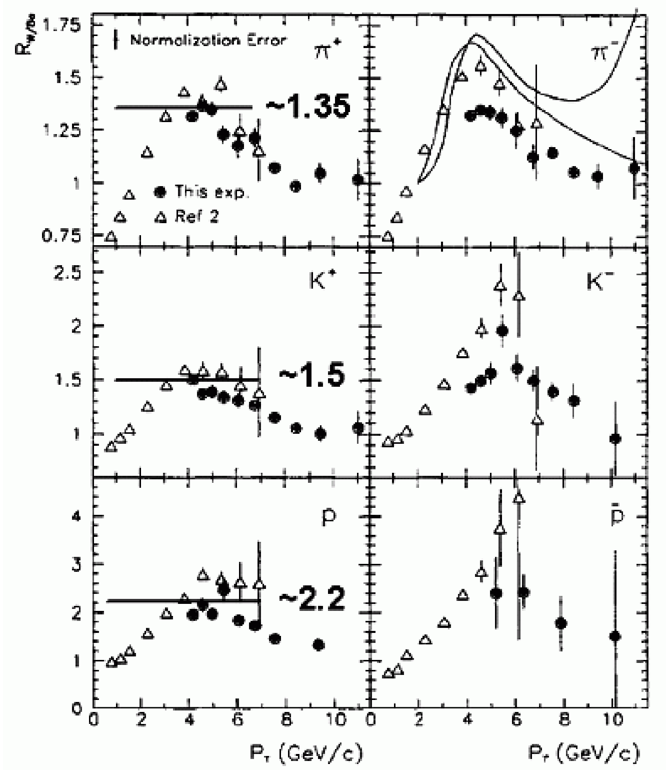

Figure 1.9: $R_{W/Be}$, pW-to-pBe ratio of per-nucleon cross sections, vs. p_T for π, K and p at low energy collisions. Open triangles are the results at $\sqrt{s} = 27.4$ GeV and closed circles at $\sqrt{s} = 38.8$ GeV. The peak values of $R_{W/Be}$ are labelled by numbers. Curves are from the model calculations. [Str92]

1.9.2 Initial State and Final State

Following the framework of multiple scatterings and pQCD jet fragmentation in nuclear reactions, projectile partons in protons(or deuterons) experience several scatterings with small transverse momentum transfer(soft process) then undergo a hard scattering to a high p_T jet(hard process) which then fragment into final hadrons. Initial or final state effects refer to whether the effect happened before or after the hard scattering. In this section we review several theoretical models for the description of the Cronin effect in proton-nucleus(pA) or d+Au collisions. We start with the models developed originally for the lower energy experiments

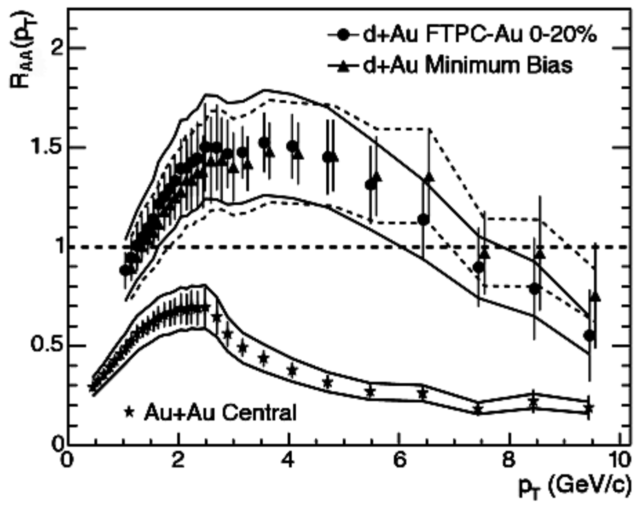

Figure 1.10: R_{AA} for charged hadrons in d+Au collisions at $\sqrt{s_{NN}} = 200$ GeV at STAR(RHIC). The Cronin enhancement at $1.5 < p_T < 7$ GeV/c was seen.

based on initial state effects [Acc03]. Their effectiveness extrapolating to RHIC energies $\sqrt{n} = 130$ and $\sqrt{n} = 200$ GeV remains unkown. Then we discuss the novel models focusing on the final state effects specifically for the RHIC data.

Initial state models: Early attempts to explain the Cronin effect in pA collisions mainly emphasize hadronic or partonic multiple rescatterings. An intrinsic transverse momentum for a parton, k_T, has to be introduced in the proton and nuclear parton distribution functions. The rescatterings cause the intrinsic transverse momentum broadening of the projectile parton compared to that in pp collision.

$$\langle k_T^2 \rangle_{pA} = \langle k_T^2 \rangle_{pp} + \langle k_T^2 \rangle_r \tag{1.7}$$

where the second term on the right hand, $\langle k_T^2 \rangle_r$, is from the rescattering contribution. This broadening will lead to an enhancement at high p_T region(> 2 GeV/c) in pA collisions. Several different approaches implement this schema. In [Wan00, Zha02] rescatterings are on the soft hadron level. Each time the projectile proton interacts with a target nucleon, its partons gain a little intrinsic momentum until the excited proton breaks. Instead of soft hadronic processes, semihard partonic rescatterings were used to calculate the broadening of the intrinsic momentum in [AT01, VG02b]. Slightly different from these models, the color dipole model based on the light-cone QCD-dipole approach describes the Cronin effect without fitting the data. In the model, the parton transverse momentum distribution function was expanded and the zeroth order gives the intrinsic k_T distribution and the first order corresponds to the contribution of one-rescattering process, and so on. These initial state models have not described the particle type dependence in the Cronin effect between bayrons and mesons.

Final state models: Final state effects are thought to take place after a hard scattering of the parton, e.g., at the stage of interaction with a medium or of the final hadronization of the parton. The final state models presented recently, like coalescence or recombination approaches, focus on the modification of the hadronization process, which provided a natural explanation for the hadron species dependence in the measurement of nuclear modification factors at RHIC. An outgoing high energy parton will break into a jet of partons which share the energy of the initial parton. These partons, eventually turning into many hadrons, can be soft or hard. In the recombination and fragmentation(R+F) model [Fri03] only soft partons are allowed to coalesce into hadrons, while hard partons follow the fragmentation process. In the soft and hard recombination (S+H) model [Gre03] one hard parton is recombined with a thermal(soft) parton from the surrounding medium. This parton recombination or coalescence mechanism most affects the intermediate p_T region, 2-5 GeV/c. Below $p_T = 2$ GeV/c the pure thermal phase dominates and above $p_T = 5$ GeV/c the pure fragmentation dominates. These two models were originally proposed to explain the hadron spectra, ratios, nuclear suppression factor and v_2 in Au+Au collisions. Recently the reombination/coalescence model has been applied to d+Au collisions by Hwa and Yang to describe the hadron spectra and the Cornin effect at mid-rapidity [HY03, HY04a]. In their approach all the fragmented partons recombine to higher momentum hadrons. At very high p_T the recombination of high momentum partons gives the same picture as the fragmentation process. The dominant p_T range from the parton recombination scheme is $3 < p_T < 8$ GeV/c for Au+Au collisions [HY04b] and $1 < p_T < 4$ GeV/c for d+Au collisions [HY04a], which gives a much wider range than that given in the R+F and S+H models. In Chapter 6 we will discuss this model for our d+Au data in detail.

1.10 Outline

In this thesis, we present the spectra measurement for K^0_S, $\Lambda+\overline{\Lambda}$ and $\Xi^-+\overline{\Xi}^+$ in d+Au collisions at $\sqrt{s_{NN}} = 200$ GeV at STAR. In Chapter 2 the RHIC accelerator facility and the STAR detectors will be described. The analysis details for the weak decay hadron reconstruction, yield extraction and efficiency calculations will be presented in Chapter 3, and estimates for systematic uncertainties as well as corrections for weak decay feeddowns are given in Chapter 4. The main results including the p_T and m_T spectra, R_{CP}, the $\overline{\Lambda}/\Lambda$ ratio, the Λ/K^0_S ratio and the integrated yield dN/dy and $\langle p_T \rangle$ are presented in Chapter 5. Finally in Chapter 6 we discuss the comparison of our d+Au results to the models and Au+Au results at the same collision energy.

CHAPTER 2

Experimental Set-up

2.1 RHIC Complex

The Relativistic Heavy Ion Collider (RHIC) located at Brookhaven National Laboratory on Long Island, NY, USA, is designed to provide collisions of various species up to gold ions from two independent intersecting beams. RHIC is a world-class scientific research facility that began operation in 2000, following 10 years of development and construction. The facility consists of two concentric rings of super-conducting magnets that focus and guide the beams and a radio frequency system that captures, accelerates and stores the beams. The ring's diameters are approximately 1.22km.

The whole RHIC complex (Figure 2.1) also includes the Tandem Van de Graaff accelerator, the Booster Synchrotron and the Alternating Gradient Synchrotron (AGS). Gold($^{197}_{79}$Au) atoms generated in the Pulsed Sputter Ion Source in the Tandem have to experience three distinct acceleration processes before injection into the RHIC rings:

1. The Tandem uses static electricity to accelerate Au atoms during the traversal of thin foils, also removing some of their electrons. The Tandem gives billions of these positively charged atoms(ions) a boost of energy, sending

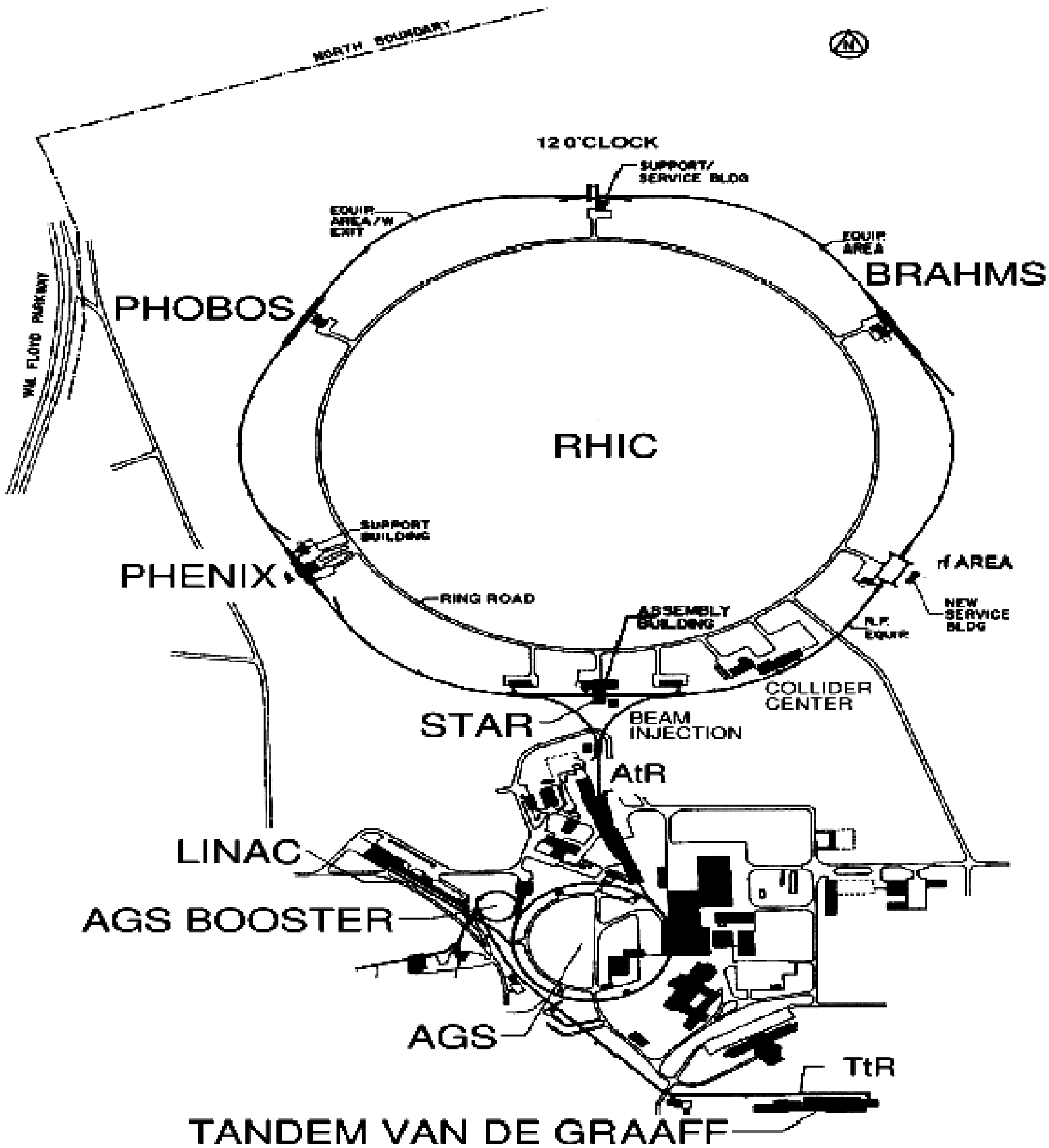

Figure 2.1: A diagram of the RHIC complex(top) including AGS facitlity(bottom) that brings nuclear ions up to RHIC injection energy.

them on their way towards to Booster. On exiting the final foil downstream of the Tandem, the ions have a net charge of $Q = +32e$ and energy of 1 MeV/nucleon;

2. The Booster synchrotron is a compact circular accelerator that provides the ions more energy, by having them surf ride on the downhill slope of radio frequency electromagnetic waves. The ions are propelled forward at higher and higher speeds, getting closer and closer to the speed of light. In the Booster the Au($Q = +32e$) ions are accelerated to 95 MeV/nucleon, and their net charge is increased to $Q = +77e$ from traversal of a "stripping" foil at the exit of the booster;

3. As the $Q = +77e$ ions enter the Alternating Gradient Synchrotron (AGS) from the Booster, they are travelling at about 37% the speed of light. They whirl around the AGS and are accelerated further to 10.8 GeV/nucleon travelling at 99.7% the speed of light. The last two $1s$ electrons are removed by a stripping foil in the transport line between the AGS and the RHIC collider rings. Finally the fully stripped $Q = +79e$ bare Au nuclei are injected into RHIC rings where they are accelerated to collision energy and stored for up to 8 hours.

RHIC can also perform high energy proton-proton collisions. For proton beams, the Linear Accelerator is used as the source instead of the Tandem.

RHIC is the first machine in the world capable of colliding head-on heavy ions. It can collide $p+p$ up to $\sqrt{s_{NN}} = 500$ GeV, Au+Au up to $\sqrt{s_{NN}} = 200$ GeV and deuteron(d)+Au up to $\sqrt{s_{NN}} = 200$ GeV. RHIC can also accelerate other species. Copper-copper(Cu+Cu) collisions were performed at $\sqrt{s_{NN}} = 200$ GeV in 2005. Table 2.1 lists the physical parameters and the performance specifications for the

Physical Parameters			
Crossing points	6		
RHIC circumference(m)	3833.845		
No. Bunches/ring	$\sim$60		
Bunch Spacing (nsec)	213		
Collision Angle	0		
Beam lifetime (hours)	$\sim$8		
Performance Specifications	$Au + Au$	$p + p$	$d + Au$
Top Energy $\sqrt{s_{NN}}$	200	500	200
No. Particles/Bunch	1×10^9	1×10^{11}	10^{11}(d) 10^9(Au)
Luminosity, average (cm^{-2}sec^{-1})	$\sim 2 \times 10^{26}$	$\sim 1.4 \times 10^{31}$	$\sim 2 \times 10^{28}$

Table 2.1: Physical parameters and performance specifications for the Relativistic Heavy Ion Collider (RHIC). Some of these numbers may vary for each run.

year	collisions	collision energy (GeV)	events taken(Million)
2000	Au+Au	130	0.5
2001	Au+Au	200	5
2002	p+p	200	6
2003	d+Au	200	20
2004	Au+Au	200	50
2004	Au+Au	62.4	6
2005	Cu+Cu	200	30

Table 2.2: Experiments run at RHIC from the year of 2000 to 2005. Some short test runs are not included.

RHIC.

There are four experimental collaborations at RHIC: BRAHMS, PHOBOS, PHENIX and STAR. More than 1000 physicists from about 130 institutions around the world are working at RHIC.

The STAR collaboration is one of two largest groups at RHIC. The STAR detector began data taking in June 2000. Table 2.2 shows the experimental runs on various particle sources during the past 5 years.

In this thesis we present an analysis of d+Au collisions recorded by the STAR detector in 2003. d+Au collisions were chosen instead of p+Au collisions because the charge to mass ratio (Z/A) for the deuteron (1/2) is much closer to the ratio for Au (79/197), and therefore less adjustment of magnetic fields for is needed to provide the same energy nucleon in the two rings.

2.2 The STAR Detector

The Solenoidal Tracker At RHIC (STAR) was designed to search for signatures of a possible new state of matter, the quark-gluon plasma (QGP). In the absence of definitive signatures for the QGP, it requires a detection system that can simultaneously measure many experimental observables.

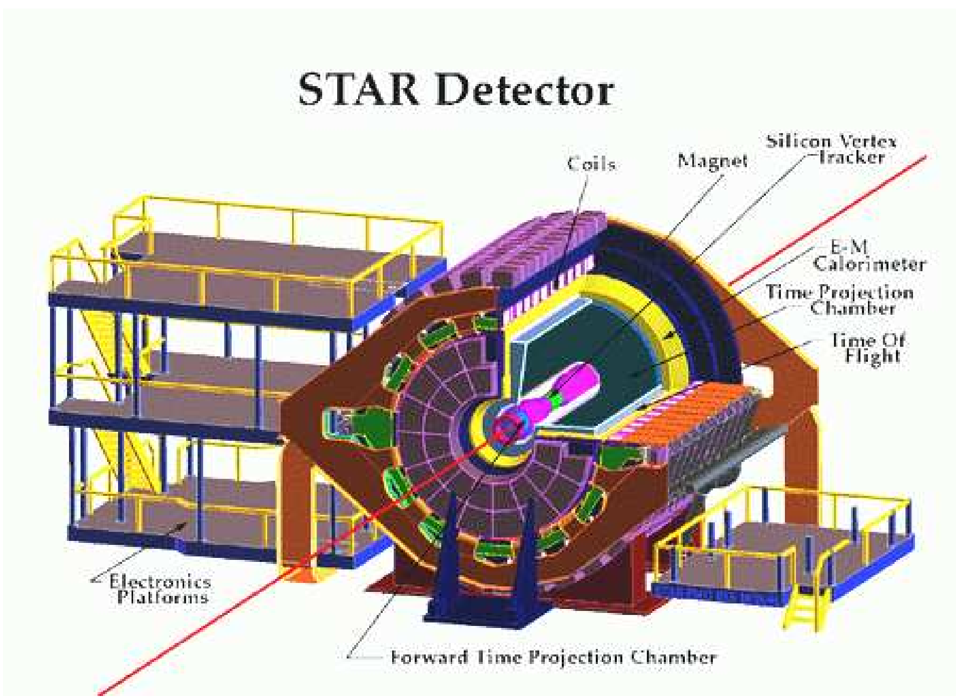

Figure 2.2: The STAR experiment.

The STAR detector (Figure 2.2) is a cylindrical detector system with 2π azimuthal coverage and contains several subsystems:

- Time Projection Chamber (TPC) [Ack99];
- Silicon Vertex Tracker (SVT);
- Forward Time Projection Chamber (FTPC);
- Electromagnetic Calorimeter (EMC);
- Time of Flight (TOF);
- Zero Degree Calorimeters (ZDC);
- other trigger detectors.

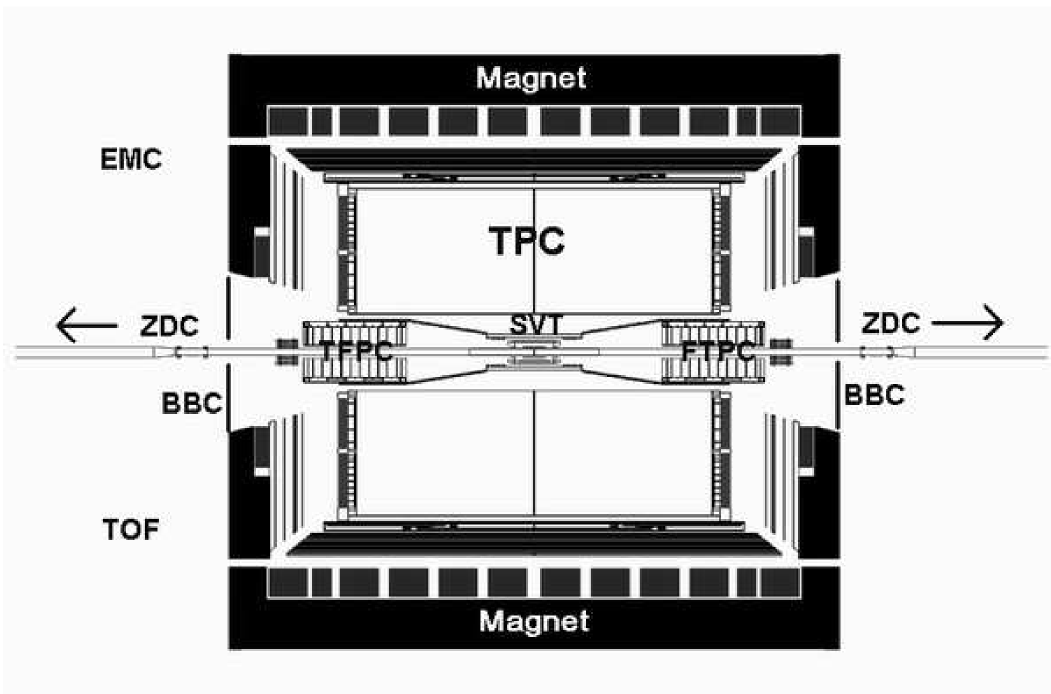

Figure 2.3: Side view of the STAR detector including the major detectors, Time Projection Chamber (TPC), Silicon Vertex Tracker (SVT), Forward Time Projection Chamber (FTPC), Time of Flight (TOF), Electromagnetic Calorimeter (EMC) and Zero Degree Calorimeters (ZDC). Other trigger detectors are not labelled.

The detector system(cross section view Fig. 2.3) is surrounded by a magnet which provide uniform fields along the beam direction with an adjustable strength, 0.25 Tesla (Half Field) to 0.5 Tesla (Full Field).

The detector can identify most of the charged particles at mid-rapidity in the main TPC that covers the pseudo-rapidity range $|\eta| < 1.8$. Four kinds of charged particles, $\pi^+(\pi^-)$, $K^+(K^-)$, $p(\bar{p})$, $e(\bar{e})$ can be identified via the measurement of ionization energy loss (dE/dx) of the particle travelling across the TPC. Pions and kaons can be identified at $p < 0.7$GeV/c and kaons and protons at $p < 1.0$GeV/c. The TOF detector now under construction can help push these two momentum limits up to 1.5 GeV/c and 3.0 GeV/c, respectively. Figure 2.4 shows identified bands for these charged particles from the TPC dE/dx and TOF $1/\beta$ measurements.

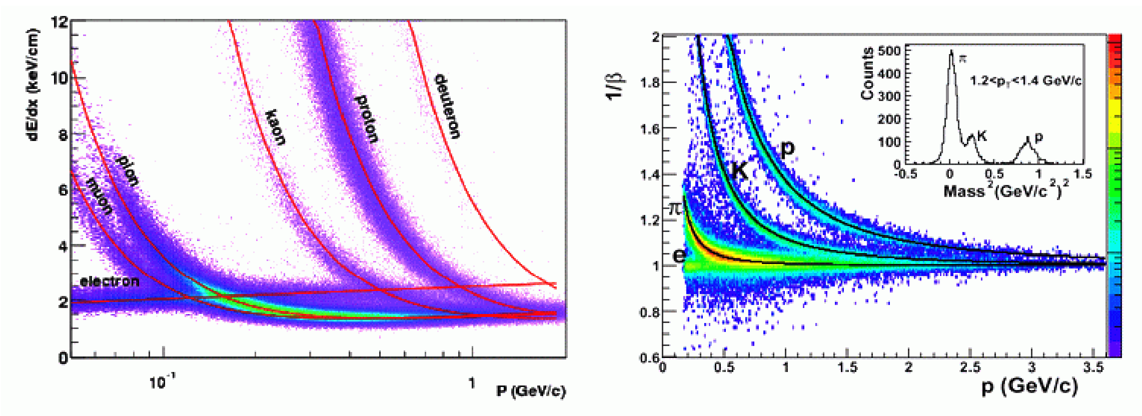

Figure 2.4: Charged particle identification at STAR. The left is particle ionization energy loss (dE/dx) as a function of momentum(p) measured in the TPC. The right is $1/\beta = tc/L$(t is time interval for a particle travelling from the collision point to the time-of-flight tray, L is path length from the collision point to the time-of-flight tray) as a function of momentum measured with TOF detector.

Other neutral and charged particles, like the K_s^0, ϕ, $\Lambda(\bar{\Lambda})$, $\Xi^-(\bar{\Xi}^+)$ and $\Omega^-(\bar{\Omega}^+)$ are reconstructed according to their weak decay channels [Col92]. These reconstructed particles can be identified at much higher p_T region. In this thesis, we have measured K_s^0 and $\Lambda(\bar{\Lambda})$ up to $p_T = 6$ GeV/c and $\Xi^-(\bar{\Xi}^+)$ $p_T = 5$ GeV/c using *weak decay topology cuts*. The vector meson ϕ can be measured up to $p_T = 6$ GeV/c using *event-mixing technique*. The EMC, designed to measure high energy($\geq$ 2GeV) electrons and photons, is used to identify some particles decaying to electrons and photons, such as π^0, η and J/ψ.

2.2.1 Time Projection Chamber (TPC)

The TPC (Figure 2.5) is the STAR main tracking detector that has two longitudinal drift chambers each 2.1 m long divided by a high voltage (28 kV) membrane. The inner and outer radii of the field cages are 50 cm and 200 cm respectively. 24 anode pad sectors for signal recordings are installed at both end-caps of the TPC cylinder between the inner and outer filed cages.

The chamber is filled with a gas mixture of 90% Argon and 10% Methane. The choice of the Methane gas for the TPC was made as a compromise among the following ten features [Col92]:

1. The gas mixture has to work at atmospheric pressure ;
2. The electron drift velocity must be > 2.0 cm/μs at $E < 300$ V/cm ; The field limit is determined by the tolerances of the insulators on the field cages;
3. At nominal field, the drift velocity should be saturated to reduce the effects from inhomogeneities in the E field and variations from gas pressure (gas pressure changes with atmospheric pressure);
4. Small transverse and longitudinal diffusion;
5. Large $\omega\tau$, to reduce transverse diffusion;

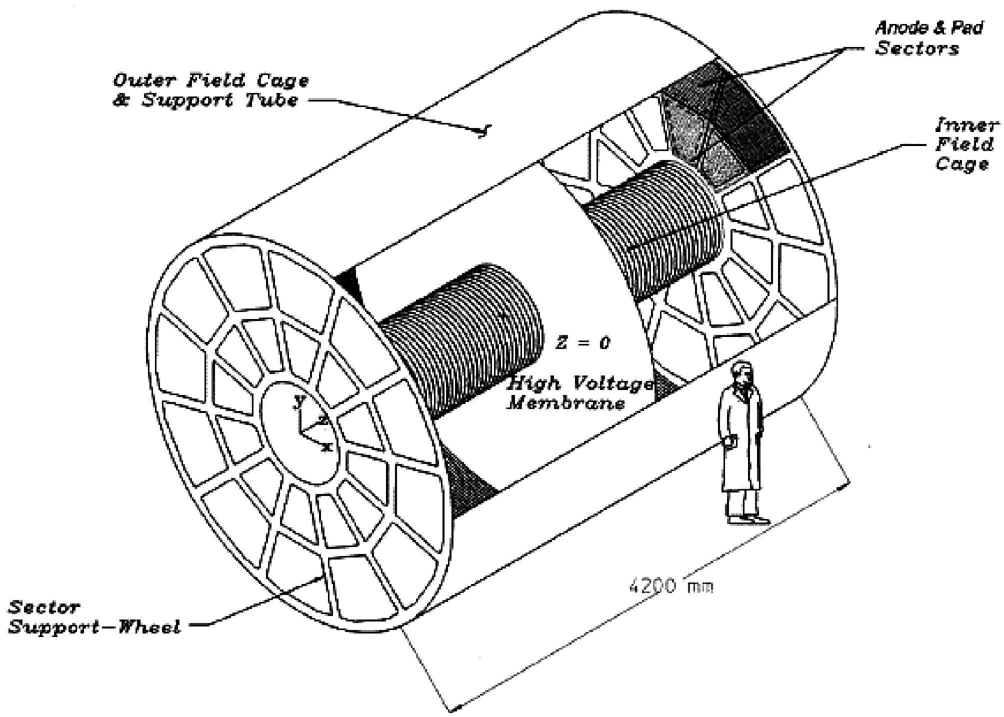

Figure 2.5: The STAR Time Projection Chamber(TPC).

6. High ionization efficiency;

7. Low electron absorption over drift length;

8. High drift velocity for positive ions in order to minimize the space charge accumulation;

9. Low rate of aging and high resistance to high voltage breakdown;

10. Gas should be cheap, safe and affordable in large quantities.

When a high velocity charged particle travels through the gas-filled TPC volume, the gas molecules will be ionized and produce positive ions and electron clouds along the path. The energy loss due to ionization is typically a few KeV per cm of gas. This gives a total energy loss of a few MeV over a path length of 2 m, which is negligible compared with the typical kinetic energy of a particle (above 100 MeV). Under the influence of the electric field in the TPC, ionized electrons drift to one end of TPC and positive ions drift in the opposite direction to the central membrane. The arrival time and locations of the electron clusters are recorded by the electronics system at the anode sectors.

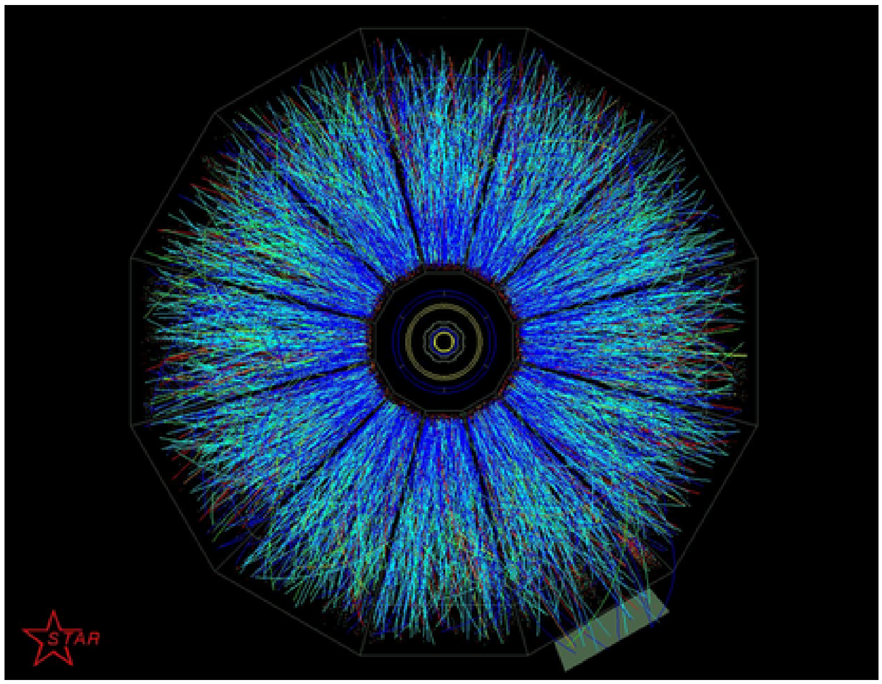

Figure 2.6: First Gold-Gold Collision Events at RHIC at full energy $\sqrt{s_{NN}}$= 200 GeV recorded by STAR. Front view of Time Projection Chamber (TPC).

The TPC can record tracks up to $\sim 4 \times 10^3$ particles per event in Au+Au collisions. Figure 2.6 illustrates the reconstruction of a large number of charged particles produced from central Au+Au collisions in the STAR Time Projection Chamber(TPC). The number of tracks per event (multiplicity) in Au+Au collisions is much higher than that in d+Au collisions.

Each end-cap of the TPC is instrumented with 70,000 pads. Two pad sizes are used, one for the inner sectors (50 cm < radius < 125 cm) and one for the outer

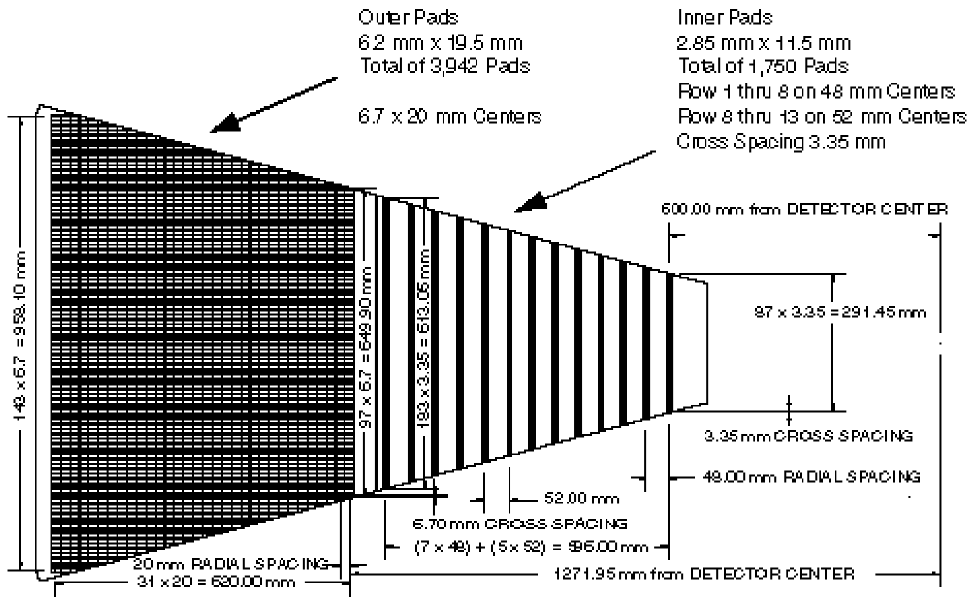

Figure 2.7: A TPC pad plane with one full sector which consists of an inner subsector and an outer subsector. The inner subsector is on the right and has small pads arranged in widely spaced rows. The outer subsector is on the left and is densely packed with larger pads.

sectors (125 cm < radius < 200 cm) as shown in Figure 2.7. The inner sector is made of 13 pad rows and the outer sector 32 rows. A track passing through both sectors can be recorded by up to 45 points, leading to a good ability in particle identification by ionization energy loss. The sizes of pads are designed according to the required position resolution along pad row direction. The inner pads with a smaller size of 2.85 mm × 11.5 mm can provide a better two track resolution than the outer pads with a size of 6.2 mm × 19.5 mm, which is necessary for the region in high track density.

2.2.2 Forward Time Projection Chamber (FTPC)

The physics goal in building an FTPC sub-system is to extend the rapidity coverage of the STAR tracking system. FTPC (Figure 2.8) is a high-resolution Time

Projection Chamber for tracking charged particles within the pseudo-rapidity $|\eta|$ = 2.5 - 4, azimuthal angle ϕ = 0-360 deg, and transverse momentum p_T of several GeV/c. The detector was filled with 50%/50% mixture of Ar and CO_2, non-flammable gases. Unlike the TPC where the readout anode pads are placed on both ends so that the drift field is in the beam direction, the FTPC is a radial drift field detector where ionized electrons move radially to the readout pads. The high voltage electrode surrounds the beam pipe at a radius of 8cm and a potential of -10KV and the Frisch grid is placed at a radius of 30cm and a potential of zero voltage. Towards both ends of the detector, 17 aluminum rings are set to potentials equivalent to a radial field by a divider chain to shield the electric field in the TFPC against disturbances from the outside.

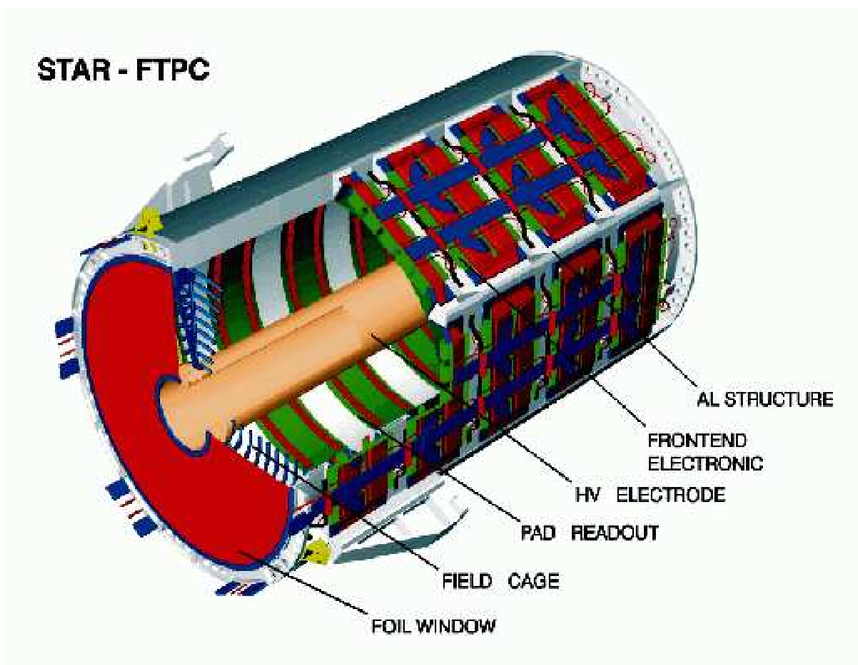

Figure 2.8: The STAR Forward Time Projection Chamber (FTPC).

Two FTPCs are located inside the STAR solenoid magnet symmetrically with respect to the center of the detector. They have a sensitive volume of r = 8 -

30 cm and $|z|$ = 160 - 260 cm. Making use of the STAR magnetic field, the FTPC can achieve a typical momentum resolution around 12% and discriminate between positive and negative charges.

For the d+Au run in 2003, the event centrality definition was made according to the measured multiplicity in the East (Au side) FTPC instead of that in the TPC where most main physical analysis was done. This selection avoids the auto-correlations that may occur if both physical analysis and centrality measurement are done in the same rapidity region.

2.2.3 Time-Of-Flight (TOF)

The purpose of the time-of-flight detector is to extend the particle identification capabilities of the STAR detector to high transverse momentum as shown in Fig.2.4.

The full time-of-flight coverage requires 120 TOF trays(TOFr), 60 in the east ($0 < \eta < 1$) and 60 in the west ($-1 < \eta < 0$). Each tray contains 32 multi-gap resistive plate chambers (MRPC) that provide a cost-effective solution for large-area time-of-flight coverage. The MRPC is basically a stack of resistive plates arranged in parallel. The utility of resistive plates is to quench the streamers so that they do not initiate a spark breakdown. The intermediate plates create a series of gas gaps. Electrodes are connected to the outer surfaces of the two outer plates. A strong electric field is created in each subgap when a high voltage is applied to these electrodes. All the internal plates are electrically floating; they initially take the voltage as defined by electrostatics, but are kept at the correct voltage by the flow of electrons and ions produced in the gas by avalanches.

For d+Au run in 2003, only 28 MRPCs were installed in a tray and 12 out of 28 were instrumented with electronics, equivalent to 0.3% of full coverage.

2.2.4 Electromagnetic Calorimeter (EMC)

The electromagnetic calorimeter (EMC), designed to measure and trigger on the total and local transverse energy deposition in collisions, extends the capabilities of STAR to study direct photons, neutral pions, jets, and high p_T particle spectra. There are two types of EMC: the Barrel EMC (BEMC) provides full azimuthal coverage in $-1 < \eta < 1$ and the Endcap EMC(EEMC) extends the rapidity coverage to $\eta = 2$.

The BEMC is a lead-scintillator sampling calorimeter. It is located inside the large room temperature magnet within a cylindrical space approximately 41cm deep, by 6.2m in length, sandwiched between the Time of Flight system and the magnet coils. It includes a total of 120 calorimeter modules, each subtending 6^o in $\Delta\phi$(0.1 radian) and 1.0 unit in $\Delta\eta$. These modules are mounted 60 in ϕ by 2 in η. The detector has the ability to separate high energy direct photons from π^0 decays. For the d+Au run in 2003, only half of BEMC modules were installed, covering 2π in azimuth and $0 < \eta < 1$.

The EEMC with the coverage $1 < \eta < 2$ in pseudorapidity and 2π in ϕ was subdivided into 720 projective towers, with 12 segments covering the η range and 60 segments in ϕ. Each tower has independent readout. The η range covered by each tower will gradually increase from 0.057 at $\eta = 1$ to 0.099 at $\eta = 2$. It includes a scintillating-strip shower-maximum detector to provide π^0/γ discrimination and preshower and postshower layers to aid in distinguishing between electrons and charged hadrons.

2.2.5 Trigger Detectors

The detectors with fast readout times are used for triggering events to decide whether they should be recorded or not. They include a Central Trigger Barrel (CTB) around the TPC at $|\eta| < 1$, Beam-Beam Counters (BBC) at both sides of the STAR detector and two zero-degree calorimeters (ZDC West and ZDC East) located in the forward direction at $\theta < 2$ mrad and 18 meters away from the interaction point.

The CTB consists of 240 scintillator slats covering the outer shell of the TPC. Each slat consists of a scintillator, light guide, and photomultiplier tube (PMT). Each ZDC consists of three modules. Each module consists of a series of tungsten plates alternating with layers of wavelength shifting fibers that route Cherenkov light to a PMT.

The CTB triggers on the flux of charged particles in the midrapidity region. The ZDCs are used for determining the energy of neutral particles (mainly dissociated neutrons not participating in the collision) remaining in the beam direction while all charged particles are deflected away by dipole magnets (DX) located between interaction region and ZDCs.

A minimum bias trigger for d+Au run in 2003 was based only on the signals received in the East (Au side) ZDC due to the low reception rate in the West (deuteron side) ZDC. The minimum bias d+Au data requires at least one beam-rapidity neutron in ZDC-Au.

CHAPTER 3

Analysis Methods

In the STAR TPC, four particles (electrons, pions, kaons and protons) in the low p_T region can be identified through their energy loss rate(dE/dx) along their track in the TPC, while other particles are reconstructed from them through decay channels. K_S^0, Λ, Ξ^- and their anti-particles decay to pions and protons through their weak decay channels. These decays involve a relatively long decaying time leading to a large decay length. Therefore, the daughter particles (pions and protons) were created at some point in space away from the primary vertex. This feature can be used to get rid of much background and makes these strange hadrons easy to reconstruct.

3.1 d+Au minimum bias data

For the d+Au run at $\sqrt{s_{NN}}$=200 GeV at RHIC in 2003, about 22 million experimental data were recorded by the STAR detector. The minimum bias data, accepting (95±3)% of the d+Au hadronic cross section, are triggered by requiring at least one beam-rapidity neutron in the gold side of ZDC. To remove trigger biases, the minimum bias data also require a vertex-z cut within 50 cm of the TPC center. Moreover, primary vertices (collision points) were not successfully reconstructed in some events due to the low multiplicity (number of particles from one event) in the TPC so that these events are useless. After discarding these events, we have ~ 10 million d+Au minimum bias events from the newest production P04f for our analysis. In order to estimate the systematic errors, the data were taken under the full magnetic field (0.5 Tesla) in two opposite directions. There are three data sets containing d+Au minimum bias events: dAuMinBias, dAuCombined and UPCCombined. Fig. 3.1 shows the vertex-z distributions for minimum bias events of three data sets in the full field(FF) and the reversed full field(RFF). Table 3.1 lists the selection criteria for minimum bias events in the analysis.

Event Selection	
Vertex-Z(cm)	$-50 < \|z\| < 50$
Primary Vertex Found	Yes
min-bias events	~ 10 million

Table 3.1: Event selection criteria for minimum bias events in d+Au collisions at $\sqrt{s_{NN}} = 200$ GeV at STAR.

3.2 Centrality definition in d+Au

Nuclear effects are different for the different collision centralities, which are related to the impact parameter b of the collision in geometry. In experiments we define the centrality according to the number of charged particles measured in a given rapidity region.

Unlike the Au+Au runs(Run-1 and Run-2) where the TPC multiplicity was adopted for the centralities, the d+Au run in 2003 uses FTPC reference multiplicity, the total number of the qualified tracks in the east(Au) side of TFPC, to define STAR's centrality intervals, avoiding the particle autocorrelation in the

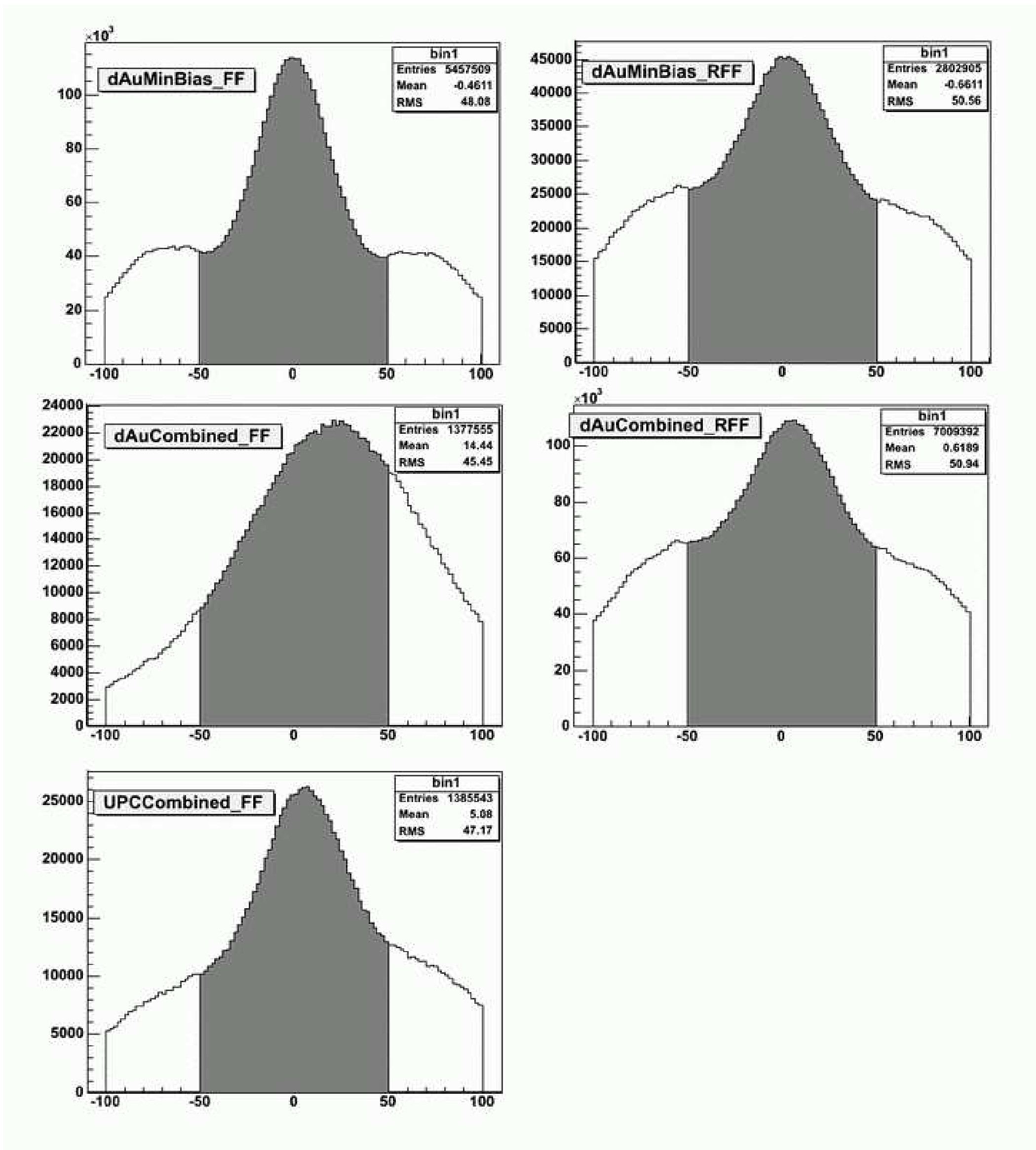

Figure 3.1: Vertex-Z distribution for three data sets (dAuMinBias, dAuCombined, UPCCombined in full field and reversed full fields) containing minimum bias events. The events in shadowed areas with $|vertex - z| < 50$ are used for our analysis.

TPC. These tracks must be from minimum bias events with primary vertex found. The qualified tracks for the centrality definition are the charged primary tracks with the following requirements:

- fit points >= 5 (>=6 included Primary Vertex)
- $-3.8 < \eta$(pseudo-rapidity)$<= -2.8$
- $p_T < 3$ GeV/c
- a distance of closest approach (DCA) to the primary vertex < 3 cm

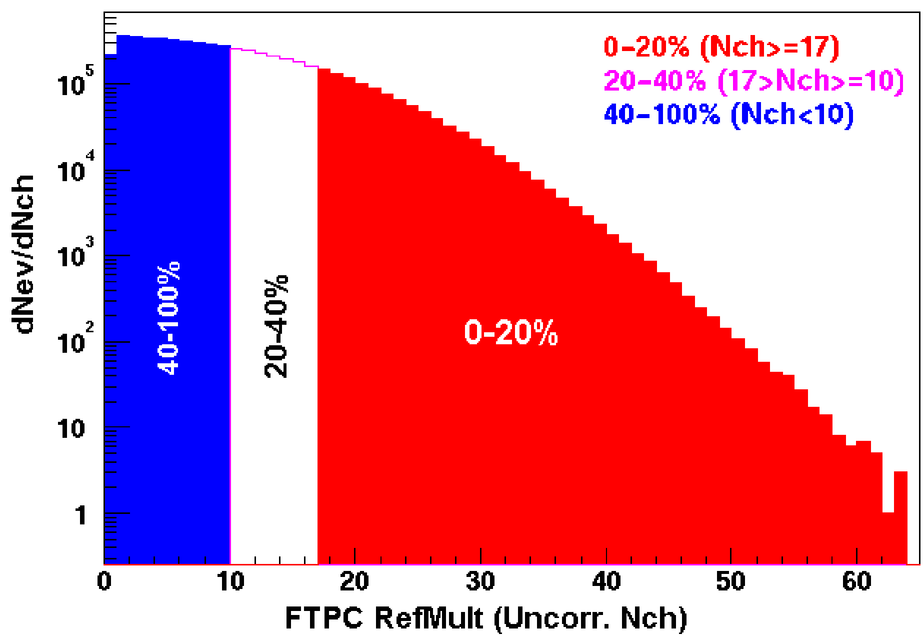

Figure 3.2: The minimum-bias primary charged track multiplicity(Nch) distribution measured in the east side(Au) of FTPC with $-3.8 <= \eta < -2.8$. The three centrality intervals are defined: $Nch >= 17, 10 <= Nch < 17$ and $0 <= Nch < 10$ corresponding to 0-20%, 20-40% and 40-100% of the total cross section, respectively.

According to the uncorrected FTPC reference multiplicity (Nch), we have three centrality intervals: $Nch >= 17, 10 <= Nch < 17$ and $0 <= Nch < 10$

corresponding to 0-20%, 20-40% and 40-100% of the total cross section for d+Au collisions, respectively as shown in Figure 3.2.

Centrality Bin	Uncorr. FTPC RefMult	Uncorr. $\langle N_{ch} \rangle$	$\langle N_{binary} \rangle$	$\langle N_{part} \rangle$
minibias	RefMult >= 0	10.2	7.5±0.4	8.0
0-20%	RefMult >= 17	17.58	15.0±1.1	14.5
20-40%	10 <= RefMult < 17	12.55	10.2±1.0	10.8
40-100%	0 <= RefMult < 10	6.17	$4.0^{+0.8}_{-0.3}$	5.1

Table 3.2: The average uncorrected FTPC reference multiplicity($\langle Nch \rangle$), the average number of participating nucleons($\langle N_{part} \rangle$) and of binary collisions($\langle N_{binary} \rangle$) for three centralities and minimum bias taken from HIJING.

In nuclear collisions, each collision may involve many participating nucleons and many binary(nucleon-nucleon) collisions. These numbers reflect the collision properties and are closely related to the centralities and often used as normalization factors when comparing nuclear effects among different systems. Table 3.2 lists the average uncorrected FTPC reference multiplicity($\langle Nch \rangle$), the average number of participated nucleus($\langle N_{part} \rangle$) and binary collisions($\langle N_{binary} \rangle$) for three centralities and minimum bias taken from HIJING simulation calculation for d+Au collisions.

Centrality Bin	Events (uncorrected)	Events (corrected)
mini-bias	9853182	10594819
0-20%	1910593	1910593
20-40%	2235216	2235216
40-100%	5707373	6485651

Table 3.3: Uncorrected and vertex-efficiency-corrected event numbers for three centralities and minimum bias in d+Au collisions.

In our analysis, we have the event numbers for the three centrality bins and for the minimum bias trigger listed in Table 3.3. Uncorrected event numbers refer to events with found vertex, while corrected event numbers refer to all events irrespective of whether the vertex is found or not. This will be discussed in more detail in Section 3.12.

3.3 Track Selection

There are two sets of tracks available for the analysis in the STAR. Primary tracks requiring a distance of closest approach (DCA) to the primary vertex less than 3 cm are usually used for identification of particles originating at or very close to the primary vertex. Global tracks that include all the TPC tracks are mainly used to reconstruct particles that decay at some point in space away from the primary vertex. We use global tracks in our analysis to reconstruct K_S^0, Λ, Ξ^- and their anti-particles by taking advantage of their large decay length. Tracks in the TPC are formed by fitting the measured hit points. The number of hit points for each track ranges from 8 to 45. We required at least 16 hit points for a track of good quality and discarded short tracks that might be split from a track with a large number of hit points. Due to the acceptance of the TPC detector, very low momentum tracks can not be detected. The tracks with transverse momentum less than 0.077 GeV/c were thrown away.

Track Selection	
Number of hits	> 15
Momentum (GeV/c)	$p_T > 0.077$
nσ_π in K_S^0	$\lvert n\sigma_\pi\rvert < 4$
nσ_π in $\Lambda(\overline{\Lambda})$	$\lvert n\sigma_\pi\rvert < 4$
nσ_p in $\Lambda(\overline{\Lambda})$	$\lvert n\sigma_p\rvert < 4$
nσ_π (second pion) in $\Xi^-(\overline{\Xi}^+)$	$\lvert n\sigma_\pi\rvert < 4$

Table 3.4: Track selection criteria for reconstructing K_S^0, Λ, Ξ^- and their anti-particles in d+Au collisions at $\sqrt{s_{NN}} = 200$ GeV at RHIC STAR. The more effective topology cuts will be applied to reconstruct these particles.

To reduce the background for these reconstructed particles, the nσ criterion (a parameter describing how far the measured dE/dx deviates from the theoretical value of a known particle) cuts on their daughter tracks is used. Because of the good quality of the dE/dx calibration for 04f d+Au production, a 4 nσ cut is enough to ensure not losing possible signals. Table 3.4 lists the selection criteria for tracks in the analysis. We also tried other dE/dx cuts to see the corresponding yield changes and to estimate the systematic errors. This will be discussed in the next chapter.

3.4 K_S^0 and $\Lambda(\overline{\Lambda})$ Reconstruction

We identify these V0 particles, K_S^0, Λ and $\overline{\Lambda}$, from their charged daughter tracks that were identified by dE/dx measurements. The weak decay channels used in our analysis and their corresponding branching ratios are listed in Table. 3.5

Particles	Decay Channel	Branching ratio
K_S^0	$\pi^+\pi^-$	68.61%
Λ	$p\pi^-$	63.9%
$\overline{\Lambda}$	$\overline{p}\pi^+$	63.9%

Table 3.5: Weak Decay Mode for V0 particles.

The fact that V0 particles decay at some point away from the primary vertex allows us to build the signals by applying appropriate topology cuts. Figure 3.3 shows a V0 decay topology projected onto the X-Y plane. The trajectory of the charged daughter tracks, P+ (positive) or P- (negative), is a helix, that is, a circle in the X-Y plane plus a constant velocity in the Z direction.

To find V0s, we first need to calculate the distance of closest approach (DCA) between two daughter tracks (DCA_P+_P-). Theoretically DCA_P+_P- should be zero if two daughter particles are decayed from the V0. Practically a distance tolerance is, however, allowed due to the track position resolution. We allow this DCA to be less than 1 cm. The detailed math derivation for calculating

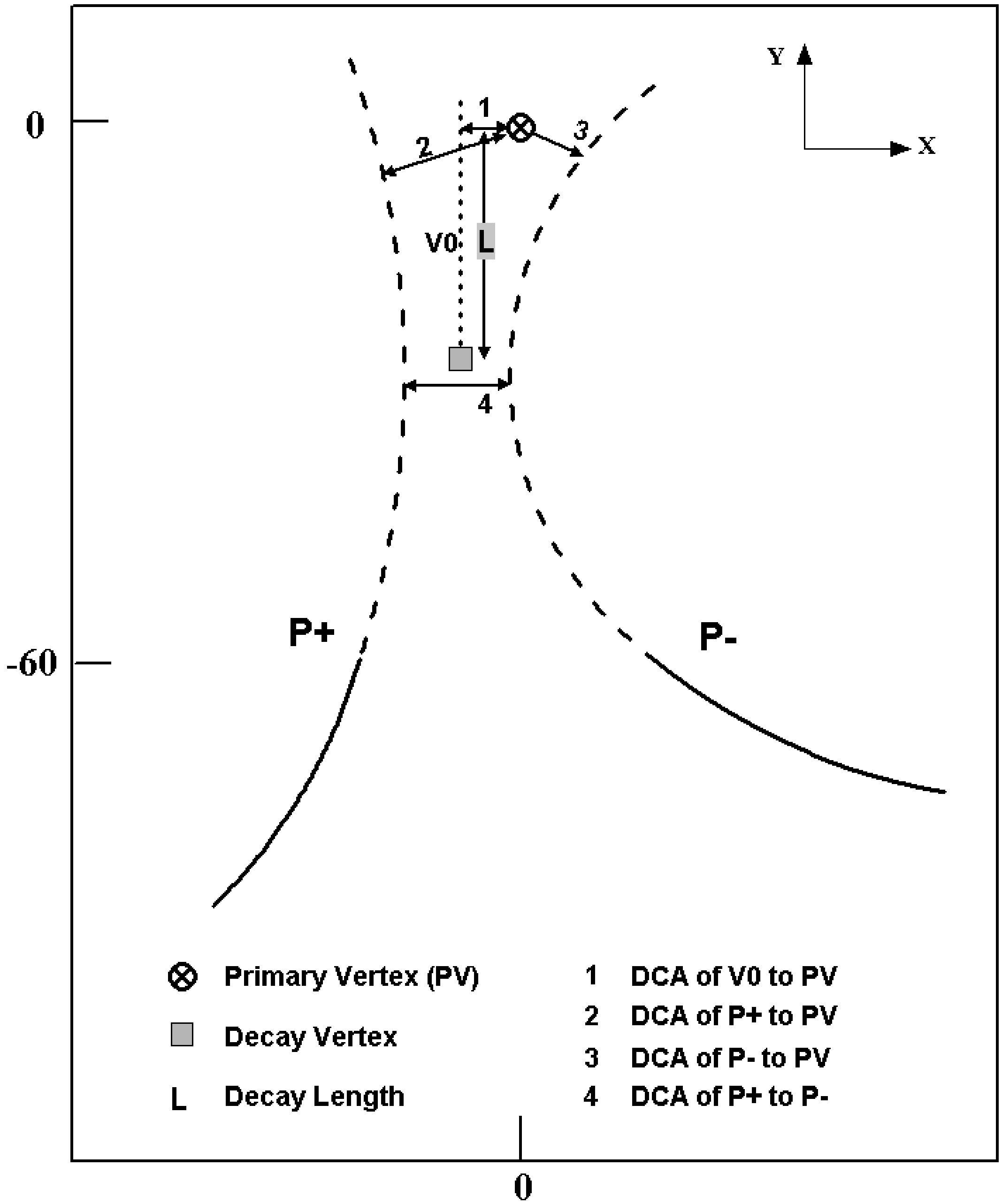

Figure 3.3: The V0 particle (Λ or K_S^0) decay topology in X-Y plane. P+ refers to a positive particle and P- a negative particle. The solid part of a line is detectable by the TPC anode sectors which is 60 cm away from the beam line. The dash parts of the lines are either extrapolated from the solid part(as P+ and P-) or reconstructed from daughter tracks (as V0)

DCA_P+_P- was published in Hui Long's thesis [Lon02].

Similarly, a tolerance is applied to the DCA between the V0 and the primary vertex (DCA_V0_PV) even for a V0 coming from the primary vertex. All the K_S^0 particles are assumed to have been produced at the primary vertex, so we set the limit for K_S^0 DCA_V0_PV as 1 cm. However, some of Λs($\overline{\Lambda}$s) can be produced at the secondary vertex via the $\Xi(\overline{\Xi})$ weak decay channel, which forces us to use a larger DCA_V0_PV cut. In the analysis, we set the limit as 5 cm for the inclusive Λs($\overline{\Lambda}$s).

The other two DCAs, DCA of P+ to primary vertex (DCA_P+_PV) and DCA of P- to primary vertex (DCA_P-_PV), can be used to reduce the background efficiently by cutting away a large portion of primary tracks which have small DCA_P+_PV or DCA_P-_PV. For the V0 reconstruction in Au+Au collisions, these two DCAs have to be applied to build the acceptable signals. However, it turns out that they are not necessary in d+Au analysis due to much smaller combinatorial background. Compared with 5000 tracks produced in some central Au+Au events, the maximum number of tracks produced in d+Au events is only about 500.

The momentum direction of the V0 is determined by adding up the momenta of track P+ and track P- at the decay vertex. The decay length is calculated as the distance between the decay vertex and the primary vertex.

Table 3.6 lists the topology cuts used for the spectra and R_{CP} analysis. These topology cuts are applied to maximize the signal-to-background ratio in the invariant mass plots. If a V0 candidate passes these cuts, its invariant mass(m) is calculated assuming hypothetic mass values for daughter tracks:

$$m = \sqrt{\left(\sqrt{m_+^2 + P_+^2} + \sqrt{m_-^2 + P_-^2}\right)^2 - P^2}, \tag{3.1}$$

where $m_+(m_-)$ is the mass of the positive(negative) track, P_+, P_- and P are the momenta of the positive daughter track, the negative daughter track and the V0 at the decay vertex, respectively. For example, m_+ is the proton mass and m_- is the pion mass for the Λ reconstruction.

Topology Cuts for K_S^0		
K_S^0 p_T (GeV/c)	< 3.5	$>= 3.5$
DCA of π^+ to primary vertex (cm)	$>= 0.5$	$>= 0$
DCA of π^- to primary vertex (cm)	$>= 0.5$	$>= 0$
DCA of K_S^0 to primary vertex (cm)	$<= 1.5$	$<= 1.5$
DCA of π^+ to π^- (cm)	$<= 1.0$	$<= 1.0$
Decay Length (cm)	$>= 2.0$	$>= 5.0$
Topology Cuts for Λ		
Λ p_T (GeV/c)	< 2.0	$>= 2.0$
DCA of proton to primary vertex (cm)	$>= 0.5$	$>= 0$
DCA of π^- to primary vertex (cm)	$>= 1.5$	$>= 0$
DCA of Λ to primary vertex (cm)	$<= 5.0$	$<= 5.0$
DCA of proton to π^- (cm)	$<= 1.0$	$<= 1.0$
Decay Length (cm)	$>= 3.0$	$>= 6.0$

Table 3.6: Topology Cuts for K_S^0 and $\Lambda+\overline{\Lambda}$ final spectra and R_{CP}. The cuts used ensure a high signal-to-background ratio in the invariant mass plots. The same cuts are used for $\overline{\Lambda}$.

3.5 K_S^0 and $\Lambda+\overline{\Lambda}$ Invariant Mass Distributions

The K_S^0, Λ and $\overline{\Lambda}$ particles are not identified on a particle-by-particle basis. There is a large background from random combinations of unidentified daughter particles or of uncorrelated identified daughter particles. However, the yield can be estimated by counting the candidates within a mass window around the center of the signal peak above a fitted background line. A possible way [Lon02, Kop74] to determine the background is to rotate all positive tracks 180 degrees in the azimuthal plane with respect to the primary vertex. This procedure destroys all the secondary vertices and only combinatorial background is reconstructed for the invariant mass distribution. This method has been successfully used on the V0 analysis for the Au+Au collisions [Lon02, Sor03]. For our d+Au analysis, the signal-to-background ratio is large enough even without a rotated background subtraction. We use a combination of a Gaussian function and a second order polynomial function to fit the invariant mass distribution for each p_T interval. To increase the statistics, we combine the Λ and $\overline{\Lambda}$ yields. Figure 3.4 shows the K_S^0 invariant mass distributions in six selected p_T bins at mid-rapidity ($|y| < 1.0$) for the minimum bias events, and Figure 3.5 shows similar Λ+$\overline{\Lambda}$ invariant mass distributions.

3.6 Background Study

The weak decay topology cuts used in the analysis reduce the background drastically since many particles produced at the primary vertex are cut away by applying the decay length and daughter track DCA cuts. However, backgrounds from other sources still need to be understood.

In d+Au collisions STAR TOF measurements [Ada05b] have shown that the proton(p) yield is about 10% of the π yield at low p_T($<$ 1 GeV/c) and the yield ratio of p/π increases with increasing p_T and is close to one at $p_T \simeq 3.0$ GeV/c [Ada05b]. For the low p_T K_S^0, a large amount of the background comes from the combinatorial contribution of uncorrelated $\pi^+\pi^-$ pairs since we use the dE/dx cuts($|n\sigma_\pi| < 4$) that ensures most of daughter tracks used are pions. Similarly for the low p_T $\Lambda(\overline{\Lambda})$, most of the background comes from the uncorrelated $p\pi^-$ pairs.

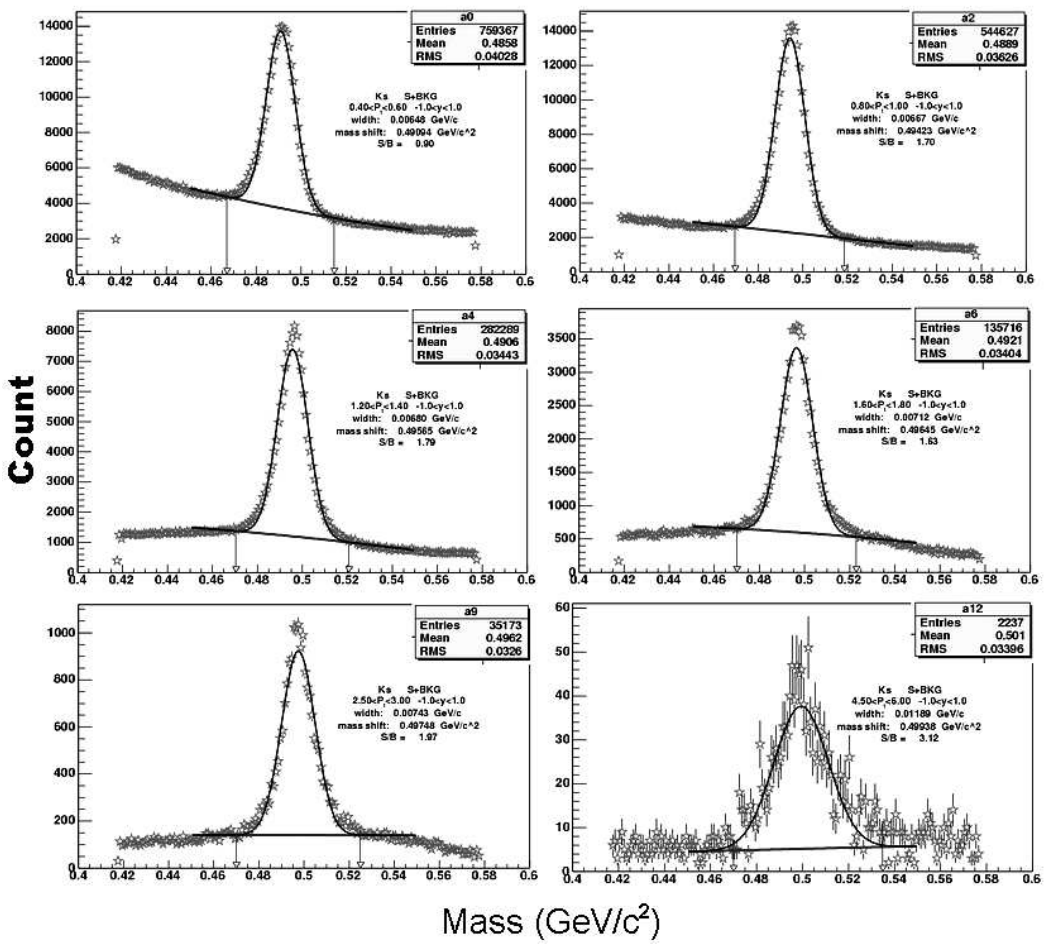

Figure 3.4: Invariant mass distributions of K_S^0 candidates at mid-rapidity ($|y| < 1.0$) from the minimum bias d+Au collisions. The selected p_T bins are (0.4-0.6), (0.8-1.0), (1.2-1.4), (1.6-1.8), (2.5-3.0) and (4.5-6.0) GeV/c. The fitting function is a gaussian function plus a 2nd order polynomial function(solid lines). The arrow lines confine the mass range for the yield extraction.

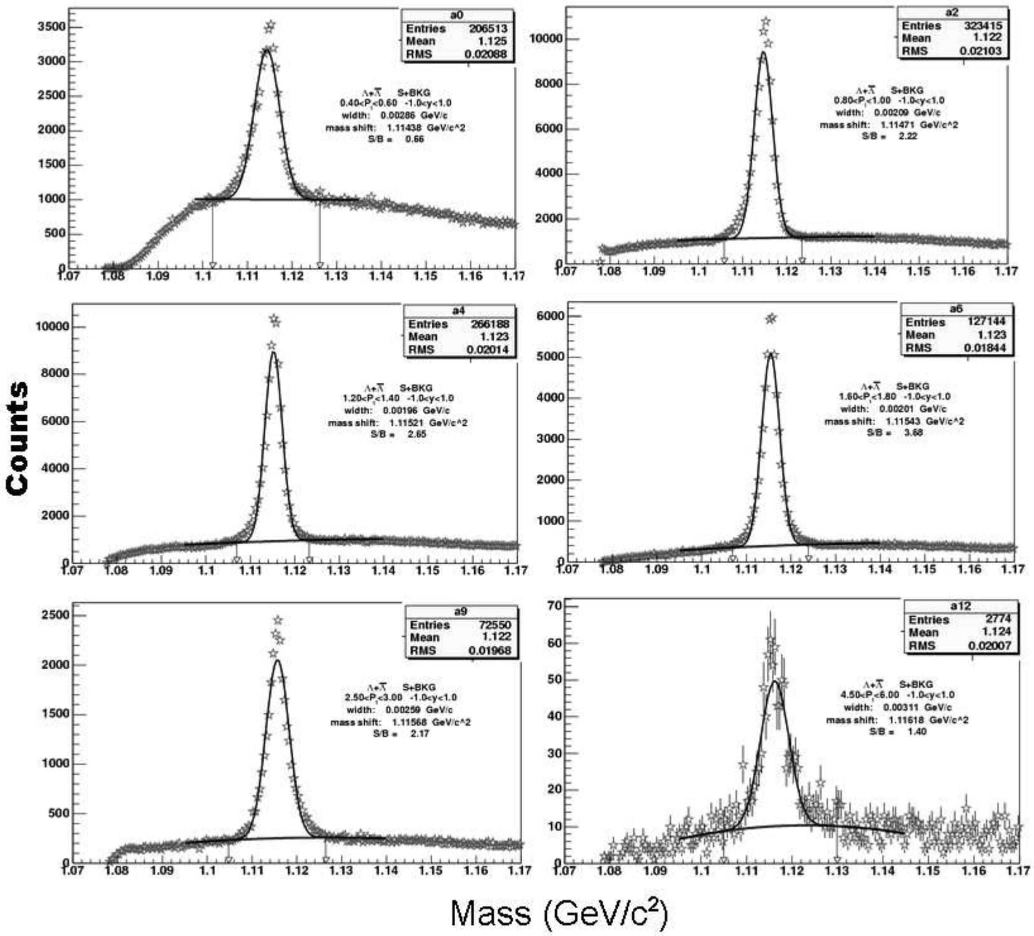

Figure 3.5: Invariant mass distributions of $\Lambda+\overline{\Lambda}$ candidates at mid-rapidity ($|y| < 1.0$) from the minimum bias d+Au collisions. The selected p_T bins are (0.4-0.6), (0.8-1.0), (1.2-1.4), (1.6-1.8), (2.5-3.0) and (4.5-6.0) GeV/c. The fitting function is a gaussian function plus a 2nd order polynomial function(solid lines). The arrow lines confine the mass range for the yield extraction.

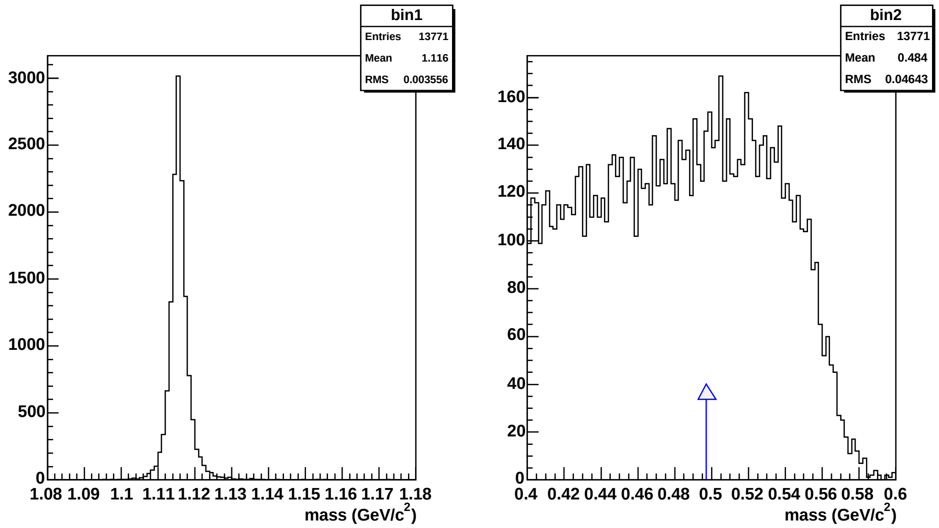

Figure 3.6: The reconstructed Monte-Carlo $\Lambda(p\pi^-)$ invariant mass(left panel)in $1.0 < p_T < 4.0$. The corresponding invariant mass distribution by replacing proton(p) in Λ with π^+(right panel). Only a small range of mass window around K^0_S mass value is shown. The arrow points to the K^0_S mass value.

Protons and pions are not distinguished from each other in the TPC for $p > 1$ GeV/c above which proton yields are comparable with pion yields. Hence, for the high p_T K^0_S, except the combinatorial background, misidentification of protons as pions from $\Lambda \rightarrow p\pi$ decays would contribute to the background. A simulation study has been performed to see the effect of daughter track misidentification. The left panel in Figure 3.6 presents the Monte-Carlo Λs reconstructed from the decay channel $\Lambda \rightarrow p\pi^-$ at $1.0 < p_T < 4.0$ GeV/c. The right panel presents the invariant mass distribution with a proton in the Λ replaced with a π^+. The $\pi^+\pi^-$ invariant mass moves toward to the lower mass value region with respect to the K^0_S mass due to the smaller Q-value(the mass difference between a particle and the total of its daughter particles) of the Λ decay than the K^0_S decay. Similarly, to understand the Λ background we have calculated the invariant mass by replacing a π^+ in the K^0_S with a proton as shown in Figure 3.7. The $p\pi^-$ invariant mass moves toward to the higher mass value. From this simulation study, we conclude misidentification of the daughter track would not produce false K_S^0 and $\Lambda(\overline{\Lambda})$ peaks.

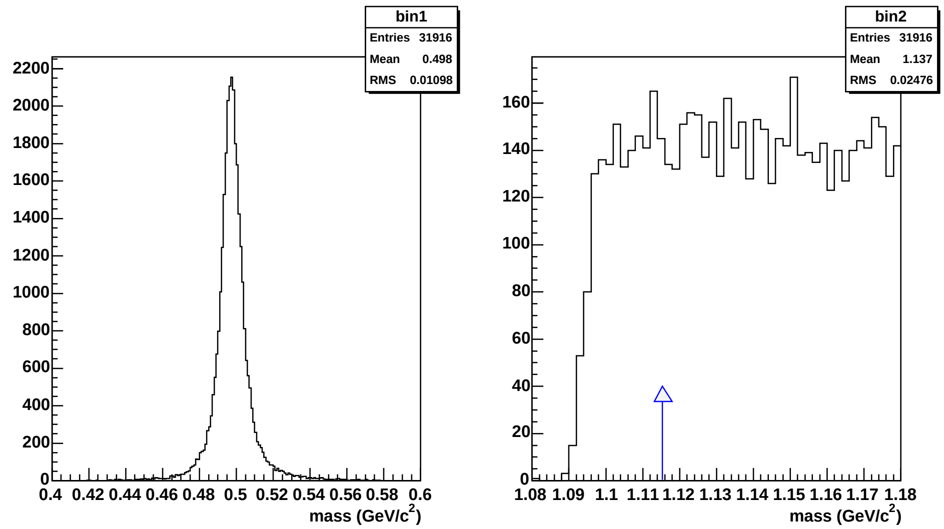

Figure 3.7: The reconstructed Monte-Carlo $K_S^0(\pi^+\pi^-)$ invariant mass(left panel)in $1.0 < p_T < 4.0$. The corresponding invariant mass distribution by replacing π^+ in K_S^0 with proton(p)(right panel). Only a small range of mass window around Λ mass value is shown. The arrow points to the Λ mass value.

3.7 Mass width and shift

We studied the mass width and shift from the invariant mass plots as a function of p_T. Because the track momentum resolution becomes worse as the increasing p_T, the half width of the mass peak (the parameter σ in Gaussian function) for K_S^0 increases from 6 MeV/c^2 at low p_T to 12 MeV/c^2 at high p_T. The half width for $\Lambda+\overline{\Lambda}$ ranges from 2 MeV/c^2 to 3 MeV/c^2 as shown in Figure 3.8.

In addition, the mass corresponding to the peak of the Gaussian function has a shift away from the PDG(Particle Data Group) mass value [Eid04] as shown in Figure 3.9. While this mass shift might partially arise from the interaction between the outgoing particles from collisions and the materials close to the beam

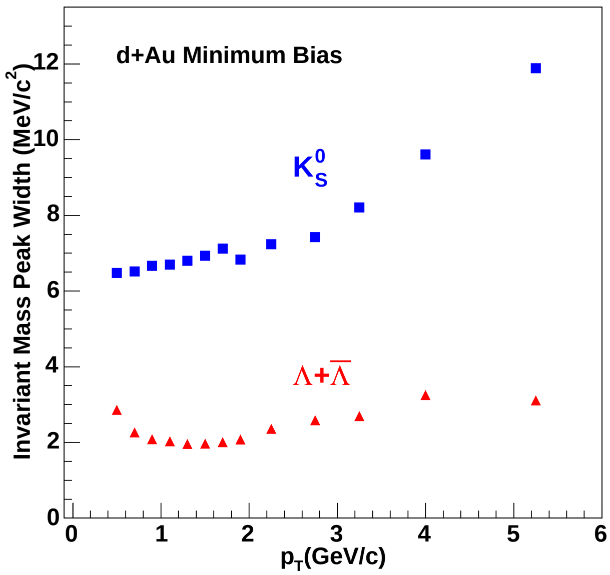

Figure 3.8: The half width of invariant mass peak for K_S^0 and $\Lambda+\overline{\Lambda}$. This half width, σ, is a parameter of the Gaussian fit function.

line in the detector, the comprehensive understanding remains unknown. Both the mass peak width and the mass shift are little dependent of the centralities in d+Au collisions.

3.8 Raw spectra of K_S^0 and $\Lambda+\overline{\Lambda}$

The raw yield can be calculated by integrating the Gaussian fit function. However, this method always under-estimates the signal under the mass peak, we use direct bin counting for the raw yield estimation. We sum the counts over all the mass bins within a mass window, $\pm 3 \sim 4\sigma$ away from the center of the peak, then subtract the counts under the background fit line within the same mass window. Finally, the summed counts are normalized to the number of events in a specific centrality.

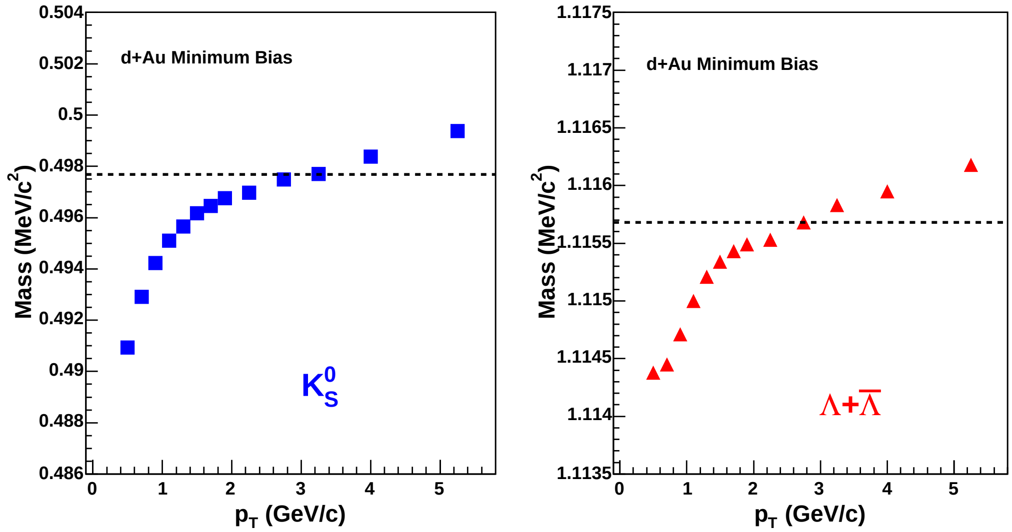

Figure 3.9: The fitted mass for K^0_S and $\Lambda+\overline{\Lambda}$ in d+Au collisions. The mass value is taken as a parameter of the Gaussian fit function. The dashed lines are the mass values for K^0_S and Λ from PDG [GG00].

Fig. 3.10 shows the raw p_T spectra for K^0_S and $\Lambda+\overline{\Lambda}$ in three centrality bins (central: 0-20%, middle: 20-40% and peripheral: 40-100%) and minimum bias events (0-100%). Due to the limit of the statistics and the detector acceptance, the measured p_T range is within 0.4-6.0 GeV/c that consists of 13 p_T intervals and the rapidity covers $|y| < 1$.

3.9 $\Xi^-(\overline{\Xi}^+)$ Reconstruction

Particles	Decay Channel	Branching ratio
Ξ^-	$\Lambda\pi^-$	99.89%
$\overline{\Xi}^+$	$\overline{\Lambda}\pi^+$	99.89%

Table 3.7: Weak Decay Mode for V0 particles.

Ξ^- and $\overline{\Xi}^+$ are reconstructed from their weak decay channels(Table 3.7). The daughter particle Λ or $\overline{\Lambda}$ is identified via the method described in the previous

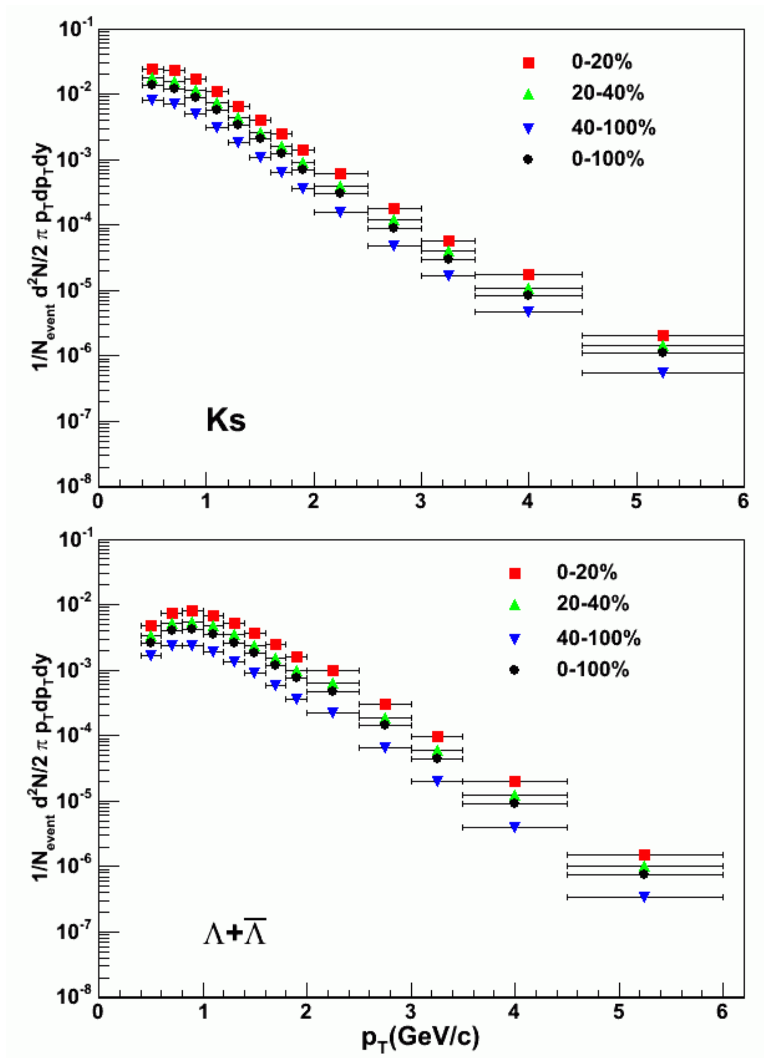

Figure 3.10: The raw spectra of K_S^0 and $\Lambda+\overline{\Lambda}$ in three centrality bins and minimum bias data. The p_T covers 0.4-6.0 GeV/c and the rapidity $|y| < 1$.

sections. The sketch of the Ξ^- decay topology is illustrated in Fig. 3.11. Its anti-particle $\overline{\Xi}^+$ has the similar decay topology simply by replacing Λ with $\overline{\Lambda}$ and π^- with π^+.

The quality and quantity of Λ candidates are two essential factors in reconstructing Ξ candidates. As Λ is not identified on a particle-by-particle basis, there is always a portion of the background entering in reconstructing the Ξ^- candidates as seen in Λ invariant mass distributions(Fig. 3.5). Getting the largest signal-to-background(S/B) ratio of Λ reduces the Ξ^- background but also the statistics. To get more Ξ^- candidates, it is not necessary to optimize the Λ S/B ratio since the combinatorial background in d+Au collisions is much smaller than in Au+Au collisions. Therefore, we adjust the cuts to enhance the signal-to-background ratio while ensuring a minimum signal loss.

Topology Cuts for Ξ^-			
Ξ^- p_T (GeV/c)	$<= 2.2$	$2.2 < p_T <= 4$	> 4
DCA of proton to PV (in Λ) (cm)	$>= 0$	$>= 0$	$>= 0$
DCA of π^- to PV (in Λ) (cm)	$>= 1.2$	$>= 0$	$>= 0$
DCA of π^- to PV (not in Λ) (cm)	$>= 0.7$	$>= 0$	$>= 0$
DCA of Ξ^- to PV (cm) 2D	$<= 1.0$	$<= 1.0$	$<= 1.0$
DCA of Λ to π^- (cm)	$<= 0.7$	$<= 0.7$	$<= 0.7$
Ξ^- Decay Length (cm) 2D	$>= 1.0$	$>= 1.2$	$>= 0$
Λ Decay Length (cm)	$>= 3.0$	$>= 3.0$	$>= 3.0$

Table 3.8: Ξ^- Topology Cuts for the final spectra and R_{CP}. Some of variables use 2 dimensional values denoted as 2D. PV means the primary vertex. The same topology cuts are used for $\overline{\Xi}^+$.

In the topology cuts for Ξ^- and $\overline{\Xi}^+$ (Table. 3.8), we use the 2 dimensional Ξ^- decay length and DCA of Ξ^- to primary vertex projected to the X-Y plane instead of their 3 dimensional values to minimize the large position uncertainty in z axis for Ξ^- candidates.

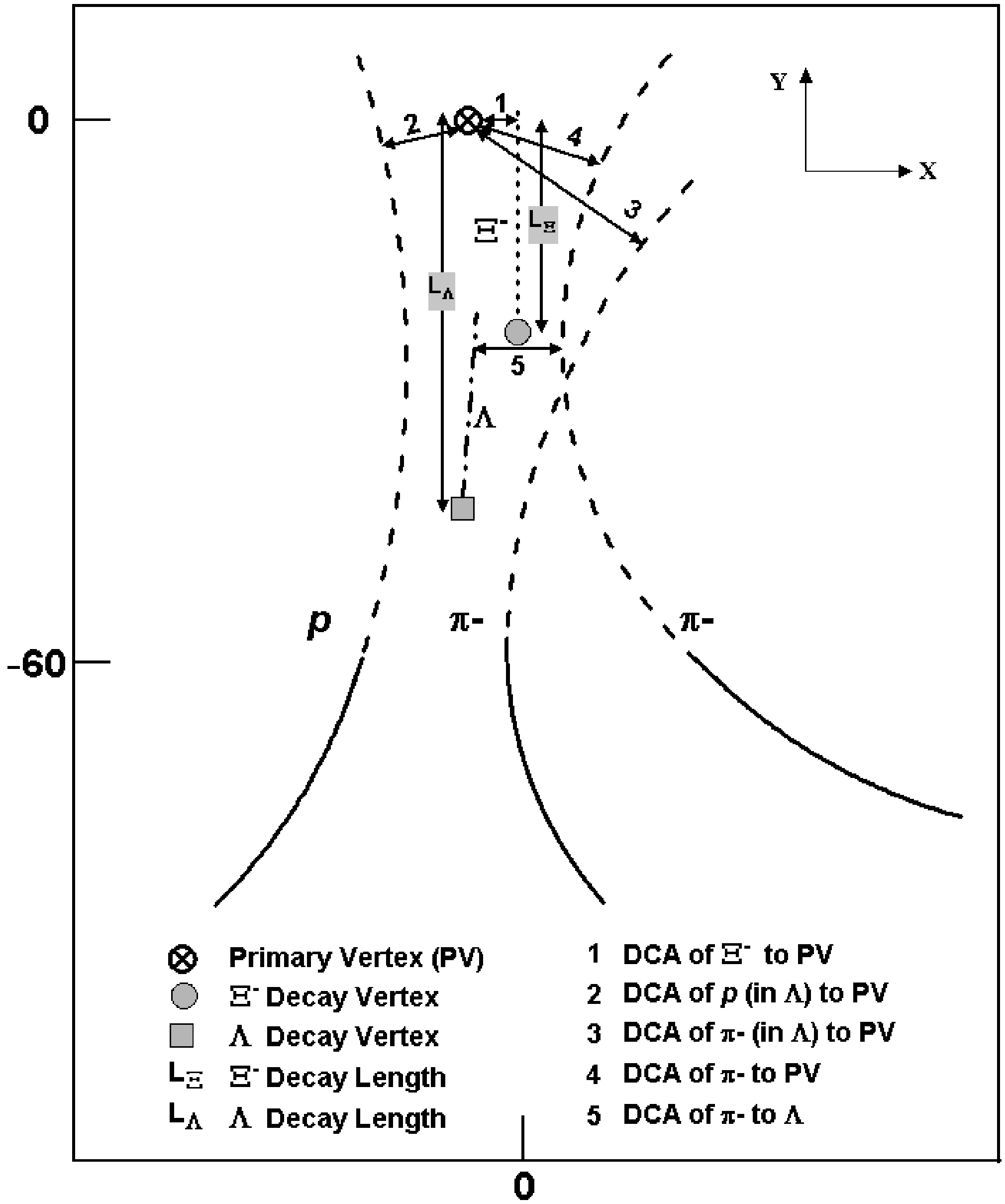

Figure 3.11: The Ξ^- decay topology in X-Y plane. The solid parts of lines are directly detected via the track dE/dx approach in the TPC. The dashed parts of the lines are either extrapolated from the solid part, like charged particles (p, π^+) or reconstructed from daughter tracks, like Λ and Ξ^-. No information for p and π^-(in Λ) are given since Λ has been reconstructed.

3.10 $\Xi^{-}+\overline{\Xi}^{+}$ Invariant Mass Distributions

Figure 3.13 shows the invariant mass distributions of $\Xi^{-}+\overline{\Xi}^{+}$ for eight p_T bins at mid-rapidity ($|y| < 1.0$) spanning a p_T range from 0.60 to 5.0 GeV/c. Again due to the small background, we do not use the rotating method and a Gaussian function plus a 2nd order polynomial function works well to fit the mass peak and the background. As shown in Figure 3.12, the half width of mass peaks(σ) in the Gaussian function ranges from 3 MeV/c at low p_T to 4.2 MeV/c at high p_T. The fitted mass values of $\Xi^{-}+\overline{\Xi}^{+}$ shift toward the lower mass region at low p_T and the higher at high p_T. The shifted amount for each p_T bin is slightly larger than that in $\Lambda+\overline{\Lambda}$ but is quite smaller than that in K^0_S.

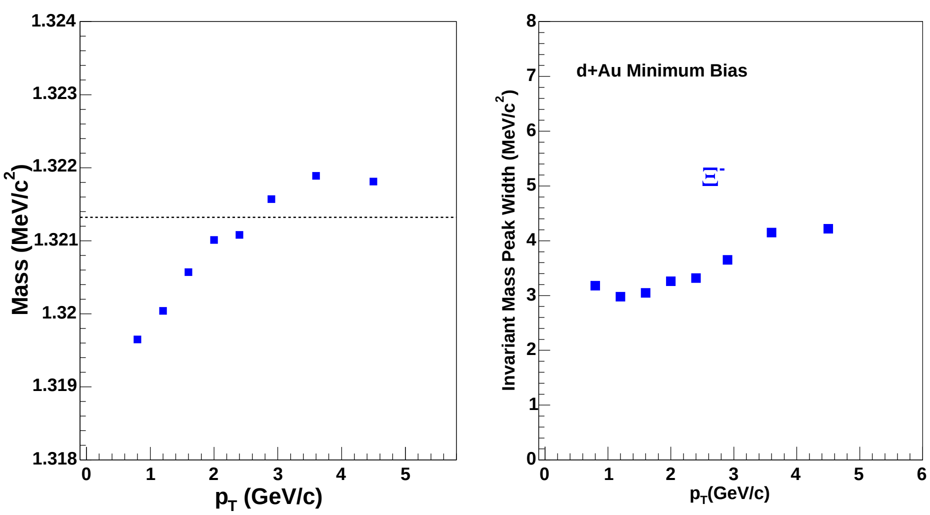

Figure 3.12: The half width of invariant mass peak(σ in the Gaussian fit function) and the fitted mass(another parameter in the Gaussian fit function) for $\Xi^{-}+\overline{\Xi}^{+}$. The dashed line in the left panel is the Ξ mass value from PDG [GG00].

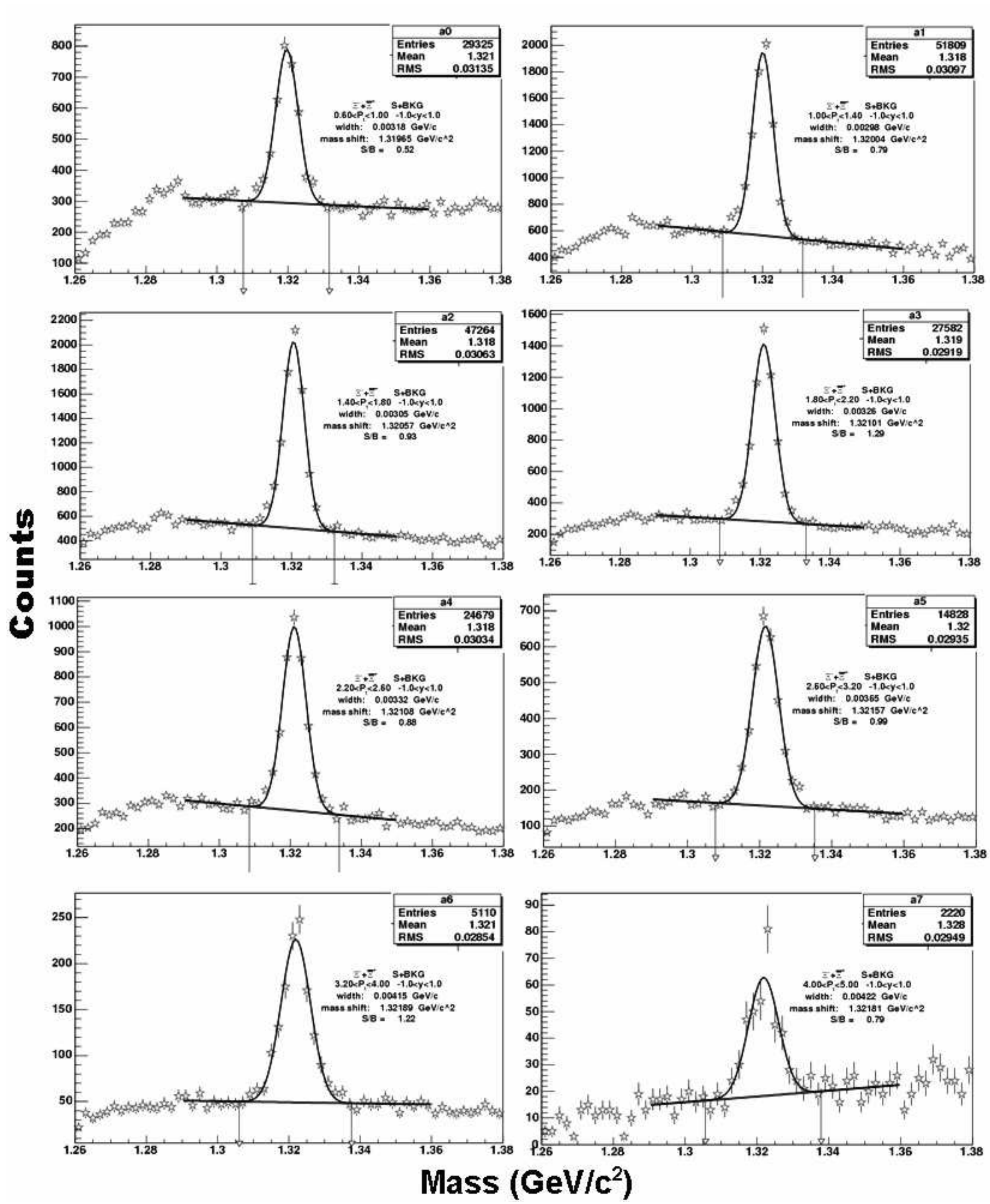

Figure 3.13: Invariant mass distributions of $\Xi^{-}+\overline{\Xi}^{+}$ candidates at mid-rapidity ($|y| < 1.0$) from the minimum bias d+Au collisions. The p_T bins are (0.6-1.0), (1.0-1.4), (1.4-1.8), (1.8-2.2), (2.2-2.6), (2.6-3.2), (3.2-4.0) and (4.0-5.0) GeV/c. The fitting function is a Gaussian function plus a 2nd order polynomial function(solid lines). The arrow lines confine the mass range for the yield extraction.

3.11 Raw spectra of Ξ^-+$\overline{\Xi}^+$

The raw yield of Ξ^-+$\overline{\Xi}^+$ takes only $\sim 2-3\%$ of the Λ+$\overline{\Lambda}$ raw yield under our cuts, making the measured p_T range for Ξ^-+$\overline{\Xi}^+$ narrower in $0.6 < p_T < 5.0$ containing 8 p_T intervals. Figure 3.14 shows the raw spectra of Ξ^-+$\overline{\Xi}^+$ in three centralities and minimum bias events at mid-rapidity $|y| < 1$.

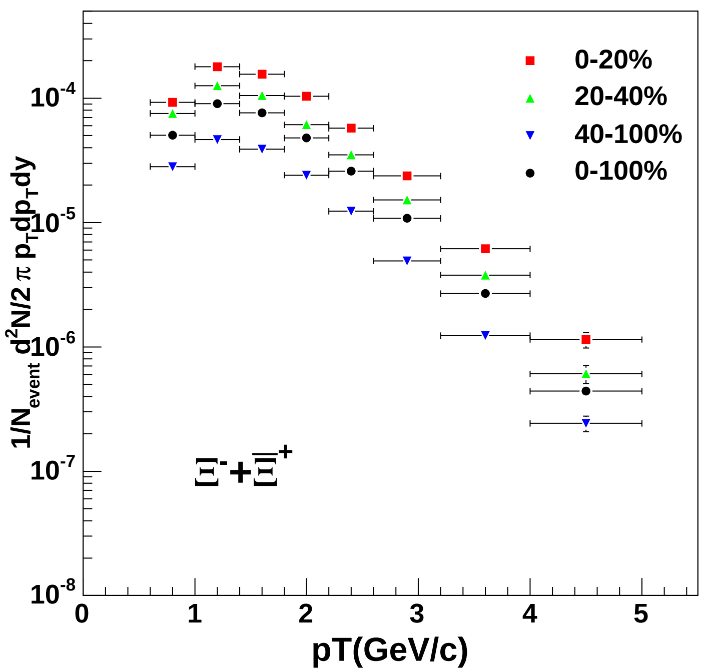

Figure 3.14: The raw spectra of Ξ^-+$\overline{\Xi}^+$ in three centrality bins and minimum bias data. The p_T covers 0.6-5.0 GeV/c and the rapidity $|y| < 1$.

From the raw spectra of K_S^0, Λ+$\overline{\Lambda}$(Fig. 3.10) and Ξ^-+$\overline{\Xi}^+$, we see that the raw yield of K_S^0 reaches its maximum in the p_T bin of 0.4-0.6 GeV/c, Λ+$\overline{\Lambda}$ in 0.8-1.0 GeV/c and Ξ^-+$\overline{\Xi}^+$ in 1.0-1.4 GeV/c. This observation may not lead to any conclusion as the raw yield depends on the cuts. However, considering the same cuts were used for each p_T bin at $p_T < 2.0$ GeV/c, it appears that the p_T region for the largest raw yield of a particle measured in the TPC is proportional to the particle mass. This provides a hint of which p_T region should be looked for in the first priority when searching for a new particle. This naive claim is also supported by the ϕ meson measurement(see [Yam01]).

3.12 Efficiency Corrections

The raw yield only takes a fraction of the total yield for a particle created in collisions. The total yield can not be measured directly due to various factors: the detector acceptance, response, tracking efficiency, reconstruction efficiency and vertex finding efficiency. For example, particles with larger rapidity($|y| > 2$) are not detected by the STAR TPC and some tracks may not well reconstructed if some hits are missing. It is the total yield not the raw yield which has the main physics content, being directly related to the collision dynamics. Therefore, to compare the physics results among different collision systems, the raw yield needs to be corrected.

Simulation programs were used to correct the raw yields [Lon02, Yam01]. Simulated V0 or $\Xi(\overline{\Xi})$ particles were embedded into real data and were forced to decay by GEANT 100% according to the desired decay channels. For d+Au simulations, one Monte-Carlo(MC) particle was embedded into each event and these particles have a flat rapidity distribution and an m_t distribution with an inverse slope of 350 MeV. Different numbers of events are used in three p_T regions to ensure sufficient MC particles for analysis at high p_T.

The combination of real and simulated MC data were then passed though the reconstruction chain. After that the reconstructed tracks and vertices associated with the MC tracks and vertices were generated. For each p_t and rapidity bin, the efficiency is defined as the number of reconstructed vertices(particles) divided by the number of input MC vertices(particles) in this bin. The final efficiency should also include the branching ratio that is not put into the simulation procedure. The event and track selection criteria and the topology cuts used on the efficiency estimates must be the same as those used on the raw yield calculations. Although the simulation program was designed to mimic the real detection environments, some information were still missing. For example, there is no dE/dx information for MC tracks and the DCA distributions for MC tracks and real tracks may be different due to the distortion or charge space effects in the detector. These factors are considered to be systematic uncertainties of the corrected spectra and will be discussed in the next chapter.

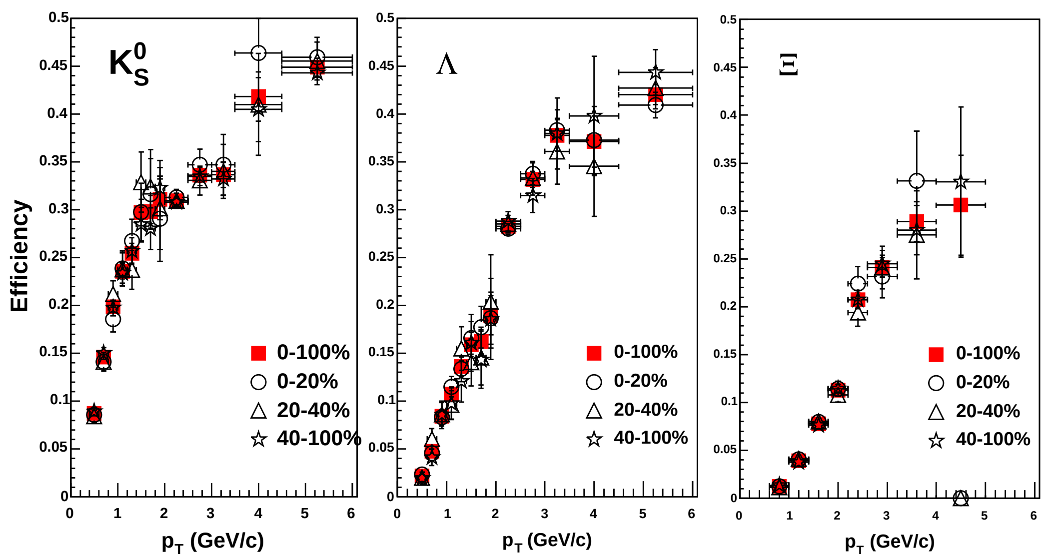

Figure 3.15: The correction factors for K_S^0, Λ and Ξ^- based on the topology cuts listed in Table 3.6 and 3.8. The discontinuities in the efficiency at $p_T = 3.5$ for K_S^0, $p_T = 2.0$ for Λ and $p_T = 2.2$ for Ξ^- reflect changes of cuts (see Table 3.6 and 3.8). The errors are statistical only.

Figure 3.15 shows the correction factor for K_S^0, Λ and Ξ^- as a function of transverse momentum (p_t) in $|y| < 1.0$ for three centrality intervals and minimum bias events. The correction factors shown here include the detector acceptance, tracking and reconstruction efficiencies as well as decay branching ratios. For d+Au collisions the values for the efficiency corrections are little dependent on centralities. This is quite different from Au+Au collisions where the efficiencies drop from peripheral collisions to more central collisions. This difference arises from the fact that the multiplicity difference for various centralities in d+Au collision is much smaller than that in Au+Au collisions. The $\overline{\Lambda}$ efficiency is close to Λ's except the lowest p_T bin where the $\overline{\Lambda}$ efficiency is low by 5%. This can be explained by the anti-proton absorption at low p_T. Due to the limited statistics for the embedded data, we use the minimum bias efficiencies to calculate the corrected spectra since the centrality difference and the anti-proton absorption effect are negligible compared to the statistical errors.

A vertex efficiency correction is necessary since the primary vertex may not be reconstructed successfully for low multiplicity events. From the study on embedded HIJING events, the vertex efficiency increases quickly with increasing multiplicity in a event and over 80% of the events missing vertex have fewer than three tracks in the TPC [Ada04]. These vertex missing events discarded in our analysis should be counted as the minimum bias events since they contribute to the total hadronic cross section. However, they have little chance to produce particles like K_S^0 and $\Lambda(\overline{\Lambda})$ that require at least two global tracks, and even less chance for $\Xi^-(\overline{\Xi}^+)$. Thus we only correct the number of events(see Table 3.3) that is a normalization factor in the spectra, but not the yields of the measured particles for these events missing a vertex. The overall vertex efficiency is 0.88 for the most peripheral bin(40-100%), 0.93 for minimum bias events and 1 for the central and middle centrality bins(0-20% and 20-40%).

CHAPTER 4

Systematic Uncertainties

The errors for the raw spectra and the efficiency calculation shown in the previous chapter are statistical errors which only depend on the statistics of analyzed data set. In the measurement of a particle yield, the statistical error is simply proportional to $\sqrt{N}$ where N is the particle number measured.

Systematic uncertainties, another more complicated error in the analysis, arise from various sources: time-varying experimental running status, detector responses that cannot be corrected by simulations or mismatch between the real and simulation environments, analysis methods and cuts used, etc. It is not realistic to analyze all possible systematic uncertainties as some of them are unknown to us.

In this chapter we only present the estimates of systematic uncertainties from some of sources. The overall systematic uncertainty, however, is not obtained simply by adding these uncertainties up because of their possible correlations, but by randomly changing several cut parameters (most are topology cut parameters). Only minimum bias events are used for this analysis as we assume a weak dependence on centrality for the systematic uncertainties.

4.1 FF and RFF Data Sets

To check for the possible systematic deviations from the detector configurations, the d+Au experiment was designed to be run in two opposite magnetic field directions with a magnitude of 0.5 $Tesla$ at STAR. These two data sets are labelled as FullField(FF) and Reversed FullField(RFF) data sets. Table 4.1 shows the relative uncertainties from FF and RFF data sets from raw yield calculations. The Monte-Carlo simulation results are assumed to be identical. Overall, this p_T bin-by-bin uncertainty ranges from 0 to 8% for the measured three types of particles. Some unexpected large numbers probably come from the limited statistics.

4.2 dE/dx cuts in raw yields

Not all the effects can be corrected via the Monte-Carlo(MC) simulation. MC tracks in embedded data do not carry dE/dx information as they are identified definitely by GeantID(a number labelling a MC particle). For the real data raw yields change with the dE/dx $n\sigma$ cuts. Ideally, when real tracks are selected within $|n\sigma| < 3$, the raw yield would not be cut away. However, due to the dE/dx calibration deviation the raw yield would not be saturated even using a looser $n\sigma$ cut. We compared the raw yields of K_S^0 and $\Lambda + \overline{\Lambda}$ with selecting daughter tracks $|n\sigma| < 3$ and $|n\sigma| < 4$. Most relative errors from these two selection criteria are less than 1% as shown in Table 4.1. This tells us that the track dE/dx measurement was well calibrated for this d+Au production. For example, Figure 4.1 shows the dE/dx bands of protons and pions in Λ candidates with the daughter track cuts of $|n\sigma| < 3$ and $|n\sigma| < 4$. The Λ candidates are selected in the invariant mass window within 1.108-1.122 GeV/c^2. The lines centered in the

p_T (GeV/c)	Ks FF-RFF	Λ FF-RFF	Ks dE/dx	Λ dE/dx
0.4 - 0.6	4.2%	-1.1%	0.6%	0.4%
0.6 - 0.8	2.6%	0.9%	0.6%	0.9%
0.8 - 1.0	2.3%	2.2%	0.8%	0.8%
1.0 - 1.2	1.6%	1.9%	0.8%	0.7%
1.2 - 1.4	2.1%	3.5%	0.5%	0.5%
1.4 - 1.6	3.1%	3.3%	0.5%	0.5%
1.6 - 1.8	1.9%	6.7%	0.4%	-0.2%
1.8 - 2.0	2.6%	3.8%	0.4%	0.8%
2.0 - 2.5	2.7%	-0.1%	0.6%	0.6%
2.5 - 3.0	2.7%	1.5%	0.4%	0.8%
3.0 - 3.5	0.8%	-1.7%	-0.1%	0.4%
3.5 - 4.5	3.3%	6.7%	0.02%	0.02%
4.5 - 6.0	-3%	4.2%	-2.2%	1.2%
p_T (GeV/c)	Ξ FF-RFF			
0.6 - 1.0	7.7%			
1.0 - 1.4	-5.3%			
1.4 - 1.8	-0.13%			
1.8 - 2.2	1.8%			
2.2 - 2.6	-4.8%			
2.6 - 3.2	-6.8%			
3.2 - 4.0	-2.6%			
4.0 - 5.0	19.2%			

Table 4.1: The relative systematic errors from two magnetic field settings, FullField(FF) and Reversed FullField(RFF) and the different dE/dx cuts. The FF-RFF means the difference of the raw yields between the FF data set and the RFF data set. The dE/dx errors are the difference of the raw yields between two daughter track $n\sigma$ cut sets, one $|n\sigma| < 3$ and another $|n\sigma| < 4$.

bands represent tracks with $|n\sigma| < 0.2$.

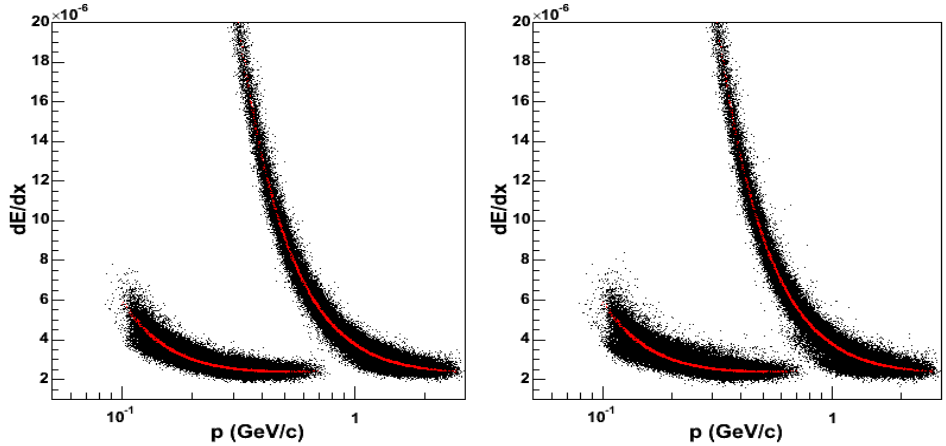

Figure 4.1: The dE/dx bands of protons and pions in Λ candidates. The left panel shows the proton and pion bands with $|n\sigma| < 3$. The right panel shows the proton and pion bands with $|n\sigma| < 4$. The lines centered in the bands correspond to a $|n\sigma| < 0.2$ cut. The p_T range for Λ candidates is $0.4 - 2.0$ GeV/c.

4.3 Vertex-Z Effect

The positions of primary vertices in d+Au collisions can spread over a very wide area along the beam direction(Z axis) from -100 cm to +100 cm around the center of the TPC 3.1. The minimum bias triggering requires a vertex-z cut $|VertexZ| < 50$cm. Since the anode sectors recording the ionized tracks are 210 cm away from the center of the TPC, the particle production would not depend on the vertex-z cut in an ideal condition. However, as shown in Table 4.2, the measurements on real events show an apparent increase in raw yields as the vertex-z cut becomes tighter from $|VertexZ| < 50$ cm to $|VertexZ| < 25$ cm. This indicates that the particles produced away from the center of the TPC are easier to be 'absorbed', which is most likely caused by the interference of the supporting materials close to the edges of SVT right outside the beam line. The efficiency calculations for K_S^0 and Λ from various p_T bins do not show a consistent increase when the VertexZ cut becomes tighter. For the Ξ efficiency, the difference between these two sets of VertexZ cuts is much smaller than that for the real events. Therefore, the efficiency corrections can not cancel the vertex-z effect that appears in the raw yield calculations. This difference indicates our simulation procedure does not take the detector geometry issue into account with sufficient accuracy.

p_T (GeV/c)	K_S^0(raw yield)	K_S^0(efficiency)	Λ(raw yield)	Λ(efficiency)
0.4 - 0.6	-10.4%	0.6%	-7.5%	23.7%
0.6 - 0.8	-8.9%	0.05%	-9.6%	4.7%
0.8 - 1.0	-7.7%	-1.4%	-7.9%	-4.0%
1.0 - 1.2	-7.1%	1.3%	-7.0%	-1.3%
1.2 - 1.4	-5.8%	-2.2%	-5.6%	-1.6%
1.4 - 1.6	-5.4%	-0.1%	-6.8%	-8.2%
1.6 - 1.8	-5.7%	-4.7%	-3.7%	-21.7%
1.8 - 2.0	-4.4%	-8.2%	-4.0%	1.6%
2.0 - 2.5	-6.2%	-3.0%	-5.8%	-2.3%
2.5 - 3.0	-5.9%	-2.6%	-4.0%	-0.6%
3.0 - 3.5	-6.8%	0.4%	-3.6%	-2.2%
3.5 - 4.5	-6.9%	0.05%	-2.1%	-0.6%
4.5 - 6.0	-5.5%	-2.3%	-20.9%	-2.3%
p_T (GeV/c)	Ξ^-(raw yield)	Ξ^-(efficiency)		
0.6 - 1.0	-32.0%	-1.6%		
1.0 - 1.4	-16.9%	-3.6%		
1.4 - 1.8	-12.1%	-2.3%		
1.8 - 2.2	-8.9%	-3.2%		
2.2 - 2.6	-10.3%	-3.4%		
2.6 - 3.2	-5.6%	-3.1%		
3.2 - 4.0	-12.1%	-7.4%		
4.0 - 5.0	-6.3%	-1.0%		

Table 4.2: The relative systematic errors from the vertex-z cuts for K_S^0, Λ and Ξ. The percentages are obtained by using the raw yields and efficiency calculations with the cut $|VertexZ| < 50$cm minus those with the cut $|VertexZ| < 25$cm.

4.4 Rapidity and Nhits

Due to the asymmetry in d+Au collisions, the corrected yield of a particle shows a significant difference between the gold side and the deuteron side at the large rapidity region [Sim05]. However, this asymmetry would not greatly affect the strange hadron at mid-rapidity region around $y = 0$. We compared the raw and corrected yields with two different rapidity cuts of $|y| < 0.5$ and $|y| < 1.0$ (Table 4.3) for K^0_S, Λ and Ξ. Within the error bars the corrected yields show no obvious differences between the two sets of the cuts although the raw yields do increase over all p_T bins for three measured particles with the smaller rapidity region chosen. Some unexpected large differences in the corrected yields arise from the limited statistics of real or embedded events.

Another factor that may affect the yields is the number of hits (nhits) for a track that describes the track quality. If nhits is larger than 15, we believe that track has a good quality. We have checked the K^0_S yields with two sets of cuts for nhits on pion tracks, nhits$>$ 15 and nhits$>$ 30. As expected, Table 4.4 shows that the corrected yields do not have an obvious change while there is a considerable drop in the raw yields from nhits$>$ 15 to nhits$>$ 30.

4.5 Topology Cuts on Real and MC Data

The topology cuts are the most efficient cuts in reconstructing weak decay particles. The signal to background ratio(S/B) easily becomes large with tight topology cuts. Since the Monte-Carlo simulation tries to completely describe the detector response, each cut parameter distribution from real particles should have the same shape as that from MC particles if identical topology cuts are applied. Otherwise, the mismatch between them would cause the wrong efficiency calculation.

p_T (GeV/c)	K_S^0(raw yield)	K_S^0(corr. yield)	Λ(raw yield)	Λ(corr. yield)
0.4 - 0.6	-35.8%	-1.6%	-82.4%	1.6%
0.6 - 0.8	-30.8%	-1.3%	-65.2%	3.0%
0.8 - 1.0	-25.0%	0.6%	-45.4%	3.5%
1.0 - 1.2	-19.8%	-2.1%	-34.3%	0.6%
1.2 - 1.4	-18.0%	0.9%	-27.1%	-0.8%
1.4 - 1.6	-17.4%	-1.1%	-22.7%	-7.6%
1.6 - 1.8	-15.8%	1.5%	-19.8%	-7.1%
1.8 - 2.0	-13.7%	-9.8%	-21.8%	-16.1%
2.0 - 2.5	-11.3%	-4.9%	-13.2%	-5.8%
2.5 - 3.0	-10.9%	-6.2%	-9.9%	-2.4%
3.0 - 3.5	-10.7%	-9.2%	-5.4%	-2.7%
3.5 - 4.5	-1.6%	1.4%	-9.8%	-15.9%
4.5 - 6.0	-9.3%	-6.1%	-22.9%	-22.6%
p_T (GeV/c)	Ξ(raw yield)	Ξ(corr. yield)		
0.6 - 1.0	-75.1%	-4.2%		
1.0 - 1.4	-52.1%	-1.4%		
1.4 - 1.8	-34.5%	0.9%		
1.8 - 2.2	-33.4%	-3.2%		
2.2 - 2.6	-26.8%	-10.2%		
2.6 - 3.2	-28.3%	-12.3%		
3.2 - 4.0	-25.2%	-11.6%		
4.0 - 5.0	-31.3%	-11.6%		

Table 4.3: The relative difference of the raw and corrected yield from two rapidity cuts, $|y| < 0.5$ and $|y| < 1.0$. The percentage numbers mean the $|y| < 1.0$ yields minus the $|y| < 0.5$ yields then divided by the $|y| < 1.0$ yields.

p_T (GeV/c)	K_S^0(raw yield)	K_S^0(efficiency)	K_S^0(corr. yield)
0.4 - 0.6	38.98%	38.99%	-0.01%
0.6 - 0.8	33.75%	29.91%	5.48%
0.8 - 1.0	31.88%	27.82%	5.62%
1.0 - 1.2	30.31%	30.5%	-0.28%
1.2 - 1.4	29.51%	27.98%	2.12%
1.4 - 1.6	28.8%	23.78%	6.58%
1.6 - 1.8	25.15%	20.94%	5.32%
1.8 - 2.0	22.3%	23.24%	-1.22%
2.0 - 2.5	20.59%	20.61%	-0.02%
2.5 - 3.0	18.24%	20.24%	-2.5%
3.0 - 3.5	16.43%	19.7%	-4.06%
3.5 - 4.5	15.52%	15.42%	0.12%
4.5 - 6.0	11.36%	15.33%	-4.69%

Table 4.4: The relative difference of the raw yield, efficiency and the corrected yield with two sets of number of hits(nhits) cuts for K_S^0, nhits$>$ 15 and nhits$>$ 30.

For the real reconstructed particles, the background-subtracted distribution can be obtained by subtracting the distribution outside the signal mass window from the distribution within the signal mass window. The number of selected entries outside the signal mass window should be close to that within the signal mass window underneath the background fit line. This method assumes the topology cut parameter distributions for the background from the different invariant mass regions are the same. Figure 4.2 shows the background-subtracted topology parameter distributions for real and MC reconstructed K_S^0. The distributions are normalized to the number of K_S^0 candidates. Most distributions for real and MC are matched except DCA of K_S^0 to primary vertex(dca-K_S^0-PV). The feed-down contribution from other particles to K_S^0 is negligible, so this mismatch is most likely from some uncertainties in the measurement. Our study has shown that this mismatch becomes smaller when the primary vertex position of a MC event is smeared in a small amount. This indicates the position of the primary vertex may not be well determined in d+Au collisions due to the low multiplicity and the largest uncertainty is in Z direction. For the final spectra, we use 1.5 cm as the dca-K_S^0-PV cut thus the mismatch effect was reduced to the minimum and could be ignored. Λ topology cut parameter distributions (Figure 4.3) have the same situation. Unlike the K_S^0, the apparent mismatch of the dca-Λ-PV distributions between real and MC data comes from both the feed-down contribution from Ξ and the possible uncertainty in primary vertex determination. The dca-Λ-PV cut of 5 cm for the final spectra was sufficient. For the Ξ topology cut parameter distributions (Figure 4.4), we use the 2 dimensional decay length and dca-Ξ-PV in the X-Y plane to avoid the impact from the largest uncertainty in Z direction. We use 1 cm as the 2D dca-Ξ-PV cut.

The systematic errors for the minimum bias spectra calculated from the corrected spectra with various topology cuts are listed in Table 4.5. These errors dominate the overall systematic uncertainties in our analysis for the d+Au system.

p_T (GeV/c)	K_S^0	$\Lambda+\overline{\Lambda}$	p_T (GeV/c)	$\Xi^-+\overline{\Xi}^+$
0.4 - 0.6	7%	20%	0.6 - 1.0	9%
0.6 - 0.8	9%	14%	1.0 - 1.4	10%
0.8 - 1.0	8%	5%	1.4 - 1.8	6%
1.0 - 1.2	8%	7%	1.8 - 2.2	5%
1.2 - 1.4	13%	9%	2.2 - 2.6	5%
1.4 - 1.6	7%	8%	2.6 - 3.2	5%
1.6 - 1.8	11%	6%	3.2 - 4.0	5%
1.8 - 2.0	11%	8%	4.0 - 5.0	8%
2.0 - 2.5	9%	5%		
2.5 - 3.0	6%	7%		
3.0 - 3.5	6%	8%		
3.5 - 4.5	10%	10%		
4.5 - 6.0	13%	9%		

Table 4.5: The systematic errors from topology cuts for the minimum bias spectra of K_S^0, $\Lambda+\overline{\Lambda}$ and $\Xi^-+\overline{\Xi}^+$. These errors are calculated according to the spectra in various topology cuts.

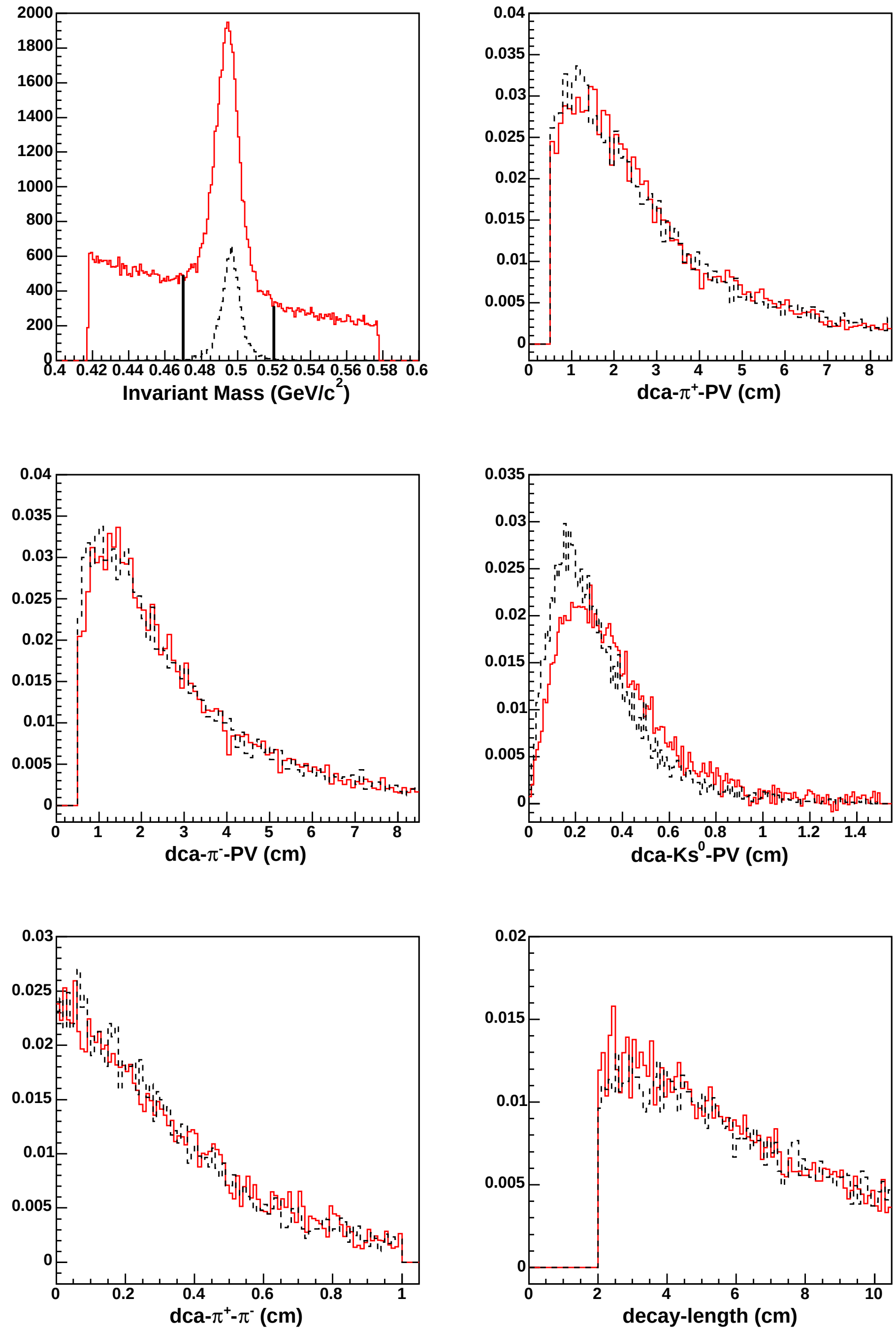

Figure 4.2: Topology cut parameter distributions for K^0_S Real(solid lines) and MC(dashed lines) data. The upper left plot is the invariant mass distribution for real and MC data. Two vertical lines confine the K^0_S signal region.

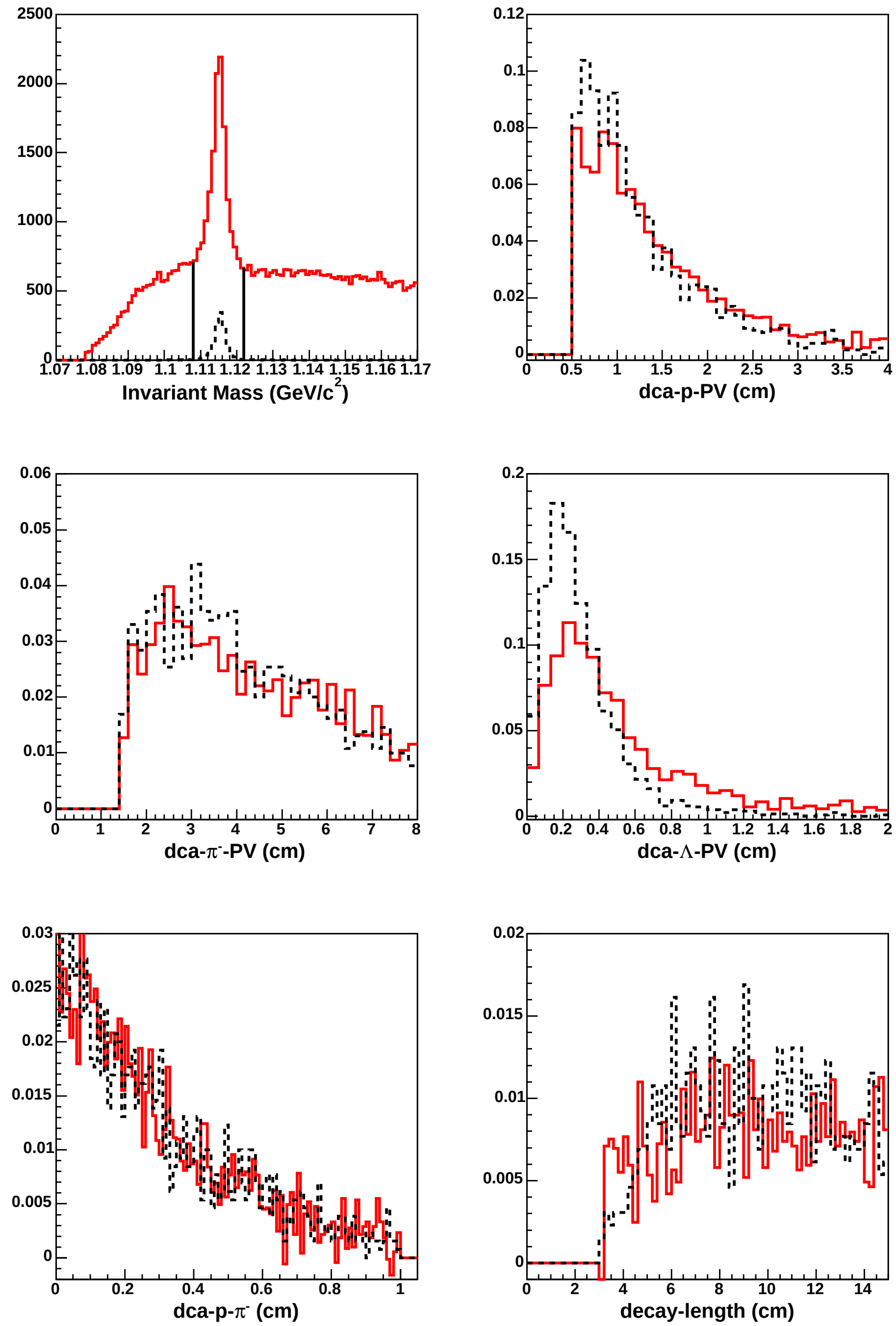

Figure 4.3: Topology cut parameter distributions for Λ Real(solid lines) and MC(dashed lines) data. The upper left plot is the invariant mass distribution for real and MC data. Two vertical lines confine the Λ signal region.

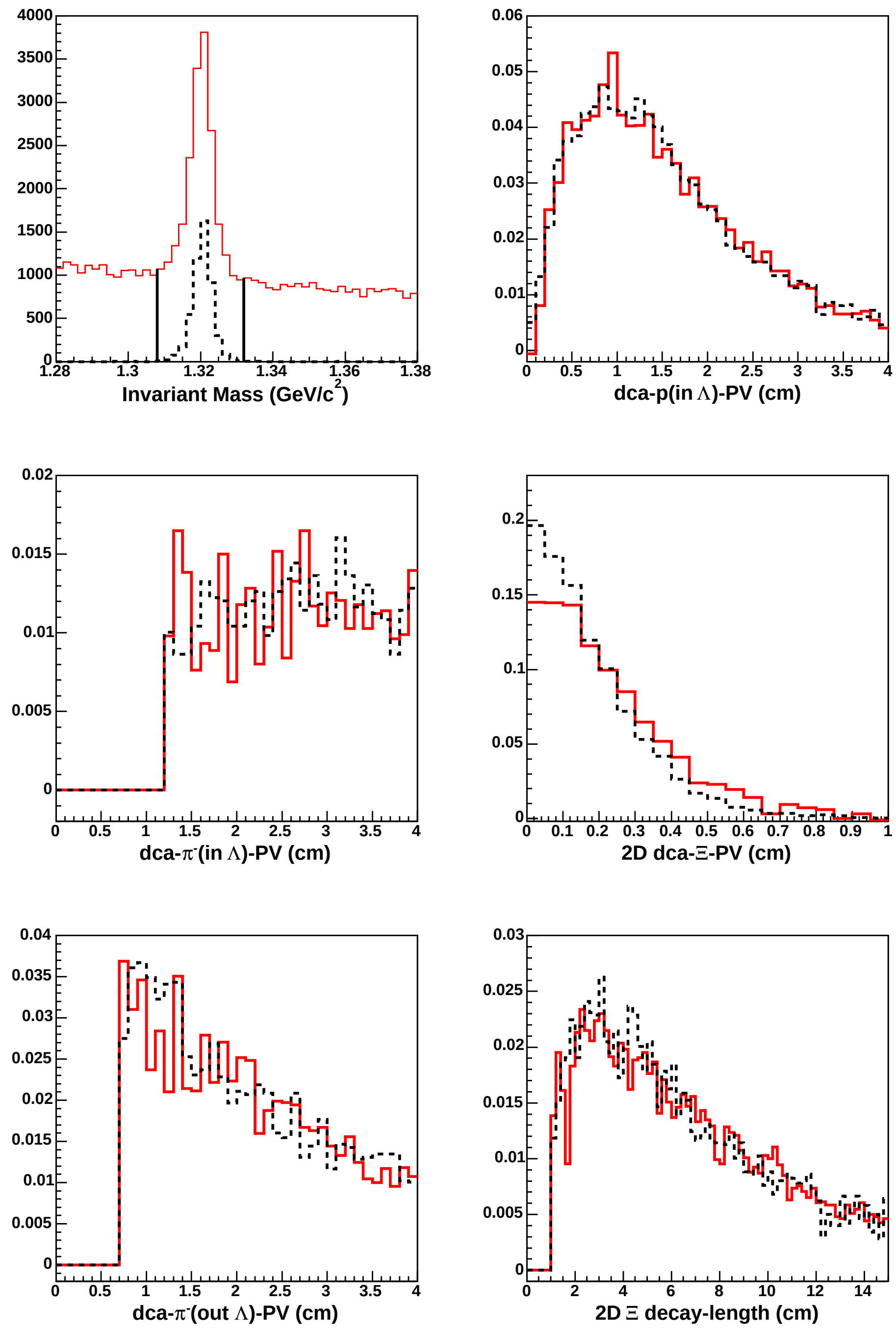

Figure 4.4: Topology cut parameter distributions for Ξ Real(solid lines) and MC(dashed lines) data. The upper left plot is the invariant mass distribution for real and MC data. Two vertical lines confine the Ξ signal region. 2 dimensional decay length and dca of Ξ-PV in X-Y plane are used for Ξ analysis.

4.6 Background Fit and Double Counted Signals

There are other uncertainties.

Background Fit: There are two methods to fit the background in invariant mass plots. One is to fit the signal and background together with a Gaussian function plus a 2nd order polynomial function and then subtract the polynomial function from the histogram. Another one is to fit the pre-defined background outside the signal region with a 2nd order polynomial function and then subtract this function value from the bin counts in the signal region. It turns out the overall difference between these two methods is less than 3% [Lon02].

Double Counted Signals: Sometimes one track in the reconstruction will be used twice due to track splitting. This will lead to artificially larger yields. An early study showed that the difference of double counted signals between the real data and Monte-Carlo embedded data is dependent on the multiplicity of the events, but not on p_T. In the most peripheral centrality from Au+Au collision, this difference was very small [Lon02]. In d+Au collisions with even smaller multiplicity the MC simulation would better reflect the real condition and the effect from double counted signals is negligible.

4.7 Weak Decay Feed-Down Contributions to $\Lambda(\overline{\Lambda})$

Not all the Λs are produced at the primary vertex for the d+Au collisions and a portion of them come from Ξ^-, Ξ^0 and Ω weak decays via

$$\Xi^- \rightarrow \pi^- + \Lambda \tag{4.1}$$

$$\Xi^0 \to \pi^0 + \Lambda \tag{4.2}$$

$$\Omega^- \to K^- + \Lambda \tag{4.3}$$

We can estimate the feed-down contribution from Ξ decays by applying different DCA of Λ-PV cuts([Lon02]) because Λs from Ξ decays have a wider DCA-Λ-PV distribution than those from the primary vertex (Figure 4.3) due to the Ξ decay boost. However, this method fails if the wider DCA-Λ-PV distribution partially arises from some other uncertainties as discussed in section 4.5. Since a corrected Ξ integrated yield(dN/dy) is available from our measurements, we can use an alternative method by reconstructing Λs from the Ξ embedded events and then calculating feed-down according to the Ξ dN/dy. The Monte-Carlo Ξs are forced to decay to Λs in the simulation procedure according to equation 4.1. We use the exact same topology cuts and selection criteria on these Λs as the inclusive Λs (Table 3.4 and 3.6). The raw Λ counts in ith p_T bin in a specific centrality interval from the Ξ^- feed-down is

$$\Lambda_{\Xi}^{i} = (dN/dy)_{\Xi} \frac{N_{\Lambda}^{i}}{N_{\Xi}} \tag{4.4}$$

where $(dN/dy)_{\Xi}$ is the Ξ integrated yield in a unit rapidity, N_{Λ}^{i} the counts of Λ in ith p_T bin and N_{Ξ} the total counts of input Ξs over the whole p_T range(0-5.0 GeV/c) in the same rapidity, centrality and vertex-z region as for the reconstructed Λs. This method applies only if Monte-Carlo input Ξ has the same p_T or m_T distribution as Ξ's from the real events. The inverse slope, T_1, of Ξ m_T distribution is $356 \pm 8(stat) \pm 21(syst)$ MeV (Table 5.1) from the real data measurement and it was set as 350 MeV in MC events. The $(dN/dy)_{\Xi}$ is given by integrating the Ξ spectrum over the whole p_T range. The numbers are listed in Table 5.1 for all the centralities.

The feed-down contribution from Ξ^0 decay is believed to be the same as from Ξ^- decay since their yields are close. The Ω^- dN/dy is about 15% of Ξ^-'s in Au+Au collisions at the same beam energy. But considering that the Ω has a harder m_T spectrum(larger temperature or inverse slope) and smaller decay length, we assume that the Ω^- feed-down contribution is 10% of that for the Ξ^-'s. The feed-down to $\overline{\Lambda}$ from anti-multi-strange hyperons is approximately same as the feed-down to Λ from multi-strange hyperons since both hyperons have similar inverse slopes in their m_T distributions. Figure 4.5 shows the raw Λ+$\overline{\Lambda}$ spectra normalized to the number of events from all the weak decay feed-down contributions from Ξ^-, Ξ^0 and Ω^- and their antiparticles.

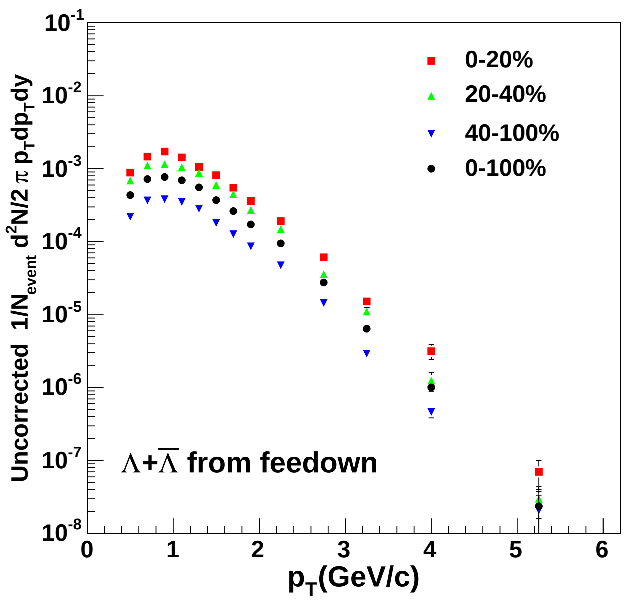

Figure 4.5: Raw Λ+$\overline{\Lambda}$ spectra from the feed-down contributions from Ξ^-, Ξ^0, Ω^- and their anti-particles. The data points of the last p_T bin are extrapolated. The errors are statistical only.

According to Equation 4.4 and the raw inclusive Λ yield(Figure 3.10), the corrected Λ counts in ith p_T bin in a specific centrality interval from the Ξ^- feed-down is

$$\Lambda^i = \frac{\Lambda'^i_{inclusive} - \Lambda'^i_{\Xi}}{\eta_\Lambda} \tag{4.5}$$

where $\Lambda'^i_{inclusive}$ and Λ'^i_{Ξ} are the inclusive and feed-down Λ raw counts in ith p_T bin, respectively, and η_Λ is the efficiency for Λ (see Figure 3.15). The Λ+$\overline{\Lambda}$ p_T and m_T spectra after feed-down correction are plotted in Figures 5.1 and 5.2 and the corresponding integrated yields are listed in Table 5.1.

This is impossible to estimate the feed-down contribution from resonance particles that decay at the primary vertex using the topology cuts. So our feed-down correction only excludes the Λs from multi-strange(anti-multi-strange) hyperons weak decay.

CHAPTER 5

Results

In this chapter, we present the main results for the analyses of the production of the strange hadrons, K_S^0, Λ and Ξ in d+Au collisions at $\sqrt{s_{NN}}$ = 200 GeV. The corrected transverse mass(m_T) and momentum(p_T) spectra are given for the three centrality bins and for the minimum bias events. The ratios of $\overline{\Lambda}/\Lambda$ and K_S^0/Λ as a function of p_T will be shown. The integrated yield dN/dy and the mean p_T are derived from the spectra. The nuclear modification factor R_{CP} was obtained from the spectra for the most central collisions(0-20%) and the spectra for the most peripheral collisions(40-100%).

5.1 Corrected p_T and m_T Spectra and Fit Function

The corrected p_T spectra can be obtained using the raw normalized yield for each p_T bin shown in Chapter 3 divided by the efficiency value for the same p_T bin. The vertex finding efficiency was used to correct the number of events for each centrality interval. The corrected m_T spectra can be obtained simply by changing the scale p_T to m_T(see Eq. B.8). Figure 5.1 and Figure 5.2 show the corrected p_T and m_T spectra for K_S^0, $\Lambda+\overline{\Lambda}$ and $\Xi^-+\overline{\Xi}^+$ for three centralities and minimum bias events at mid-rapidity $|y| < 1$ in d+Au collisions at $\sqrt{s_{NN}} = 200$

GeV. $\Lambda + \overline{\Lambda}$ spectra were corrected by the feed-down contributions from multi-strange baryon(Ξ,Ξ^0 and Ω) week decay (see section 4.7). The measured p_T range covers 0.4-6.0 GeV/c for K_S^0 and $\Lambda + \overline{\Lambda}$ and 0.6-5.0 GeV/c for $\Xi^- + \overline{\Xi}^+$.

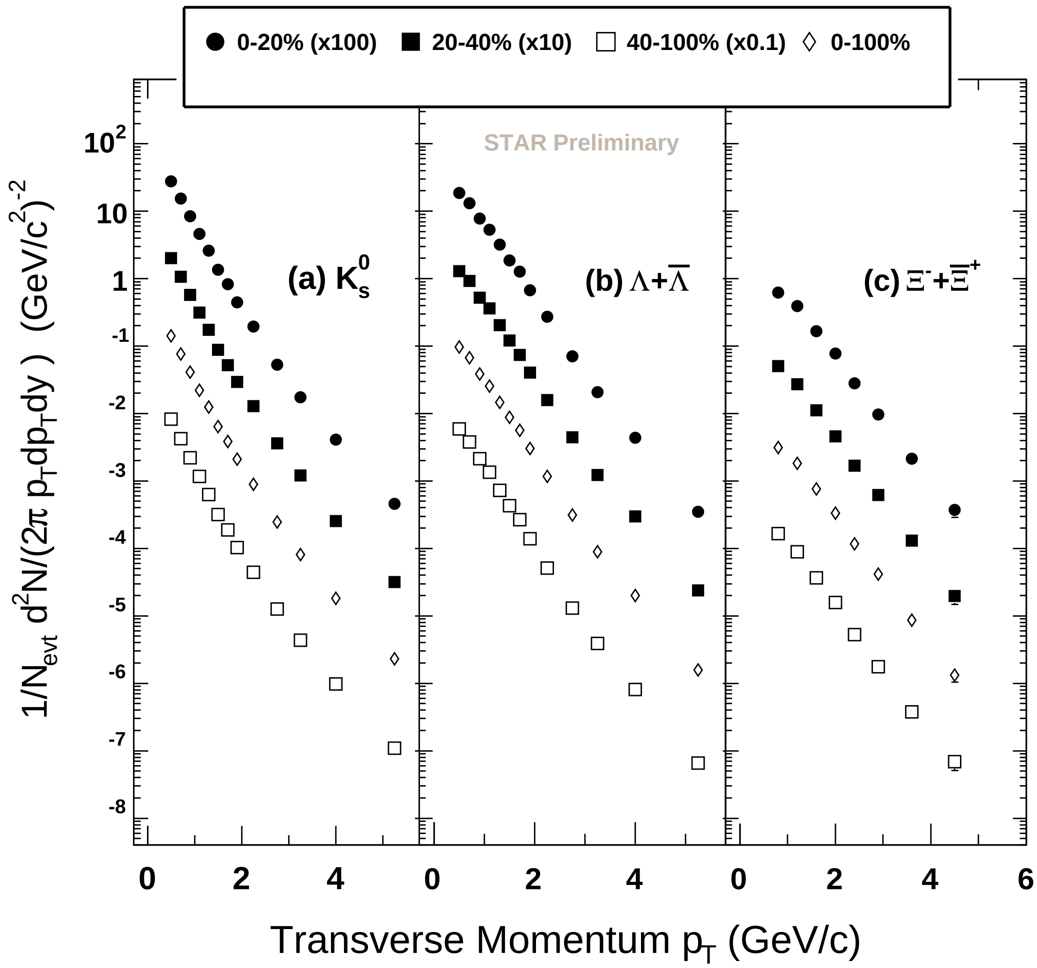

Figure 5.1: The corrected transverse momentum (p_T) spectra of K_S^0, $\Lambda + \overline{\Lambda}$ and $\Xi^- + \overline{\Xi}^+$ in three centrality intervals(0-20%, 20-40% and 40-100%) and minimum bias events. Data points were scaled for clear illustration. Error bars, most of which are smaller than its marker size, are statistical errors only.

We use double exponential function

$$\frac{dN}{2\pi dy}\left(\frac{a}{T_1(m_0+T_1)}e^{-\frac{(m_t-m_0)}{T_1}} + \frac{(1-a)}{T_2(m_0+T_2)}e^{-\frac{(m_t-m_0)}{T_2}}\right) \tag{5.1}$$

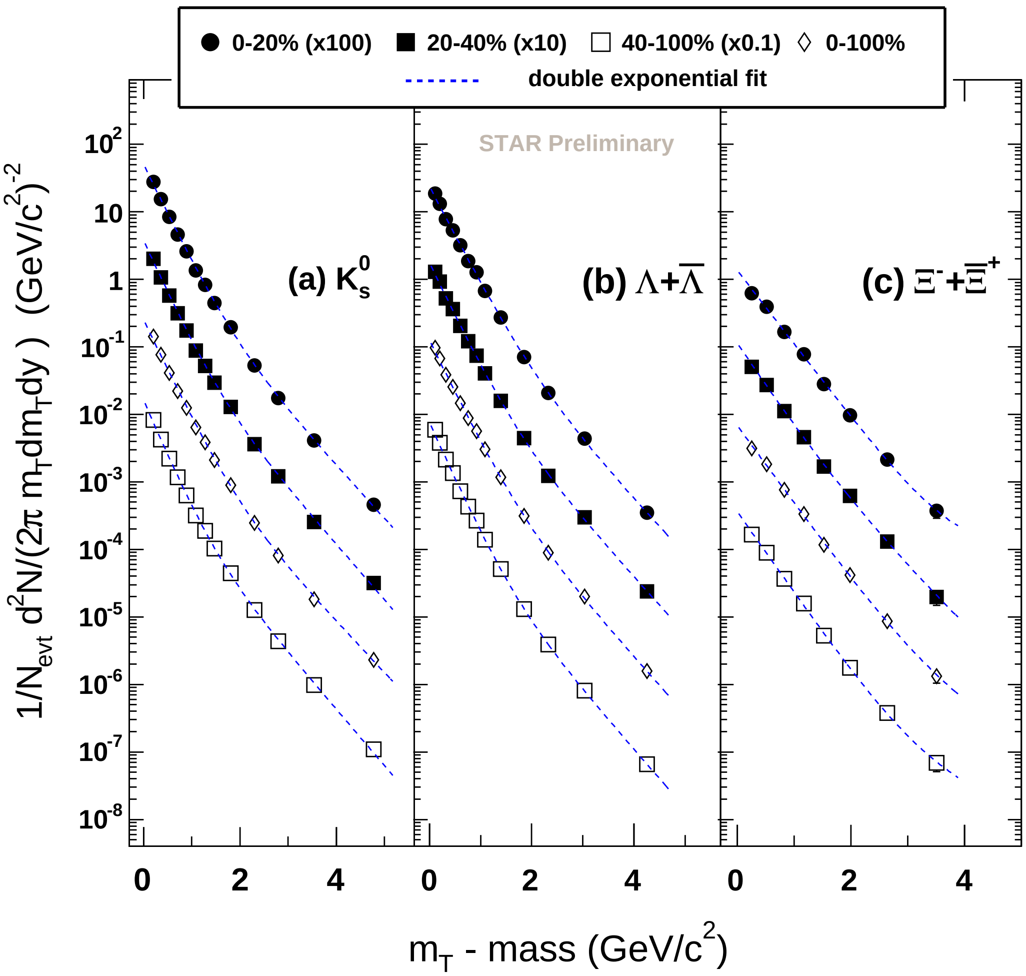

Figure 5.2: The corrected transverse mass($m_T - m_0$) spectra of K_S^0, $\Lambda+\overline{\Lambda}$ and $\Xi^-+\overline{\Xi}^+$ in three centrality intervals(0-20%, 20-40% and 40-100%) and minimum bias events. Data points were scaled for clear illustration. Error bars, most of which are smaller than its marker size, are statistical errors only.

to fit the m_t spectra where four fit parameters $dN/dy, a, T_1, T_2$ correspond to the integrated yield, the portion of the first exponential function, the inverse slope of the first and second exponential function, respectively. Physically, the double exponential function can be understood by two component models: soft(thermal) hadron contribution at the low m_t and hard hadron contribution at high m_t. The traditional single exponential function works well only for the low m_t region and the power law function only for the high m_t region.

5.2 The $\overline{\Lambda}/\Lambda$ Ratio

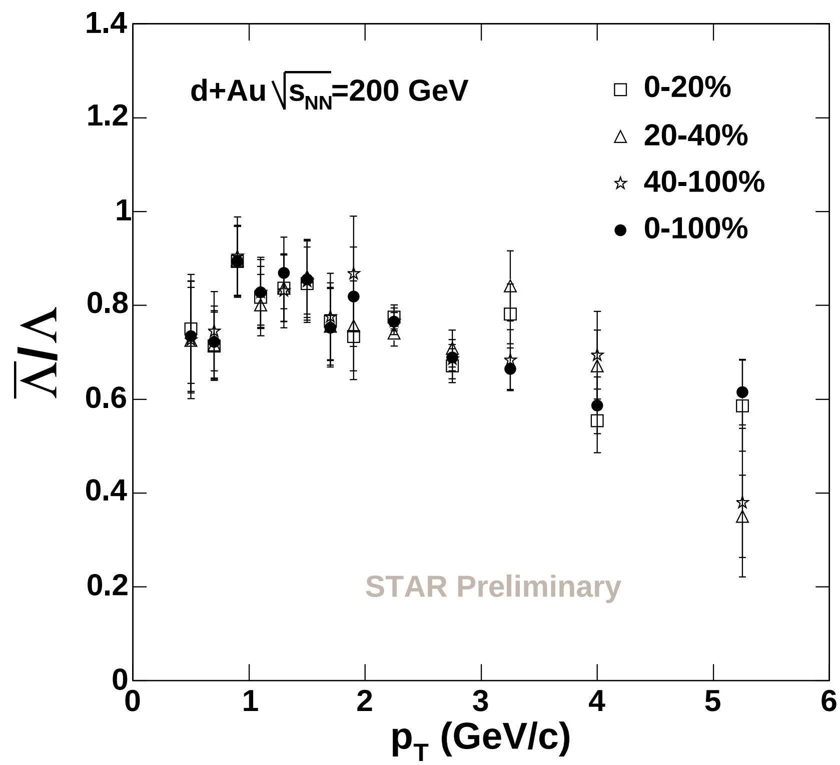

Figure 5.3: Ratio of the $\overline{\Lambda}/\Lambda$ as a function of p_T for three centralities and minimum bias events. Errors are statistical only.

The p_T dependent ratio of $\overline{\Lambda}/\Lambda$ was obtained according to the feed-down corrected Λ and $\overline{\Lambda}$ spectra measured separately. In Figure 5.3 we see that at $p_T < 2$ GeV/c the ratio is around 0.8 and it starts dropping when $p_T > 2$ GeV/c and reaches about 0.6 at high p_T. This trend is consistent with the $\bar{p}/p$ ratio for Au+Au collisions at RHIC [Adl04]. The overall ratio is $0.82 \pm 0.01(stat) \pm 0.03(syst)$.

5.3 The Λ/K_S^0 Ratio

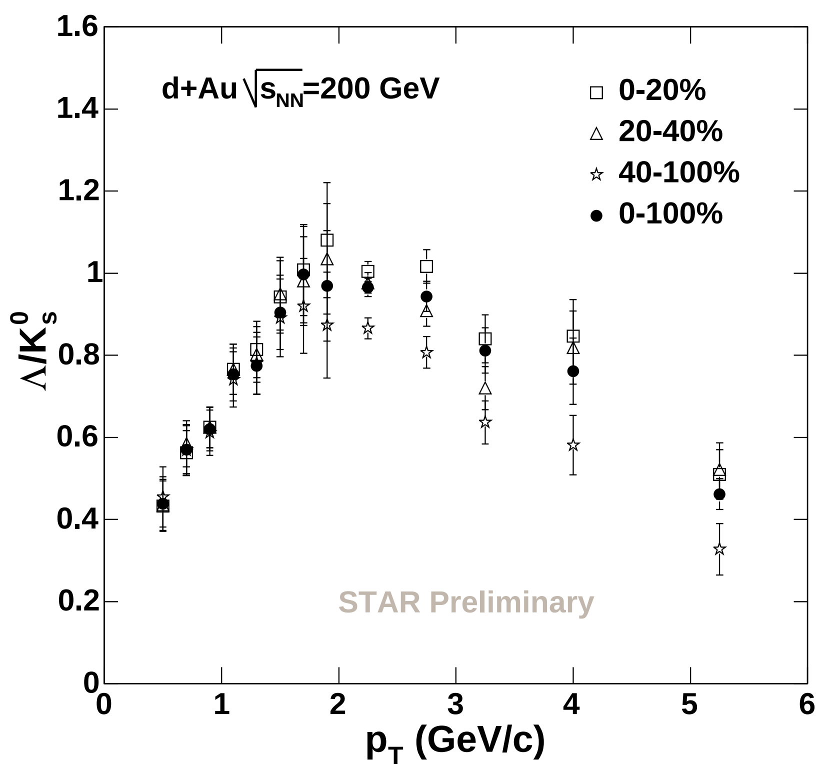

Figure 5.4: Ratio of Λ/K_S^0 as a function of p_t for three centralities and minimum bias events. Errors are statistical only.

The p_T dependent ratio of the Λ/K_S^0 was determined from the corrected K_S^0 and Λ p_t spectra (Figure 5.4). Here Λ refers to Λ only. The ratio is about ~ 0.4 at $p_T = 0.5$ GeV/c, and then increases with p_T reaching the maximum ~ 1.0 at $p_T = 2.0$ GeV/c. It then decreases in the higher p_T region. The ratios in d+Au collisions is not significantly dependent of centralities, which is quite different from the Au+Au results where the Λ/K_S^0 ratios differ by a factor of 2 between the peripheral and the central collisions. We will discuss it in next chapter.

5.4 dN/dy and $\langle p_T \rangle$

The integrated yields dN/dy are extracted from the double exponential fits on the m_t spectra as expressed in equation 5.1. dN/dy is one of the parameters in the fit function. Table 5.1 lists the dN/dy values for K_S^0, Λ+$\overline{\Lambda}$(after feedown correction) and Ξ^-+$\overline{\Xi}^+$ in three centralities and minimum bias events. The $\langle\ p_T\ \rangle$ listed in the same table was calculated numerically from the fit function(see Appendix C). T_1, another parameter in the fit function, is the inverse slope of the spectrum at low p_T regime and it depends on the particle mass. As shown in Table 5.1, the more central collision has the larger T_1.

Figure 5.5 shows the dN/dy normalized to the number of participated nucleus ($\langle N_{part}\rangle$) vs. $\langle N_{part}\rangle$ for K_S^0, Λ+$\overline{\Lambda}$ and Ξ^-+$\overline{\Xi}^+$. The $\langle N_{part}\rangle$ numbers used are listed in Table 3.2. For the comparison, the dN/dy from the Au+Au system calculated from the Boltzmann fit function are also presented [Lon05a, STA05]. The normalized dN/dy increases with $\langle N_{part}\rangle$ from d+Au to Au+Au system indicating the yield enhancement of the strange hadrons at collision energy 200 GeV at RHIC. However, there exists a jump of the yield from the most central d+Au collisions(0-20%) to the peripheral Au+Au collisions(60-80%) and this situation is most serious in the K_S^0 measurement. We have also observed in

K_S^0			
centrality	$dN/dy \pm (stat) \pm (syst)$	$\langle\ p_T\ \rangle \pm (stat)$ (GeV/c)	$T_1 \pm (stat)$ (MeV)
0-100% (minbias)	$0.381 \pm 0.008 \pm 0.05$	0.752 ± 0.0261	291 ± 6
0-20%	$0.779 \pm 0.01 \pm 0.09$	0.759 ± 0.0303	291 ± 7
20-40%	$0.547 \pm 0.01 \pm 0.06$	0.739 ± 0.0366	275 ± 7
40-100%	$0.218 \pm 0.005 \pm 0.03$	0.710 ± 0.0407	257 ± 7
$\Lambda+\overline{\Lambda}$	(after feed-down correction)		
0-100% (minbias)	$0.308 \pm 0.006 \pm 0.03$	0.905 ± 0.037	282 ± 6
0-20%	$0.625 \pm 0.01 \pm 0.06$	0.929 ± 0.049	294 ± 8
20-40%	$0.428 \pm 0.008 \pm 0.04$	0.896 ± 0.0548	270 ± 9
40-100%	$0.171 \pm 0.004 \pm 0.02$	0.851 ± 0.0666	250 ± 9
$\Xi^-+\overline{\Xi}^+$			
0-100% (minbias)	$0.024 \pm 0.0006 \pm 0.003$	1.082 ± 0.0387	356 ± 8
0-20%	$0.0509 \pm 0.002 \pm 0.005$	1.117 ± 0.0346	375 ± 8
20-40%	$0.0363 \pm 0.001 \pm 0.004$	1.069 ± 0.0428	346 ± 9
40-100%	$0.0121 \pm 0.0005 \pm 0.0016$	1.051 ± 0.0727	338 ± 10

Table 5.1: dN/dy, $\langle\ p_T\ \rangle$ and T_1 for K_S^0, $\Lambda+\overline{\Lambda}$ and $\Xi^-+\overline{\Xi}^+$ in three centralities and minimum bias events in d+Au 200 GeV. The systematical errors for $\langle\ p_T\ \rangle$ are 5% and T_1 6%.

d+Au collisions that the K_S^0 yield is lower than the charged kaon yield by about 70% in the p_T region $0.3 < p_T < 0.4$ GeV/c. We found this discrepancy to be independent of the collision centrality and is likely to be from an unknown detector systematics. In this thesis we will focus on the nuclear modification R_{CP} and $\langle p_T \rangle$, which are not affected by this systematic error.

Figure 5.6 shows the $\langle p_T \rangle$ of the K_S^0, $\Lambda+\overline{\Lambda}$ and $\Xi^-+\overline{\Xi}^+$ spectra as a function of $\langle N_{part} \rangle$ in d+Au and Au+Au collisions. The numbers for Au+Au collisions are calculated from the Boltzmann fit function. While the Λ $\langle p_T \rangle$ increases from 0.851 at d+Au peripheral collisions(40-100%) with $\langle N_{part} \rangle = 5.1$ to 1.05 at Au+Au most central collisions(0-5%) with $\langle N_{part} \rangle = 352.4$, the Ξ $\langle p_T \rangle$ shows no significant

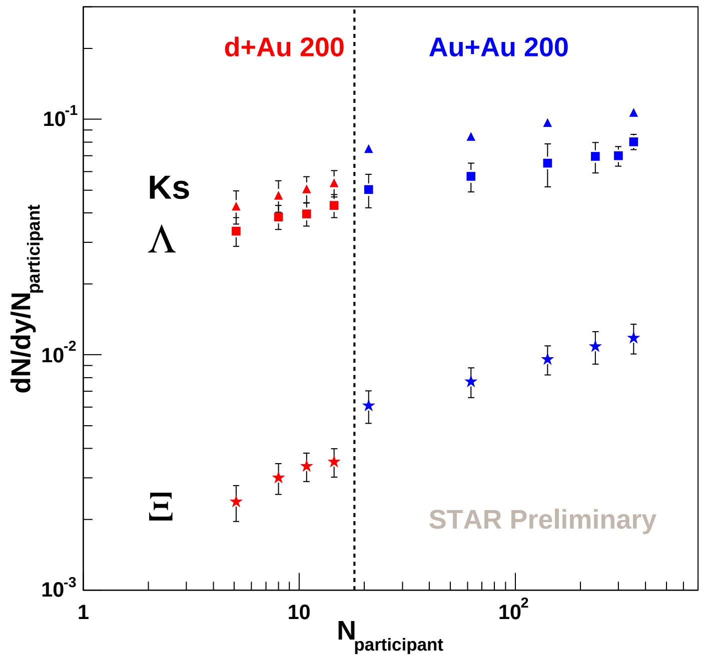

Figure 5.5: Normalized dN/dy vs. the number of participated nucleus $\langle N_{part} \rangle$ in d+Au(left of the dashed line) and Au+Au(right of the dashed line) 200 GeV for K_S^0, Λ+$\overline{\Lambda}$ and Ξ^-+$\overline{\Xi}^+$. Errors include statistical and systematical errors.

increase from d+Au to Au+Au system.

5.5 Nuclear Modification R_{CP}

The nuclear modification R_{CP} can be obtained by using the particle spectra in the central collisions(0-20%) divided by the spectra in peripheral collisions(40-100%). Both collisions are normalized by their N_{bin} values(Table 3.2). We used the raw yield spectra since the difference of the efficiencies from various centralities is negligible in our analysis(see 3.12). Figure. 5.7 shows the nuclear modification factor (R_{CP}) as a function of p_T for the mesons (K_S^0, ϕ) and the baryons ($\Lambda + \overline{\Lambda}$, $\Xi^- + \overline{\Xi}^+$) at mid-rapidity($|y| < 0.5$ for the ϕ and $|y| < 1$ for all the others). The

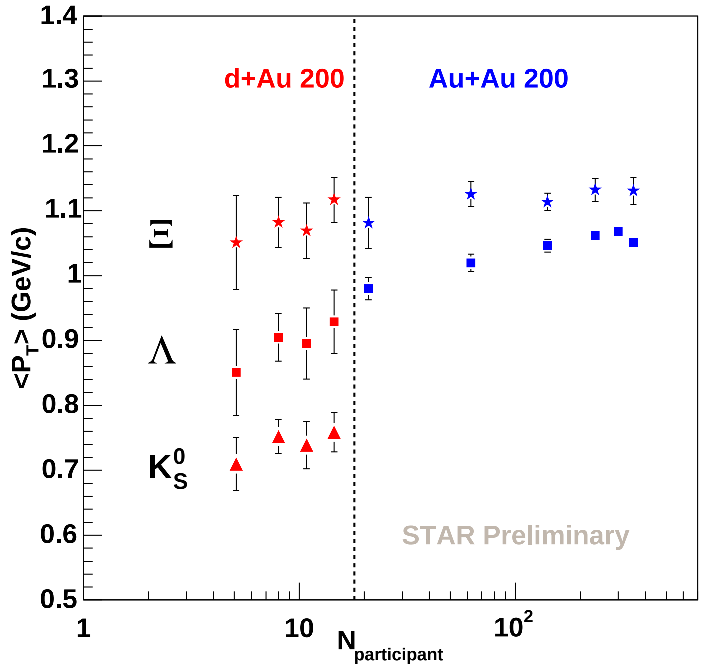

Figure 5.6: $\langle p_T \rangle$ vs. the number of participated nucleus $\langle N_{part} \rangle$ in d+Au(left of the dashed line) and Au+Au(right of the dashed line) 200 GeV for K^0_S, Λ+$\overline{\Lambda}$ and Ξ^-+$\overline{\Xi}^+$. The K^0_S $\langle p_T \rangle$ numbers lack. Errors include statistical and systematical errors for d+Au and statistical errors only for Au+Au.

ϕ R_{CP} has been measured by X.Z Cai at STAR [Cai04]. The number of binary collisions(N_{bin}) calculated from the model is 15.0 for the central collision(0-20%) and 4.0 for the peripheral collision(40-100%)(Table 3.2).

The R_{CP} ratio for each identified particle is identical and lower than unity in the low p_T region. When $p_T > 1$ GeV/c, the R_{CP} values for all the particles are above unity and the baryon(Λ and Ξ) R_{CP} values rise faster than those for the mesons(K^0_S and ϕ). At the intermediate p_T ($2 < p_T < 4$ GeV/c), the R_{CP} ratios are grouped into the mesons saturating at ~ 1.2 and the baryons saturating at ~ 1.5. When $p_T > 4$ GeV/c, we can not draw any conclusion due to the large error bars in R_{CP}. The R_{CP} numbers are listed in Table 5.2. The systematical

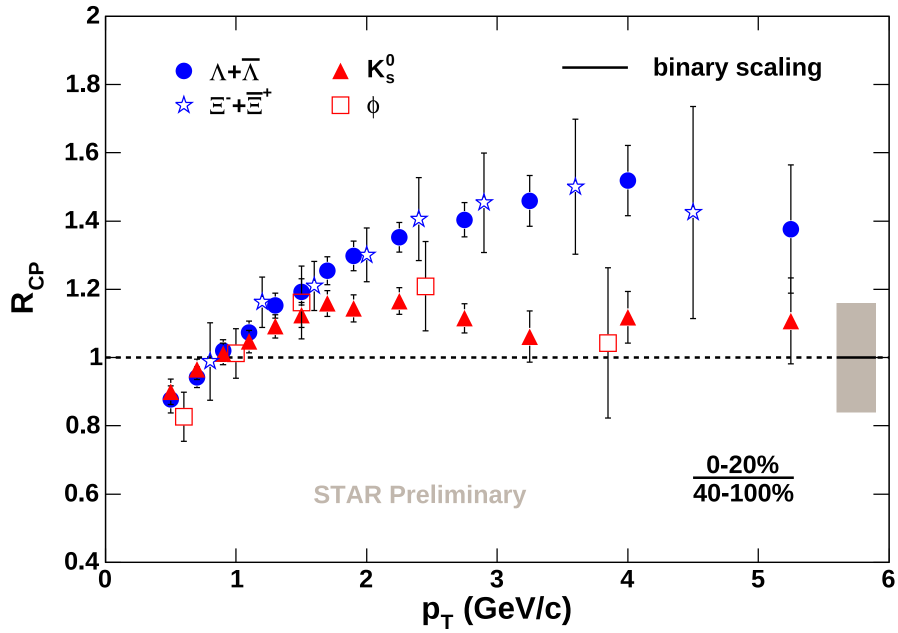

Figure 5.7: The Nuclear Modification R_{CP} for K_S^0, ϕ, $\Lambda + \overline{\Lambda}$ and $\Xi^- + \overline{\Xi}^+$ at mid-rapidity using the yields in the most central collision(0-20%) divided by those in the peripheral collision($40 - 100\%$). The gray band represents the normalization uncertainty of %16 for the binary scaling.

errors for the R_{CP} are small since central and peripheral collisions occur in the same system so that deviations due to different systems are cancelled.

p_T (GeV/c)	$K_S^0 \pm (stat) \pm (syst)$	$(\Lambda + \overline{\Lambda}) \pm (stat) \pm (syst)$
0.4 - 0.6	$0.900 \pm 0.0076 \pm 0.036$	$0.877 \pm 0.0183 \pm 0.035$
0.6 - 0.8	$0.965 \pm 0.0067 \pm 0.029$	$0.942 \pm 0.0101 \pm 0.028$
0.8 - 1.0	$1.010 \pm 0.0069 \pm 0.030$	$1.020 \pm 0.0096 \pm 0.031$
1.0 - 1.2	$1.047 \pm 0.0079 \pm 0.031$	$1.073 \pm 0.0099 \pm 0.032$
1.2 - 1.4	$1.091 \pm 0.0100 \pm 0.033$	$1.152 \pm 0.0114 \pm 0.035$
1.4 - 1.6	$1.125 \pm 0.0127 \pm 0.034$	$1.192 \pm 0.0130 \pm 0.036$
1.6 - 1.8	$1.158 \pm 0.0158 \pm 0.035$	$1.254 \pm 0.0155 \pm 0.038$
1.8 - 2.0	$1.144 \pm 0.0195 \pm 0.034$	$1.297 \pm 0.0190 \pm 0.039$
2.0 - 2.5	$1.165 \pm 0.0174 \pm 0.035$	$1.352 \pm 0.0160 \pm 0.041$
2.5 - 3.0	$1.115 \pm 0.0268 \pm 0.033$	$1.404 \pm 0.0272 \pm 0.042$
3.0 - 3.5	$1.061 \pm 0.0399 \pm 0.064$	$1.459 \pm 0.0463 \pm 0.058$
3.5 - 4.5	$1.118 \pm 0.0515 \pm 0.056$	$1.518 \pm 0.0702 \pm 0.076$
4.5 - 6.0	$1.107 \pm 0.0989 \pm 0.078$	$1.377 \pm 0.1690 \pm 0.083$
p_T (GeV/c)	$(\Xi^- + \overline{\Xi}^+) \pm (stat) \pm (syst)$	
0.6 - 1.0	$0.988 \pm 0.0907 \pm 0.069$	
1.0 - 1.4	$1.162 \pm 0.0577 \pm 0.046$	
1.4 - 1.8	$1.209 \pm 0.0535 \pm 0.048$	
1.8 - 2.2	$1.300 \pm 0.0593 \pm 0.052$	
2.2 - 2.6	$1.406 \pm 0.0882 \pm 0.084$	
2.6 - 3.2	$1.453 \pm 0.1038 \pm 0.102$	
3.2 - 4.0	$1.500 \pm 0.1568 \pm 0.120$	
4.0 - 5.0	$1.425 \pm 0.2894 \pm 0.114$	
p_T (GeV/c)	$\phi \pm (total)$	
0.4 - 0.8	0.826 ± 0.0719	
0.8 - 1.2	1.012 ± 0.0725	
1.2 - 1.8	1.161 ± 0.1065	
1.8 - 3.1	1.209 ± 0.1310	
3.1 - 4.6	1.425 ± 0.2202	

Table 5.2: The data points of R_{CP} for K_S^0, ϕ, $\Lambda + \overline{\Lambda}$ and $\Xi^- + \overline{\Xi}^+$ in d+Au collisions at $\sqrt{s_{NN}} = 200$ GeV.

CHAPTER 6

Discussion

The main goal for d+Au collisions at RHIC is to take d+Au measurements as a reference for comparison to results obtained in Au+Au collisions. Moreover, measurements on d+Au system itself is interesting to test many phenomenological models. From the comparison, we may better understand the dominant physical mechanisms that can explain the experimental results. In this section, we compare the data between d+Au and Au+Au collisions at the same beam energy $\sqrt{s_{NN}} = 200$ GeV to investigate the strangeness enhancement phenomena that was first observed at SPS. The Λ dN/dy at mid-rapidity and at forward rapidity are used to test the simulation calculations. The baryon enhancement at intermediate p_T(around 2 GeV/c) will be presented. The particle type dependence for the Cronin effect in d+Au collisions is discussed along with quark coalescence and recombination models.

6.1 $\Lambda(\Lambda)$ Production and Model Comparison

Many phenomenological approaches have been proposed to explain the p_T and rapidity dependence of the particle yield measured in d+Au collisions at RHIC experiments. Figure 6.1 shows the comparison of dN/dy for Λ, $\overline{\Lambda}$ and net Λ(Λ's-

$\overline{\Lambda}$'s) as well as the $\Lambda/\overline{\Lambda}$ ratio between the experimental results at STAR and various model calculations. The presented data points cover three rapidity(y) regimes: $-3 < y < -2.5$(Au side), $2.5 < y < 3.5$(deuteron side) and $-1 < y < 1$(mid-rapidity). The high $\Lambda/\overline{\Lambda}$ ratio(~ 0.82 at mid-rapidity) indicates a low net baryon density region at mid-rapidity in d+Au collisions.

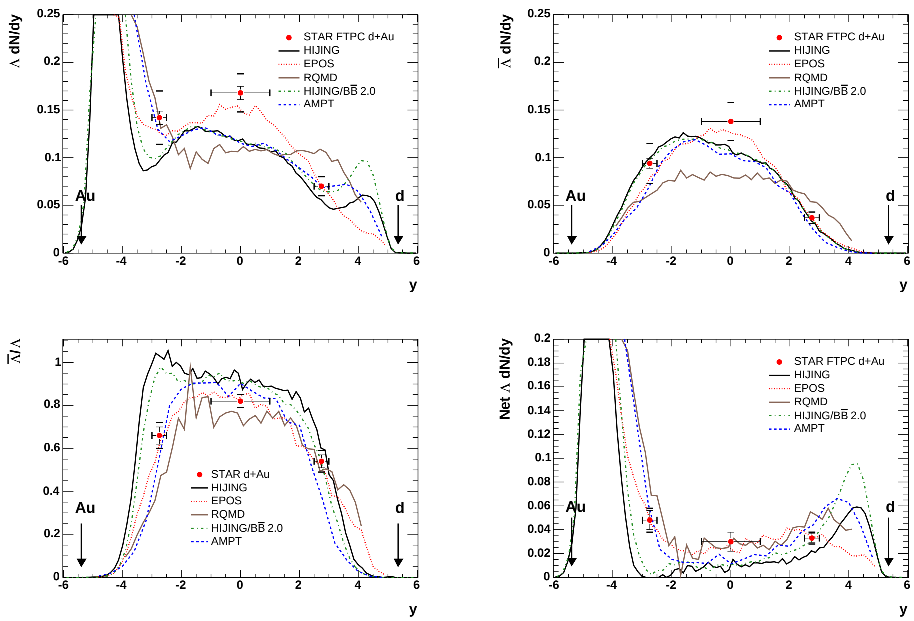

Figure 6.1: The particle yield dN/dy as a function of rapidity for Λ(top left), $\overline{\Lambda}$(top right), net Λ(bottom right) and the $\overline{\Lambda}/\Lambda$ ratio(bottom left). The error bars show the statistical and systematical errors. Beam rapidities are indicated by arrows. The forward rapidity data points are obtained from Frank Simon's thesis [Sim05]

A rise in dN/dy for the Λ on the Au side predicted in all models is caused by the baryon transport since the Λ contains a ud quark pair which also exists in the proton and neutron. This dN/dy rise disappears for the $\overline{\Lambda}$ due to the lack of $\bar{u}$ and $\bar{d}$ quarks in the nucleon. This baryon transport also affects the mid-rapidity dN/dy. From the comparison of the experimental results to the various model calculations, we see that the HIJING models [WG91, VG99] underpredict the yield on the Au side, the RQMD [Sor95] model overpredicts the yield on the deuteron side and the AMPT [Zha00, LK03] model predicts a yield lower than the measurement at mid-rapidity. The EPOS model agrees well with all the measured data within the errors.

EPOS [Wer04, Wer05] is a new version of the approach NeXus [Dre99] and is based on string theory and the parton model. In EPOS, the deuteron is considered to carry projectile partons and the Au carries target partons. Here the parton means quark, antiquark, diquark or antidiquark. The projectile and target partons interact and produce a 'parton ladder' that contains many soft(low p_T) and hard(high p_T) partons. The projectile and target partons themselves become excited partons called remnants. The parton ladders produce the particles at central rapidities and the remnants at large rapidities. Some produced partons have a large probability of interacting with another close target parton since there are many target partons available in Au. This causes the splitting of the parton ladder and leads to a 'collective hadronization' process. The EPOS calculation is also in agreement with the charged particle yields measured from PHOBOS, BRAHMS and STAR over a large pseudorapidity range, but underpredicts the data when $\eta < -3$. AMPT, a multi-phase model, well reproduces the whole rapidity spectra for the charged particles. It uses HIJING to generate the initial parton distribution and then simulates the parton rescattering by parton cascades [Zha98] and treats the hadronization with a fragmentation scheme [Sjo94].

From the models that successfully reproduce part of the data, like EOPS and AMPT, we believe that fragmentation schema based on pQCD calculations cannot alone describe the d+Au data and that multiple parton scatterings play an important role for particle mid-rapidity yields in d+Au collisions. This process may not be visible in proton-proton collisions due to the small system size and is probably surpassed by other mechanisms and becomes less pronounced in Au+Au collisions.

6.2 Strangeness Enhancement from d+Au to Au+Au

Large strangeness production has been considered to be a signature for the QGP formation [Raf82, RM86] as discussed in section 1.8. The previous heavy-ion experiments have reported that the strangeness production was increased significantly when going from pp, pA to AA collisions. In particular, the analysis of Pb-Pb collisions by WA97 at the CERN SPS has shown a strong enhancement in strange hadron yields by comparing to p-Pb collisions. The observed enhancement increases with the strangeness content($|S| = 1, 2, 3$) of the particle(left one in Figure 6.2). In WA97, the strangeness enhancement E was defined by [And99]

$$E = (\frac{\langle Y \rangle}{\langle N_{part} \rangle})_{Pb-Pb} / (\frac{\langle Y \rangle}{\langle N_{part} \rangle})_{p-Pb} \tag{6.1}$$

where $\langle Y \rangle$ and $\langle N_{part} \rangle$ are the yield and the number of participants, respectively, averaged over the full centrality range. According to the Schwinger mechanism for the string fragmentation, the production probability of a $s\bar{s}$ pair compared to a $u\bar{u}$ or $d\bar{d}$ pair is expressed as

$$\gamma_s = \frac{P(s\bar{s})}{P(q\bar{q})} = exp(-\frac{\pi(m_s^2 - m_q^2)}{2\kappa}) \tag{6.2}$$

where m_s and m_q are strange and light quark mass and κ is the string tension. The conventional N-body microscopic transport model UrQMD based on hadronic and string degrees of freedom fits well the p-Pb data but underpredicts the yield in central Pb-Pb collisions. Thus the predicted enhancement E is lower than that observed experimentally. However, it is believed that in central heavy ion collisions the string density can be so high due to early stage multiple scatterings that κ can increase from 1 GeV/fm to 3 GeV/fm. With this assumption, the UrQMD calculation gives an strangeness enhancement close to the experimental data [Sof99, Ble00a]. When applying this idea to Au+Au collisions at RHIC energy($\sqrt{s_{NN}} = 200$ GeV), the UrQMD model predicts an increase in the normalized yields from pp to $Au + Au$ by a factor of 7, 20 and 60 for Λ, Ξ and Ω, respectively [Ble00b].

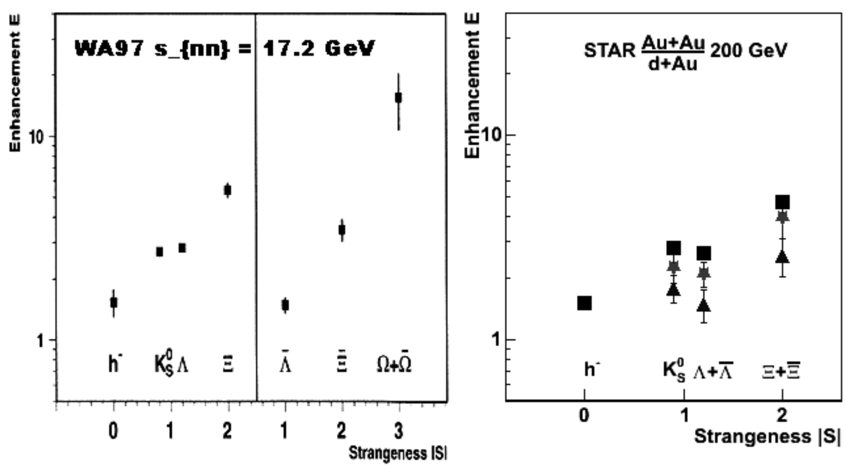

Figure 6.2: Strange particle enhancement vs. strangeness content at WA97(SPS) and STAR(RHIC). Left is the WA97 measurements on Pb-Pb and p-Pb collisions. Closed stars(triangles) in the right plot represent the ratio of 0-5%(40-60%) Au+Au to minbias d+Au at STAR. Closed squares in the right plot are the ratios from WA97(left) with combining the hyperon and anti-hyperon yields.

At STAR, we measured an enhancement factor similar to that derived in equation 6.1 for K^0_S, $\Lambda + \overline{\Lambda}$ and $\Xi^- + \overline{\Xi}^+$, but on Au+Au and d+Au systems. To compare with our results, the enhancement factors for $\Lambda + \overline{\Lambda}$ and $\Xi^- + \overline{\Xi}^+$ at WA97(SPS) were calculated from their individual ratios according to the anti-hyperon to hyperon yield ratios in Pb-Pb and p-Pb collisions. All the yields in the enhancement factor are normalized to the number of participants. We find the strangeness enhancement for the most central(0-5%) Au+Au to d+Au collisions is similar, within the error bars, to that for Pb-Pb to p-Pb collisions at WA97, and even lower for the Au+Au 40-60% centrality bin. Keeping in mind that the collision energy increases more than 10 times from SPS to RHIC, no huge increase in the strangeness enhancement with the beam energy seems to contradict the UrQMD prediction.

The canonical statistical model analysis of strange hadron production in central nucleus-nucleus collisions relative to pp or p-nucleus collisions shows that the strangeness enhancement decreases with increasing collision energy [Red01, RT02]. It is largest at $\sqrt{s_{NN}} = 8.7$ GeV as shown from the model calculation in Figure 6.3. This phenomena is due to the canonical suppression of particle thermal phase space at lower energies. According to the model, the strangeness enhancement at RHIC top energy $\sqrt{s_{NN}} = 200$ GeV should be lower than that at SPS, which qualitatively agrees with our measurements. So the strangeness enhancement seems not a unique signature of deconfinement since the initial conditions at energies where these features exist are unlikely for deconfinement. However, one may argue that the deconfined state has probably been created at the low SPS energy of $\sqrt{s_{NN}} = 8.7$ GeV where the temperature is much lower than at RHIC energy, but the net baryon density μ_B is higher such that it is still in the phase transition region, as shown in Figure 1.3.

The statistical model predicts that the N_{part} normalized yield is saturated at large N_{part}, which agrees with WA97 data but not with the STAR measurement where the normalized strange hadron yields increase with N_{part} and have no trend showing a saturation, even in the central Au+Au collisions(Figure 5.5).

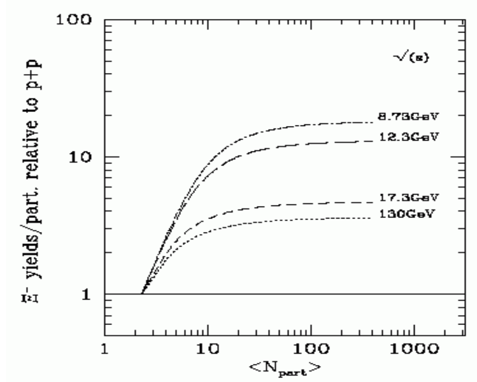

Figure 6.3: The enhancement of Ξ^- yields/participant in central Pb-Pb to p-p collisions at different collision energies from the statistical model.

6.3 Baryon Enhancement at intermediate p_T

The E735 [Ale73] and STAR [Ada05b] data for $\bar{p}p$ collisions, with $\sqrt{s} = 1.8$ TeV and $\sqrt{s} = 200$ GeV, respectively have shown that the baryon to meson ratio was less than ~ 0.5 at $p_T < 2$ GeV/c. The HJING simulation based on the string fragmentation schema fits well with the experimental data and predicts a ratio less than 0.5 over the whole p_T range [WG91, WG92]. However, at RHIC PHENIX has reported, for the first time, that proton yields exceed pion yields at $p_T > 2$ GeV/c in Au+Au collisions at $\sqrt{s} = 130$ GeV [Adc02] and that this anomaly cannot be explained by the conventional framework based on string fragmentation. At STAR, while the proton and pion measurement is limited by the p_T reach, the similar measurement, the Λ/K^0_S ratio, on the strange hadrons with p_T up to 6 GeV/c has been made for pp, Au+Au and d+Au collisions. Figure 6.4(left plot) show that the Λ/K^0_S ratio for pp collisions is saturated at ~ 0.5 in the p_T range of $1.5 - 4$ GeV/c, consistent with the p/π ratios in pp collisions mentioned above.

The model incorporating baryon junction dynamics [Kha96, VG99] and jet

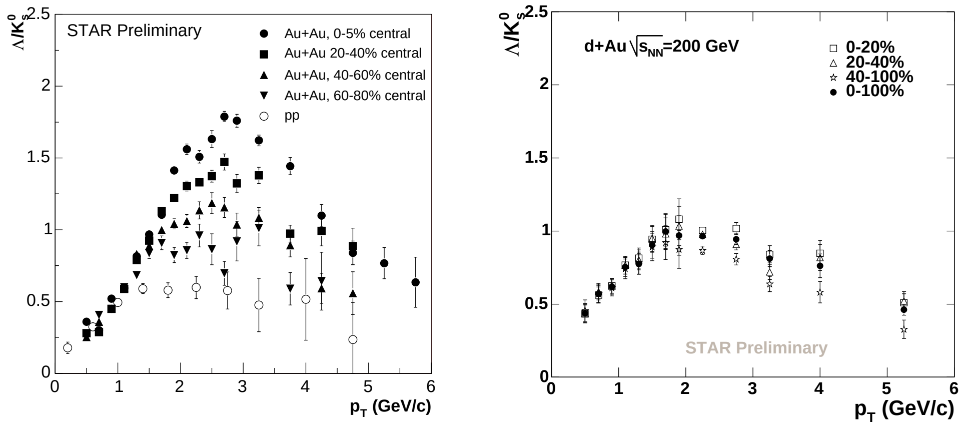

Figure 6.4: Λ/K_S^0 ratios in *pp*, Au+Au and d+Au at $\sqrt{s} = 200$ GeV. The Λ yield is not feeddown corrected. The errors are statistical only.

quenching is the first approach to qualitatively explain the baryon enhancement at the intermediate p_T [Vit01, VG02a]. This is a two component soft+hard dynamical model. At low p_T it is based on hydrodynamics and the particle yield depends on mass: lighter mesons are easier to produce than heavier baryons. At intermediate p_T perturbative pions are suppressed by jet quenching, while the nonperturbative baryon junction component would not be affected. Thus a baryon enhancement occurs. At high p_T pQCD dominates both mesons and baryons causing the ratio dropping down again. Since for the d+Au there is no jet quenching to suppress the pions and the baryon to meson ratio should be much smaller than those in Au+Au and close to the *pp* measurement. Our d+Au ratios(right in Figure 6.4), close to the peripheral Au+Au ratio, agrees with the predicted centrality dependence from this model.

Recently, the coalescence and recombination models allowing soft partons to coalesce into hadrons [Fri03] or soft and hard parton to recombine [Gre03] into hadrons also suggest a baryon enhancement at intermediate p_T. In a similar way to the baryon junction model, the pQCD string fragmentation mechanism dominates at high p_T in these models. In nucleus-nucleus collisions, it turns out the collective flow effect [Hec98, Sol93] on the intermediate p_T baryon yield is as strong as the effect due to the coalescence or recombination of partons [Gre03]. In the flow picture, heavier baryons tend to have larger momenta than mesons. In d+Au collisions, the flow effect is negligible, but the coalescence/recommbination idea is still applicable [HY04a, HY04c] and may explain the larger baryon enhancement than that in pp where parton coalescence/recombination is very small.

6.4 Cronin effect and Particle type dependence

The Cronin effect [Cro75] has been widely observed in the fixed target pA collisions [Str92]. The enhancement at intermediate p_T(usually $>\sim$ 1.5 GeV/c) was explained by the initial multiple hadronic or partonic rescatterings as introduced in section 1.9.2. Recently these traditional models based on the multiple rescatterings have been applied to the RHIC d+Au collisions at 200 GeV. They predicted a peak value of 1.1 - 1.5 in nuclear modification factor R_{AA} or R_{CP} [Acc03]. The d+Au experimental measurement on the charged hadron R_{AA} at STAR shows a maximum of $\sim$ 1.5 at $2.5 < p_T < 4$ GeV/c agreeing with the prediction.

Our R_{CP} measurements on the identified strange hadrons, K_S^0, ϕ, $\Lambda + \overline{\Lambda}$ and $\Xi^- + \overline{\Xi}^+$ covering the p_T up to 6 GeV/c seem to support the initial state model calculations(right in figure 6.5). The R_{CP} ratios peak at $\sim$ 1.2 for the measons, K_S^0 and ϕ, while $\sim$ 1.5 for the baryons $\Lambda + \overline{\Lambda}$ and $\Xi^- + \overline{\Xi}^+$.

However, it is not easy for these initial state based models to explain the grouping effect shown in R_{CP} for both d+Au and Au+Au collisions at 200 GeV.

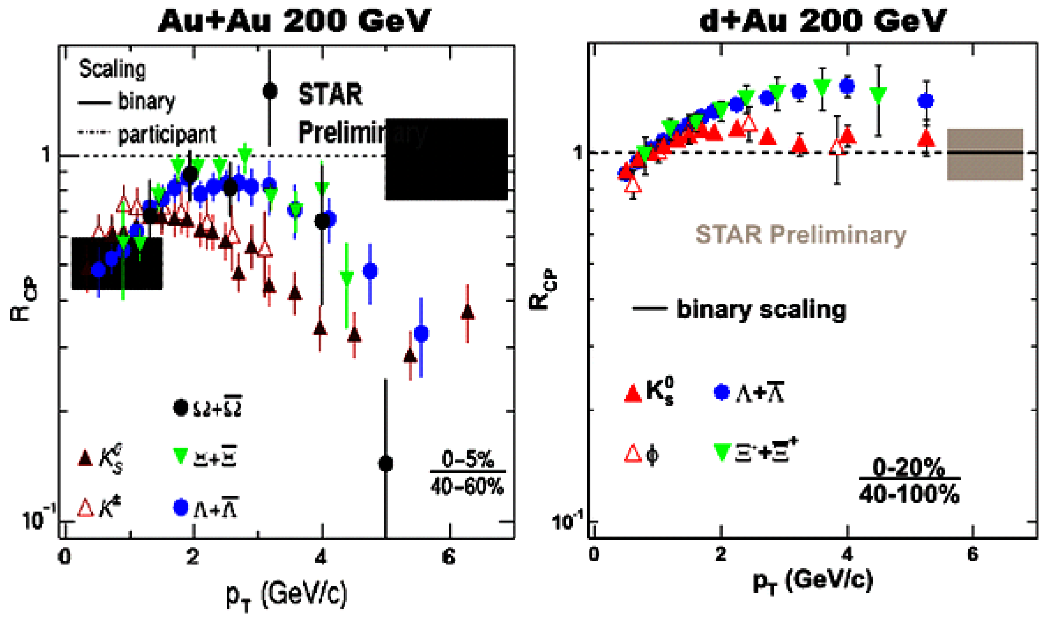

Figure 6.5: R_{CP} for strange hadrons from Au+Au and d+Au 200 GeV at RHIC. R_{CP} ratios are grouped into two particle types: mesons and baryons in both systems. Errors include statistical and systematic errors.

They are blind to the hadron species. In Au+Au collisions though the R_{CP} values for the measured strangeness particles are below unity due to the suppression from the jet quenching effect, and their separation into mesons and baryons is even more pronounced than that from the d+Au measurement(left in figure 6.5). Since the particle type dependence should be directly related to the hadronization stage, the final state effects as implemented in the recombination/coalescence models may definitely influence the Cronin effect at high energy heavy ions collisions. It should be pointed out even in pA collisions, the particle dependence has existed: the proton R_{AA} is obviously higher than kaon's and pion's while the latter two have close R_{AA} [Str92]. The origin of this phenomena remains unknown.

We will introduce the recombination model of Hwa et al. [HY04b, HY04a, HY04c] to see a possible yet natural way to explain the particle type dependence in the Cronin effect. In this model the traditional parton fragmentation is interpreted by the recombination process. The distribution of hadron production as a function of its momentum is treated for mesons and baryons in a different way. For mesons formed by quark and anti-quark, the distribution can be written as

$$p\frac{dN_M}{dp} = \int \frac{dp_1}{p_1}\,\frac{dp_2}{p_2}\,F_{q\bar{q}'}(p_1,p_2)R_M(p_1,p_2,p) \tag{6.3}$$

where $F_{q\bar{q}'}(p_1,p_2)$ is the joint distribution of a quark and an antiquark $\bar{q}'$, and $R_M(p_1,p_2,p)$ is the recombination function(RF) for $q\bar{q}' \rightarrow M$. $F_{q\bar{q}'}(p_1,p_2)$ can be expressed in a schematic way:

$$F_{q\bar{q}'} = TT + TS + SS \tag{6.4}$$

where T denotes soft(low p_T) parton distribution and S shower(high p_T) parton distribution. At very high p_T the third term SS obtained from pQCD calculations dominates and the recombination process gives the same effect as the fragmentation. However, in d+Au collisions at RHIC energies soft partons are abundant enough to affect the final hadron yield at low and intermediate p_T even in the mid-rapidity region. The first term in Eq. 6.4 giving the low p_T thermal contribution is determined by fitting the d+Au data at low p_T using a p_T exponential function

$$\frac{C^2}{6}\,exp(-p/T) \tag{6.5}$$

where C and T are two fit parameters. The second term whose magnitude influences the yield at the intermediate p_T, is the key component in the model.

For three quark baryons, the distribution can be written using three quark joint and recombination functions,

$$p^0\frac{dN_B}{dp} = \int \frac{dp_1}{p_1}\frac{dp_2}{p_2}\frac{dp_3}{p_3}\,F(p_1,p_2,p_3)R_B(p_1,p_2,p_3,p) \tag{6.6}$$

Being different from mesons, $F(p_1, p_2, p_3)$ for baryons can be expressed as

$$F_{qq'q''} = TTT + TTS + TSS + SSS \tag{6.7}$$

where the first term TTT stands for the low p_T thermal contribution and is proportional to

$$\frac{C^3}{6}\frac{p^2}{p_0}\,exp(-p/T) \tag{6.8}$$

The last term SSS is the shower contribution for the high p_T and the thermal-shower contribution $TTS + TSS$ has a quite different behavior from that for mesons where it gives TS.

From the recombination scheme, the hadron distribution depends strongly on the number of quarks in a hadron as seen in equations 6.4, 6.7 and slightly on the hadron mass that enters in through the total energy p_0 and the fit parameter T(a heavier particle may give a larger T). Therefore it could naturally describe the dependence on particle type instead of on the particle mass observed in our strange hadron R_{CP} measurement. The ϕ mass is close to Λ's, yet the R_{CP} is close to K^0_S. Furthermore, the model is not dependent on quark constituents in a hadron so all the light and strange mesons are expected to follow the same R_{CP} trend, and the same for baryons. At STAR, due to the limited statistics for protons and the identification limitation for pions at $p_T > 1.5$ GeV/c in d+Au TOF data, it is hard to compare our strange hadron R_{CP} with that for protons and pions. The PHENIX collaboration has measured the R_{CP} of the pion up to 2.4 GeV/c and the R_{CP} of the proton up to 3 GeV/c. Unfortunately, they have used a different centrality definition from the STAR making the direct comparison impossible. However, some qualitative behaviors are same: there exists an clear enhancement in the intermediate p_T for both mesons and baryons and the baryon R_{CP} ratios are higher than those for mesons. At PHENIX, the pion R_{CP} reaches a maximum at ~ 1.3 and the proton R_{CP} reaches a maximum at ~ 1.9. The origin of the greater R_{CP} for the proton is mainly from the fact that the thermal term TTT for the proton (proportional to C^3 in equation 6.8) is more sensitive to centrality than the term TT for the pion(proportional to C^2 in equation 6.5). This causes the $TTS + TSS$ contribution to be negligible in peripheral collisions while comparable with other component contributions in central collisions. This should also explain our result for strange hadrons: the R_{CP} ratios for Λ and Ξ are greater than those for K_S^0 and ϕ. To confirm the effectiveness of the recombination model, the R_{CP} measurement on more particle species over a wider p_T range is necessary.

6.5 Implications for Au+Au Collisions

From the R_{CP} measurement for charged hadrons(Figure 1.7) and strange hadrons(Figure 6.5) from 200 GeV Au+Au collisions at RHIC, a clear strong suppression for central collisions at mid-rapidity for $p_T > 5$ GeV/c was seen. This suppression could be explained either by final-state effects(pQCD-I [Wan04a] and pQCD-II [VG02b]) based on pQCD incorporating partonic energy loss in dense matter or by initial-state effects from the gluon saturation mechanism [Kha03]. While the latter predicted a suppression in hadron production in d+Au collisions, the former did not since no dense matter is expected to be created in d+Au collisions, thus partonic energy loss is negligible. The observed enhancements in mid-rapidity charged and strange hadron production in d+Au as seen in Figures 1.10 and 6.5 indicate that the suppression is due to the final-state effect: energy loss in the medium. Further, a detailed hadronic transport calculation [Cas04] has shown that the hadronic absorption in the medium fails to account for the observed suppression suggesting that the experimentally observed suppression is due to partonic rather than hadronic energy loss. However, it is difficult to tell if this medium causing the energy loss is already deconfined to partonic matter or still in the hadronic state.

Another interesting phenomenon occurred at intermediate p_T is the grouping effect in R_{CP} as discussed in Section 6.4: baryons follow the same trend regardless of the type and mass of their constituent quarks while mesons follow another trend also independent of the type and mass of their constituent of quark and antiquark(Figure 6.5). A natural way to understand this grouping effect has been given in the framework of parton coalescence and recombination in which two quarks coalesce or recombine to a meson while three quarks to a baryon. The larger R_{CP} difference in Au+Au collisions than that in d+Au implies, according to these model assumptions, that abundant soft partons exist in the central Au+Au system favoring the formation of baryons at intermediate p_T. Therefore assuming the existence of a soft partonic matter filled with quarks and gluons would explain the R_{CP} over the whole p_T range: the high p_T suppression due to hard partons traversing through this soft partonic matter and losing energy, and the intermediate p_T grouping effect (mesons vs. baryons) due to the recombination of partons from this partonic source. The assumption of hadronic matter, however, cannot explain the latter one. If this picture is correct, we would expect the same grouping effect in the v_2 measurement. Figure 6.6 shows the v_2 values scaled by the number of constituent quarks (n) for identified hadrons from RHIC Au+Au collisions. While v_2 is significantly different for mesons and baryons at

$p_T > 2$ GeV/c, v_2/n is close for all particles. This quark level v_2 indicates the momentum space azimuthal anisotropy for hadrons at the hadronization stage may develop from partonic matter existing at the early stage [MV03].

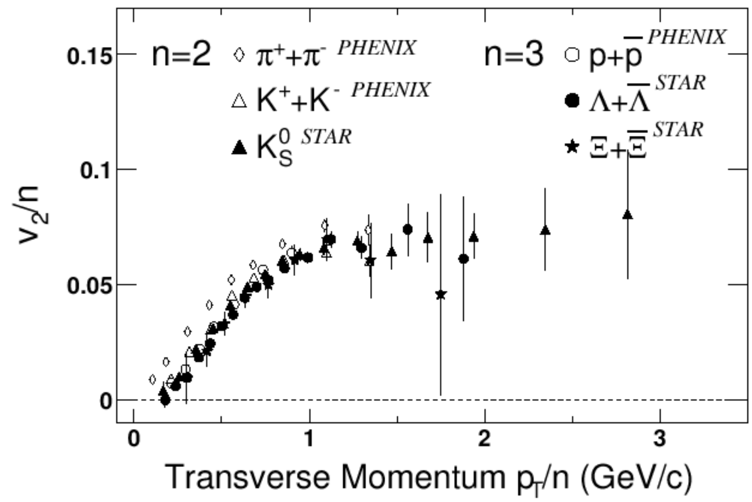

Figure 6.6: v_2 for identified particles scaled by the number of constituent quarks (n) versus p_T/n from Au+Au 200 GeV collisions at RHIC.

6.6 Conclusions

In summary, we have reported the measurements of transverse mass and momentum spectra at mid-rapidity($|y| < 1$) for the identified strange hardons: K^0_S, $\Lambda + \overline{\Lambda}$ and $\Xi^- + \overline{\Xi}^+$ from d+Au collisions at RHIC. The measured p_T covers $0.4 < p_T < 6.0$ GeV/c for K^0_S, $\Lambda + \overline{\Lambda}$ and $0.6 < p_T < 5.0$ GeV/c for $\Xi^- + \overline{\Xi}^+$.

The dN/dy normalized to the number of participants increase with the multiplicity measured in the TPC. The $\Lambda(\overline{\Lambda})$ dN/dy values at the mid-rapidity and forward rapidity regions agree with the prediction from the EPOS model, which indicates that multiple parton scatterings are important in determining the final hadron yield in d+Au collisions. The measured Λ/K_S^0 ratios show the greatest baryon enhancement at $p_T \sim 2$ GeV/c in d+Au collisions, very close to the Au+Au peripheral collisions(60-80%).

The strangeness enhancement going from d+Au to Au+Au collisions grows with the number of strange quark in a hadron. The magnitude of the enhancement is in the same order as that at SPS collision energy. If the strangeness enhancement is a signal of the deconfined matter, it suggests that at the SPS energy($\sqrt{s} = 17.4$ GeV) the QGP has been probably created at a lower temperature yet a larger net baryon chemical potential.

The nuclear modification factors R_{CP} normalized to binary collisions indicate that the Cronin effect in d+Au collisions has a distinct particle type dependence. The R_{CP} ratios show a distinct baryon versus meson dependence: the R_{CP} for $\Xi^-+\overline{\Xi}^+$ follows that for $\Lambda+\overline{\Lambda}$ while the R_{CP} for the ϕ(analysis by Xiangzhou Cai) is close to that for the K_S^0. The particle type dependence of R_{CP} is obviously out of the framework of initial state effects. Hadronization processes, as suggested by coalescence and recombination models, are likely to be important for explaining hadron spectra and the Cronin effect in high-energy d+Au collisions.

6.7 Future Directions

The confirmation of the transition from a hadron-gas state to a quark-gluon matter QGP needs many experimental crosschecks covering an energy range from the low energy nucleus-nucleus collisions where the QGP is not expected to form to the high energy nucleus-nucleus collisions where the QGP is predicted by the LQCD calculations. It is necessary to find the critical collision energy below which the system could be thought to be in a hadronic gas state. For this purpose in 2004, Au+Au collisions at $\sqrt{s_{NN}}$ = 62 GeV have run at RHIC STAR. The results for 62 GeV collisions have shown no significant difference from those at 200 GeV, suggesting that the QGP might have formed even in this lower energy. Experiments at even lower collision energy are necessary.

Since the QGP exists only in bulk matter, the change of system size would affect the formation of QGP. Cu+Cu collisions at 200 GeV has been run at RHIC in 2005. The comparison of R_{CP} and v_2 between the Au+Au and the Cu+Cu may reveal to what extent the system size would influence the meson vs baryon effect and the suppression due to the jet quenching.

From the analysis viewpoint, more data are needed to push the p_T reach into the fragmentation area($p_T > 5$ GeV/c from current estimates) to test if R_{CP} for mesons and baryons merge or not.

APPENDIX A

Kinematic Variables

A.1 Transverse Momentum and Mass

A particle produced from the collision is characterized by its mass m and three momentum components p_x, p_y and p_z where z is along the beam direction. Of special interest is the transverse momentum

$$p_T = \sqrt{p_x^2 + p_y^2} \tag{A.1}$$

because it is invariant under the Lorentz transformations along the beam direction. Another transverse variable often used for the thermal particles at low p_T region is the transverse mass that is defined as

$$m_T = \sqrt{p_T^2 + m^2} \tag{A.2}$$

and the transverse kinetic energy of the particle is $m_T - m$ which is invariant under the Lorentz transformations along z direction.

A.2 Rapidity and Pseudorapidity

The longitudinal variable rapidity y is defined as

$$y = \frac{1}{2} \ln \left(\frac{E + p_z}{E - p_z} \right) \tag{A.3}$$

where $E=\sqrt{p^2 + m^2}$ is the particle energy and rapidity is also invariant and additive under Lorentz transformations along z. Usually, the mass of an unidentified particle is unknown but its momentum can be measured experimentally. In that case, we often use the pseudo-rapidity that defined as

$$\eta = \frac{1}{2} \ln \left(\frac{p + p_z}{p - p_z} \right) \tag{A.4}$$

For $p \gg m$, η is a good approximation for the rapidity y. The pseudo-rapidity can be written as

$$\eta = -\ln \left[\tan \left(\theta/2 \right) \right]. \tag{A.5}$$

where θ is the angle between the particle momentum $\boldsymbol{p}$ and the beam axis.

APPENDIX B

Momentum Space and Invariant Yields

In this section the differential cross section and the Lorentz invariant yield will be discussed. First we introduce the differential yield, d^3N/dp^3, that is the number of particles emitted into a particular momentum space bin in a collision. The total yield for a particular particle is obtained by integrating the differential yield over the whole momentum space,

$$N = \int \frac{d^3N}{dp^3} d^3p \tag{B.1}$$

which is obviously Lorentz invariant. The momentum-space volume element, d^3p, however, is not invariant and it transforms as $dp' = \gamma dp$ between two frames. So the differential yield in d^3N/dp^3 is frame dependent and is not convenient for the comparison between two experiments since we have to specify which frame is referred to. So finding an invariant variable that is close to the differential yield is necessary.

Recall that the differential momentum-space volume d^4p is invariant ($dE' = dE/\gamma$), but it includes momentum-space region in which particles are off-shell. Requiring particles to be on-shell, we obtain:

$$\int \delta(p \cdot p - m^2) d^4p = \int \delta(E^2 - |\mathbf{p}|^2 - m^2) d^3p \, dE = \frac{d^3p}{2E}. \tag{B.2}$$

The left hand side of this expression is invariant (the delta function is invariant since its argument is), and we have used $\delta(f(x)) = \sum_i \delta(x - x_i)/|f'(x)|$, where the x_i are the zeros of $f(x)$. So the momentum-space volume element d^3p/E is Lorentz invariant. We rewrite Equation B.1 as

$$N = \int E \frac{d^3N}{dp^3} \frac{d^3p}{E}. \tag{B.3}$$

Therefore the differential yield, Ed^3N/dp^3, must be Lorentz invariant. Using the Jacobian transformation from (p_x, p_y, p_z) to (p_T, y, ϕ), we have

$$\frac{dp_x dp_y dp_z}{E} = p_T \, dp_T \, dy \, d\phi. \tag{B.4}$$

where p_T, y, ϕ are transverse momentum, rapidity and azimuthal angle. The total yield is then

$$N = \int \frac{d^3N}{p_T \, dp_T \, dy \, d\phi} p_T \, dp_T \, dy \, d\phi. \tag{B.5}$$

For the first order approximation in heavy ion collisions, the azimuthal angle distribution is assumed isotropic. Performing the integral over ϕ, the total yield becomes:

$$N = \int \frac{d^2N}{2\pi p_T \, dp_T \, dy} 2\pi p_T \, dp_T \, dy. \tag{B.6}$$

Since $2\pi p_T \, dp_T \, dy$ and the total yield N are Lorentz invariant(see A),

$$\frac{d^2N}{2\pi p_T \, dp_T \, dy} \tag{B.7}$$

is also Lorentz invariant. This is known as the invariant transverse momentum yield(or spectrum). We further observe that $p_T \, dp_T = m_T \, dm_T$, so that

$$\frac{d^2N}{2\pi m_T \; dm_T \; dy} = \frac{d^2N}{2\pi p_T \; dp_T \; dy} \tag{B.8}$$

which is known as the invariant transverse mass yield(or spectrum).

APPENDIX C

$\langle p_T \rangle$ from double exponential function

The mean $p_T(\langle p_T \rangle)$ could be calculated numerically from the p_T spectrum fit function. In our analysis, double exponential function has been used. From equation B.8, the amplitude of p_T spectrum is the same as that of m_T spectrum so we rewrite the double exponential function(Eq. 5.1) in p_T format

$$\frac{d^2N}{2\pi p_T\, dp_T\, dy} = \frac{dN}{2\pi dy}\left(\frac{a}{T_1(m_0+T_1)}e^{-\frac{(\sqrt{p_T^2+m_0^2}-m_0)}{T_1}} + \frac{(1-a)}{T_2(m_0+T_2)}e^{-\frac{(\sqrt{p_T^2+m_0^2}-m_0)}{T_2}}\right) \tag{C.1}$$

where dN/dy, T_1, T_2 and a are four parameters. Here we have used the identity

$$1 = \int\left(\frac{a}{T_1(m_0+T_1)}e^{-\frac{(\sqrt{p_T^2+m_0^2}-m_0)}{T_1}} + \frac{(1-a)}{T_2(m_0+T_2)}e^{-\frac{(\sqrt{p_T^2+m_0^2}-m_0)}{T_2}}\right)p_T\, dp_T \tag{C.2}$$

The $\langle p_T \rangle$ in a specific rapidity region is defined as

$$\langle p_T \rangle = \frac{\int p_T \frac{d^2N}{dp_T\, dy} dp_T}{\int \frac{d^2N}{dp_T\, dy} dp_T} \tag{C.3}$$

where the denominator integral is the normalization factor. With the help of equations C.1 and C.2, equation C.3 can be simplified to

$$\langle p_T \rangle = \int p_T^2 \left(\frac{a}{T_1(m_0 + T_1)} e^{-\frac{(\sqrt{p_T^2 + m_0^2} - m_0)}{T_1}} + \frac{(1-a)}{T_2(m_0 + T_2)} e^{-\frac{(\sqrt{p_T^2 + m_0^2} - m_0)}{T_2}}\right) dp_T \tag{C.4}$$

Replacing the integral with the summation and dp_T with δp_T, we can calculate the $\langle p_T \rangle$ in a numerical way

$$\langle p_T \rangle = A \sum p_T^2 * e^{-\frac{(\sqrt{p_T^2 + m_0^2} - m_0)}{T_1}} \delta p_T + B \sum p_T^2 * e^{-\frac{(\sqrt{p_T^2 + m_0^2} - m_0)}{T_2}} \delta p_T \tag{C.5}$$

where $A = \frac{a}{T_1(m_0+T_1)}$, $B = \frac{1-a}{T_2(m_0+T_2)}$ and δp_T is a small p_T interval. In practice, p_T in the summation goes from 0 to a p_T reach such that the contribution above this p_T can be ignored. Usually this p_T is not necessary to be chosen very large since the spectrum is exponentially dropping.

APPENDIX D

The STAR Collaboration

STAR Collaboration Author List

J. Adams[3], M.M. Aggarwal[29], Z. Ahammed[43], J. Amonett[20], B.D. Anderson[20], D. Arkhipkin[13], G.S. Averichev[12], S.K. Badyal[19], Y. Bai[27], J. Balewski[17], O. Barannikova[32], L.S. Barnby[3], J. Baudot[18], S. Bekele[28], V.V. Belaga[12], A. Bellingeri-Laurikainen[38], R. Bellwied[46], J. Berger[14], B.I. Bezverkhny[48], S. Bharadwaj[33], A. Bhasin[19], A.K. Bhati[29], V.S. Bhatia[29], H. Bichsel[45], J. Bielcik[48], J. Bielcikova[48], A. Billmeier[46], L.C. Bland[4], C.O. Blyth[3], S. Blyth[21], B.E. Bonner[34], M. Botje[27], A. Boucham[38], J. Bouchet[38], A.V. Brandin[25], A. Bravar[4], M. Bystersky[11], R.V. Cadman[1], X.Z. Cai[37], H. Caines[48], M. Calderón de la Barca Sánchez[17], J. Castillo[21], O. Catu[48], D. Cebra[7], Z. Chajecki[28], P. Chaloupka[11], S. Chattopadhyay[43], H.F. Chen[3]6, Y. Chen[8], J. Cheng[41], M. Cherney[1]0, A. Chikanian[48], W. Christie[4], J.P. Coffin[18], T.M. Cormier[46], M.R. Cosentino[35], J.G. Cramer[45], H.J. Crawford[6], D. Das[43], S. Das[43], M. Daugherity[40], M.M. de Moura[35], T.G. Dedovich[12], A.A. Derevschikov[31], L. Didenko[4], T. Dietel[14], S.M. Dogra[19], W.J. Dong[8], X. Dong[36], J.E. Draper[7], F. Du[48], A.K. Dubey[15], V.B. Dunin[12], J.C. Dunlop[4], M.R. Dutta Mazumdar[43], V. Eckardt[23], W.R. Edwards[21], L.G. Efimov[12], V. Emelianov[25], J. Engelage[6], G. Eppley[34], B. Erazmus[38], M. Estienne[38], P. Fachini[4], J. Faivre[18], R. Fatemi[17], J. Fedorisin[12], K. Filimonov[21], P. Filip[11], E. Finch[48], V. Fine[4], Y. Fisyak[4], K.S.F. Fornazier[35], J. Fu[41], C.A. Gagliardi[39], L. Gaillard[3], J. Gans[48], M.S. Ganti[43], F. Geurts[25], V. Ghazikhanian[8], P. Ghosh[43], J.E. Gonzalez[8], H. Gos[44], O. Grachov[46], O. Grebenyuk[27], D. Grosnick[42], S.M. Guertin[8], Y. Guo[46], A. Gupta[19], T.D. Gutierrez[7], T.J. Hallman[4], A. Hamed[46], D. Hardtke[21], J.W. Harris[48], M. Heinz[2], T.W. Henry[39], S. Heppelmann[30], B. Hippolyte[18], A. Hirsch[32], E. Hjort[21], G.W. Hoffmann[40], M. Horner[21], H.Z. Huang[8], S.L. Huang[36], E.W. Hughes[5], T.J. Humanic[28], G. Igo[8], A. Ishihara[40], P. Jacobs[21], W.W. Jacobs[17], M Jedynak[44], H. Jiang[8], P.G. Jones[3], E.G. Judd[6], S. Kabana[2], K. Kang[41], M. Kaplan[9], D. Keane[20], A. Kechechyan[12], V.Yu. Khodyrev[12], J. Kiryluk[2]2, A. Kisiel[44], E.M. Kislov[12], J. Klay[21], S.R. Klein[21], D.D. Koetke[42], T. Kollegger[14], M. Kopytine[20], L. Kotchenda[25], K.L. Kowalik[21], M. Kramer[26], P. Kravtsov[25], V.I. Kravtsov[31], K. Krueger[1], C. Kuhn[18], A.I. Kulikov[12], A. Kumar[29], R.Kh. Kutuev[13], A.A. Kuznetsov[12], M.A.C. Lamont[48], J.M. Landgraf[4], S. Lange[14], F. Laue[4], J. Lauret[4], A. Lebedev[4], R. Lednicky[12], S. Lehocka[12], M.J. LeVine[4], C. Li[36], Q. Li[46], Y. Li[41], G. Lin[48], S.J. Lindenbaum[26], M.A. Lisa[28], F. Liu[47], H. Liu[36], J. Liu[34], L. Liu[47], Q.J. Liu[45], Z. Liu[47], T. Ljubicic[4], W.J. Llope[34], H. Long[8], R.S. Longacre[4], M. Lopez-Noriega[28], W.A. Love[4], Y. Lu[47], T. Ludlam[4], D. Lynn[4], G.L. Ma[37], J.G. Ma[8], Y.G. Ma[37], D. Magestro[28], S. Mahajan[19], D.P. Mahapatra[15], R. Majka[48], L.K. Mangotra[19], R. Manweiler[42], S. Margetis[20], C. Markert[20], L. Martin[38], J.N. Marx[21], H.S. Matis[21], Yu.A. Matulenko[31], C.J. McClain[1], T.S. McShane[10], F. Meissner[21], Yu. Melnick[31], A. Meschanin[31], M.L. Miller[22], N.G. Minaev[31], C. Mironov[20], A. Mischke[27], D.K. Mishra[15], J. Mitchell[34], B. Mohanty[43], L. Molnar[32], C.F. Moore[40], D.A. Morozov[31], M.G. Munhoz[35], B.K. Nandi[43], S.K. Nayak[19], T.K. Nayak[43], J.M. Nelson[3], P.K. Netrakanti[43], V.A. Nikitin[13], L.V. Nogach[31], S.B. Nurushev[31], G. Odyniec[21], A. Ogawa[4], V. Okorokov[25], M. Oldenburg[21], D. Olson[21], S.K. Pal[43], Y. Panebratsev[12], S.Y. Panitkin[4], A.I. Pavlinov[46], T. Pawlak[44], T. Peitzmann[27], V. Perevoztchikov[4], C. Perkins[6], W. Peryt[44], V.A Petrov[46], S.C. Phatak[15], R. Picha[7], M. Planinic[49], J. Pluta[46], N. Porile[32], J. Porter[45], A.M. Poskanzer[21], M. Potekhin[4], E. Potrebenikova[12], B.V.K.S. Potukuchi[19], D. Prindle[45], C. Pruneau[46], J. Putschke[21], G. Rakness[30], R. Raniwala[33], S. Raniwala[33], O. Ravel[38], R.L. Ray[40], S.V. Razin[12], D. Reichhold[32], J.G. Reid[45], J. Reinnarth[38], G. Renault[38], F. Retiere[21], A. Ridiger[25], H.G. Ritter[21], J.B. Roberts[34], O.V. Rogachevski[12], J.L. Romero[7], A. Rose[21], C. Roy[38], L. Ruan[36], M.J. Russcher[27], R. Sahoo[15], I. Sakrejda[21], S. Salur[48], J. Sandweiss[48], M. Sarsour[17], I. Savin[13], P.S. Sazhin[12], J. Schambach[40], R.P. Scharenberg[32], N. Schmitz[23], K. Schweda[21], J. Seger[10], P. Seyboth[23], E. Shahaliev[12], M. Shao[36], W. Shao[5], M. Sharma[29], W.Q. Shen[37], K.E. Shestermanov[31], S.S. Shimanskii[12], E Sichtermann[21], F. Simon[23], R.N. Singaraju[43], N. Smirnov[48], R. Snellings[27], G. Sood[42], P. Sorensen[21], J. Sowinski[17], J. Speltz[18], H.M. Spinka[1], B. Srivastava[32], A. Stadnik[12], T.D.S. Stanislaus[42], R. Stock[14], A. Stolpovsky[46], M. Strikhanov[25], B. Stringfellow[32], A.A.P. Suaide[35], E. Sugarbaker[28], C. Suire[4], M. Sumbera[11], B. Surrow[22], M. Swanger[10], T.J.M. Symons[21], A. Szanto de Toledo[35], A. Tai[8], J. Takahashi[35], A.H. Tang[27], T. Tarnowsky[32], D. Thein[8], J.H. Thomas[21], S. Timoshenko[25], M. Tokarev[12], T.A. Trainor[45], S. Trentalange[8], R.E. Tribble[39], O. Tsai[8], J. Ulery[32], T. Ullrich[4], D.G. Underwood[1], G. Van Buren[4], M. van Leeuwen[21], A.M. Vander Molen[24], R. Varma[16], I.M. Vasilevski[13], A.N. Vasiliev[31], R. Vernet[18], S.E. Vigdor[17], Y.P. Viyogi[43], S. Vokal[12], S.A. Voloshin[46], W.T. Waggoner[10], F. Wang[32], G. Wang[20], G. Wang[5], X.L. Wang[36], Y. Wang[41], Z.M. Wang[36], H. Ward[40], J.W. Watson[20], J.C. Webb[17], G.D. Westfall[24], A. Wetzler[21], C. Whitten Jr. [8], H. Wieman[21], S.W. Wissink[17], R. Witt[2], J. Wood[8], J. Wu[36], N. Xu[21], Z. Xu[4], Z.Z. Xu[36], E. Yamamoto[21], P. Yepes[34], V.I. Yurevich[12], I. Zborovský[11], H. Zhang[4], W.M. Zhang[20], Y. Zhang[36], Z.P. Zhang[36], R. Zoulkarneev[13], Y. Zoulkarneeva[13], A.N. Zubarev[12]

(STAR Collaboration)

[1]Argonne National Laboratory, Argonne, Illinois 60439
[2]University of Bern, 3012 Bern, Switzerland
[3]University of Birmingham, Birmingham, United Kingdom
[4]Brookhaven National Laboratory, Upton, New York 11973
[5]California Institute of Technology, Pasadena, California 91125
[6]University of California, Berkeley, California 94720
[7]University of California, Davis, California 95616
[8]University of California, Los Angeles, California 90095
[9]Carnegie Mellon University, Pittsburgh, Pennsylvania 15213
[10]Creighton University, Omaha, Nebraska 68178
[11]Nuclear Physics Institute AS CR, 250 68 Řež/Prague, Czech Republic
[12]Laboratory for High Energy (JINR), Dubna, Russia
[13]Particle Physics Laboratory (JINR), Dubna, Russia
[14]University of Frankfurt, Frankfurt, Germany
[15]Institute of Physics, Bhubaneswar 751005, India
[16]Indian Institute of Technology, Mumbai, India
[17]Indiana University, Bloomington, Indiana 47408
[18]Institut de Recherches Subatomiques, Strasbourg, France
[19]University of Jammu, Jammu 180001, India
[20]Kent State University, Kent, Ohio 44242
[21]Lawrence Berkeley National Laboratory, Berkeley, California 94720
[22]Massachusetts Institute of Technology, Cambridge, MA 02139-4307
[23]Max-Planck-Institut fuer Physik, Munich, Germany
[24]Michigan State University, East Lansing, Michigan 48825
[25]Moscow Engineering Physics Institute, Moscow Russia
[26]City College of New York, New York City, New York 10031
[27]NIKHEF, Amsterdam, The Netherlands
[28]Ohio State University, Columbus, Ohio 43210
[29]Panjab University, Chandigarh 160014, India
[30]Pennsylvania State University, University Park, Pennsylvania 16802
[31]Institute of High Energy Physics, Protvino, Russia
[32]Purdue University, West Lafayette, Indiana 47907
[33]University of Rajasthan, Jaipur 302004, India
[34]Rice University, Houston, Texas 77251
[35]Universidade de Sao Paulo, Sao Paulo, Brazil
[36]University of Science & Technology of China, Anhui 230027, China
[37]Shanghai Institute of Nuclear Research, Shanghai 201800, P.R. China
[38]SUBATECH, Nantes, France
[39]Texas A&M University, College Station, Texas 77843
[40]University of Texas, Austin, Texas 78712
[41]Tsinghua University, Beijing 100084, China
[42]Valparaiso University, Valparaiso, Indiana 46383
[43]Variable Energy Cyclotron Centre, Kolkata 700064, India
[44]Warsaw University of Technology, Warsaw, Poland

[45]University of Washington, Seattle, Washington 98195
[46]Wayne State University, Detroit, Michigan 48201
[47]Institute of Particle Physics, CCNU (HZNU), Wuhan, 430079 China
[48]Yale University, New Haven, Connecticut 06520
[49]University of Zagreb, Zagreb, HR-10002, Croatia

References

[Acc03] A. Accardi. *hep-ph/0212148*, 2003.

[Ack99] K.H. Ackermann et al. "The STAR Time Projection Chamber." *Nucl. Phys.*, **A661**:681c–685c, 1999.

[Ada03a] J. Adams et al. "Centrality Dependence of Charm Production from a Measuement of Single Electrons in Au+Au Collisions at $\sqrt{s_{NN}} = 200$ GeV." *Phys. Rev. Lett.*, **91**:072304, 2003.

[Ada03b] J. Adams et al. "Transverse momentum and collision energy dependence of high pT hadron suppression in Au+Au collisions at ultrarelativistic energies." *Phys. Rev. Lett.*, **91**:172302, 2003.

[Ada04] J. Adams et al. "Identified particle distributions in pp and Au+Au collisions at $\sqrt{S_{NN}} = 200$ GeV." *Phys. Rev. Lett.*, **92**:112301, 2004.

[Ada05a] J. Adams et al. *Nuclear Physics A*, **757**:102–183, 2005.

[Ada05b] J. Adams et al. "Pion, kaon, proton and anti-proton transverse momentum distributions from p+p and d+Au collisions at $\sqrt{S_{NN}} = 200$ GeV." *Phys. Lett. B*, **616**:8, 2005.

[Adc02] K. Adcox et al. *PHENIX Collaboration, Phys. Rev. Lett.*, **88**:242301, 2002.

[Adc05] K. Adcox et al. *Nuclear Physics A*, **757**:184–283, 2005.

[Adl04] S. S. Adler et al. "Identified charged particle spectra and yields in Au + Au collisions at $\sqrt{s_{NN}} = 200$ GeV." *Phys. Rev. C*, **69**:034909, 2004.

[Ale73] T. Alexopoulos et al. *Phys. Rev. D*, **48**:984, 1973.

[And99] E. Andersen et al. *Phys. Lett. B*, **449**:401, 1999.

[AT01] A. Accardi and D. Treleani. "Minijet transverse spectrum in high-energy hadron-nucleus collisions." *Phys. Rev. D*, **64**:11604, 2001.

[BGS98] S.A. Bass, M. Gyulassy, H. Stöcker, and W. Greiner. "Signatures of Quark-Gluon-Plasma formation in high energy heavy-ion collisions: A critical review." *nucl-ph/9810281*, 1998.

[Bjo83] J.D. Bjorken. *Phys. Rev.*, **D27**:140, 1983.

[Ble00a] M. Bleicher et al. *Phys. Lett. B*, **485**:133, 2000.

[Ble00b] M. Bleicher et al. "Strangeness enhancement from strong color fields at relativistic heavy ion energies." *Phys. Rev. C*, **62**:061901, 2000.

[Cai04] X.Z Cai. *Proceedings of SQM2004*, 2004. for the STAR Collaboration.

[Cas04] W. Cassing et al. *Nucl. Phys. A*, **735**:277, 2004.

[CJJ74] A. Chodos, R. L. Jaffem, K. Johnson, C.B. Thorn, and V. F. Weisskopf. *Phys. Rev.*, **D9**:3471, 1974.

[Col92] The STAR Collaboration. "Conceptual Design Report for the Solonnoid Tracker at RHIC." Technical report, STAR Collaboration, 1992.

[CP75] J. C. Collins and M. J. Perry. "Superdense Matter: Neutrons or Asympotically Free Quarks?" *Phys. Rev. Lett.*, **34**:1353, 1975.

[Cro75] J. W. Cronin et al. *Phys. Rev. D*, **11**:3105, 1975.

[DD83] C. D. Detar and J. F. Donoghue. *Ann. Rev. Nucl. Part. Sci.*, **33**:235, 1983.

[DE03] D. D'Enterria. "High p_T Identified Particles in PHENIX: Data vs Theory." 2003.

[Dre99] H. J. Drescher et al. "A unified treatment of high energy interactions." *J. Phys. G*, **25**, 1999.

[Eid04] S. Eidelman et al. *Phys. Lett. B*, **592**:1, 2004.

[Fri03] R. J. Fries et al. "Hadron production in heavy ion collisions: Fragmentation and recombination from a dense parton phase." *Phys. Rev. C*, **68**:044902, 2003.

[GG00] (Particle Data Group), D.E. Groom, et al. *Eur. Phys. Journal.*, **C15**:1, 2000.

[Got87] G. Gottieb. *Phys. Rev.*, **D35**:2531, 1987.

[GP90] M. Gyulassy and M. Plummer. "Jet Quenching in Dense Matter." *Phys. Lett. B*, **243**:432–438, 1990.

[Gre03] V. Greco et al. "Partonic coalescence in relativistic heavy ion collisions." *Phys. Rev. C*, **68**:034904, 2003.

[GW73] D. J. Gross and F. Wilczek. "Ultraviolet Behavior of Non-Abelian Gauge Theories." *Phys. Rev. Lett.*, **30**:1343, 1973.

[Hag02] K. Hagiwara et al. *Phys. Rev. D*, **66**:010001, 2002.

[Hec98] H. van Hecke et al. *Phys. Rev. Lett.*, **81**:5764, 1998.

[HY03] R. C. Hwa and C. B. Yang. *hep-ph/0312271*, 2003.

[HY04a] R. C. Hwa and C. B. Yang. *hep-ph/0403001*, 2004.

[HY04b] R. C. Hwa and C. B. Yang. *hep-ph/0401001*, 2004.

[HY04c] R. C. Hwa and C. B. Yang. *hep-ph/0404066*, 2004.

[Kar02] F. Karsch. "Lattice Results on QCD Thermodynamics." *Nucl. Phys.*, **A98**:199 – 208, 2002.

[Kha96] D. Kharzeev. *Phys. Lett. B*, **378**:238, 1996.

[Kha02] D. Kharzeev et al. "Parton Saturation and Npart Scaling of Semi-hard processes in QCD." *hep-ph/0210332*, 2002.

[Kha03] D. Kharzeev et al. *Phys. Lett. B*, **561**:93, 2003.

[Kop74] G.I. Kopylov. *Phys. Lett.*, **B50**:472, 1974.

[Kuh76] J. Kuhn. "Nucleon-number dependence of large-transverse-momentum reactions and multiple scattering." *Phys. Rev. D*, **13**:2948, 1976.

[LK03] Z. W. Lin and C. M. Ko. "Deuteron-nucleus collisions in a multi-phase transport model." *Phys. Rev. C*, **68**:054904, 2003.

[Lon02] H. Long. "Mid-rapidity Λ and $\bar{\Lambda}$ Production in $Au + Au$ Collisions at the relativistic Heavy Ion Collider." Ph.D. Thesis, University of California at Los Angeles, 2002.

[Lon05a] H. Long. *Private Communication*, 2005.

[Lon05b] H. Long et al. "Scaling Properties of Hyperon Production from Au+Au Collisions at RHIC." to be publised, 2005.

[LP83] M. Lev and B. Petersson. *Z. Phys. C*, **21**:155, 1983.

[MV03] D. Molnar and S. A. Voloshin. "Elliptic Flow at Large Transverse Momenta from Quark Coalescence." 2003.

[Pol73] H. David Politzer. “Reliable Perturbative Results for Strong Interactions?” *Phys. Rev. Lett.*, **30**:1346, 1973.

[Qua04] Proceedings of Quark Matter. *Journal of Physics G: Nuclear and particle Physics*, 2004.

[Raf82] J. Rafelski. *Phys. Rep.*, **88**:331, 1982.

[RD80] J. Rafelski and M. Danos. *Phys. Lett. B*, **97**:279, 1980.

[Red01] K. Redlich et al. “Satistical hadronization and strangeness enhancement from p-A to Pb-Pb collisions.” *J. Phys. G: Nucl. Part. Phys.*, **27**:413–420, 2001.

[RH81] J. Rafelski and R. Hagedorn. *Statistical Mechanics of Quarks and Hadrons.* North Holland, Amsterdam, 1981.

[RM86] J. Rafelski and B. Muller. *Phys. Rev. Lett.*, **56**:2334(E), 1986.

[RT02] K. Redlich and A. Tounsi. “Strangeness enhancement and energy dependence in heavy ion collisions.” *Eur. Phys. J. C*, **24**:589–594, 2002.

[Sch93] E. Schnedermann et al. “Thermal phenomenology of hadrons from 200A GeV S+S collisions.” *Phys. Rev. C*, **48**:2462, 1993.

[Sim05] Frank Simon. “Production of Λ Hyperons at Forward Rapidity in d+Au Collisions at $\sqrt{s_{NN}} = 200$ GeV.” Ph.D. Thesis, Max-Plank-Institut für Physik, Munich, Germany, 2005.

[Sjo94] T. Sjostrand. *Comp. Phys. Comm.*, **82**:74, 1994.

[Sof99] S. Soff et al. “Strangeness Enhancement in Heavy Ion Collisions-Evidence for Quark-Gluon-Matter?” *Phys. Lett. B*, **471**:89, 1999.

[Sol93] J. Sollfrank et al. *Phys. Rev. C*, **48**:2462, 1993.

[Sor95] Sorge. “Flavor production in Pb(160 A GeV) on Pb collisions: Effect of color ropes and hadronic rescatterings.” *Phys. Rev. C*, **52**:3291, 1995.

[Sor03] P. R. Sorensen. “Kaon and Lambda Production at Intermediate p_T: Insights into the Hadronization of the Bulk Partonic Matter Created in Au+Au Collisions at RHIC.” Ph.D. Thesis, University of California at Los Angeles, 2003.

[STA05] Strangeness Physics Working Group at STAT. *Private Communication*, 2005.

[Str92] P. B. Straub et al. *Phys. Rev. Lett.*, **68**:452, 1992.

[VG99] S.E. Vance and M. Gyulassy. "Anti-hyperon enhancement through baryon junction loops." *Phys. Rev. Lett.*, **83**:1735, 1999.

[VG02a] I. Vitev and M. Gyulassy. *Phys. Rev. C*, **65**:041902, 2002.

[VG02b] I. Vitev and M. Gyulassy. "High-pT Tomography of d + Au and Au + Au at SPS, RHIC, and LHC." *Phys. Rev. Lett.*, **89**:252301, 2002.

[Vit01] I. Vitev et al. *hep-ph/0109198*, 2001.

[Wan00] X.N. Wang. "Systematic study of high p_T hadron spectra in pp, pA and AA collisions at ultrarelativistic energies." *Phys. Rev. C*, **61**:064910, 2000.

[Wan04a] X. N. Wang. *Phys. Lett. B*, **595**:165, 2004.

[Wan04b] X.N. Wang. "High-p_T Hadron Spectra, Azimuthal Anisotropy and Back-to-Back Correlations in High-energy Heavy-ion Collisions." *nucl-th/0305010*, 2004.

[Wer04] K. Werner et al. "Proton proton and deuteron gold collisions at RHIC." *hep-ph/0405274*, 2004.

[Wer05] K. Werner et al. "Parton Ladder splitting and the Rapidity Dependence of Transverse Momentum Spectra in Deuteron-Gold collisions at RHIC." *hep-ph/0506232*, 2005.

[WG91] X.N. Wang and M. Gyulassy. "HIJING: A Monte Carlo model for multiple jet production in p+p, p+A and A+A collisions." *Phys. Rev. D*, **44**:3501, 1991.

[WG92] X.N. Wang and M. Gyulassy. *Phys. Rev. Lett.*, **68**:1480, 1992.

[Won94] C. Wong. *Introduction to High-Energy Heavy-Ion Collisions*. World Scientific, Singapore, first edition, 1994.

[Yam01] E. T. Yamamoto. "Φ Meson Production in $Au + Au$ Collisions at the relativistic Heavy Ion Collider." Ph.D. Thesis, University of California at Los Angele, 2001.

[Zaj02] W.A. Zajc et al. “Overview of PHENIX Results from the First RHIC Run.” *Nucl. Phys.*, **A698**:39–53, 2002.

[Zha98] B. Zhang. *Comp. Phys. Comm.*, **109**:193, 1998.

[Zha00] B. Zhang et al. “A multi-phase transport model for nuclear collisions at RHIC.” *Phys. Rev. C*, **61**:067901, 2000.

[Zha02] Y. Zhang et al. “High-pT pion and kaon production in relativistic nuclear collisions.” *Phys. Rev. C*, **65**:034903, 2002.